Cell Patterning Technology for Controlling the Stem Cell Microenvironment

by

Adam Rosenthal

B.S. Massachusetts Institute of Technology, 2001
M.Eng. Massachusetts Institute of Technology, 2002

Submitted to the Harvard-MIT Division of Health Sciences and Technology
in partial fulfillment of the requirements for the degree of

Doctor of Philosophy
at the
Massachusetts Institute of Technology

June 2007

Signature of Author..
Division of Health Sciences and Technology
January 26th, 2007

Certified by..
Joel Voldman
Associate Professor of Electrical Engineering and Computer Science
Thesis Supervisor

Certified by..
Sangeeta Bhatia
Associate Professor of Health Sciences and Technology and
Electrical Engineering and Computer Science
Thesis Chair

Certified by..
George Daley
Associate Professor of Biological Chemistry and Molecular Pharmacology
Harvard Medical School and Pediatrics Children's Hospital Boston
Thesis Committee Member

Accepted by..
Martha L. Gray
Edward Hood Taplin Professor of Medical and Electrical Engineering
Director, Harvard-MIT Division of Health Sciences and Technology

Cell Patterning Technology for Controlling the Stem Cell Microenvironment

by

Adam Rosenthal

Submitted to the Harvard-MIT Division of Health Sciences and Technology
on January 26th, 2007
in partial fulfillment of the requirements for the degree of Doctor of Philosophy in
Electrical and Biomedical Engineering

Abstract

Embryonic stem cells serve as powerful models for the study of development and disease and hold enormous potential for future therapeutics. Yet, over two decades after mouse embryonic stem cells (mESCs) were first isolated, there is still little known about the role of cell-cell signaling in self-renewal. Since traditional cell-culture techniques do not provide significant control of the stem cell microenvironment, the goal of this thesis was to develop a cell patterning technology that allows us to precisely control stem cell signaling and monitor cell proliferation over time.

In the first aim of this thesis, we describe the development of our first cell patterning technology using dielectrophoresis (DEP). DEP uses nonuniform electric fields to trap cells on or between electrodes. We first used beads as model particles to validate the strength of our DEP square trap, and then demonstrated efficient cell patterning with multiple cell types.

In the second aim of this thesis, we describe the development of a novel cell patterning technology that we created, called the Bio Flip Chip (BFC). The BFC is a microfabricated polymer chip, containing thousands of microwells, that enables cell patterning with single-cell resolution anywhere on a substrate and onto any substrate.

In the last aim of this thesis, we used our BFC technology to control the stem cell microenvironment, allowing us to incrementally and independently modulate cell-cell contact. We present the first quantitative evidence that cell-cell contact depresses mESC colony formation and show that E-cadherin signaling is responsible for this negative regulatory pathway.

Thesis Supervisor: Joel Voldman
Title: Associate Professor of Electrical Engineering and Computer Science

Thesis Chair: Sangeeta Bhatia
Title: Associate Professor of Health Sciences and Technology and
Electrical Engineering and Computer Science

Thesis Committee Member: George Daley
Title: Associate Professor of Biological Chemistry and Molecular Pharmacology at
Harvard Medical School and Pediatrics Children's Hospital Boston

Acknowledgments

I would first like to thank Joel for being an incredible mentor throughout my PhD. While it was painful at times, Joel you always pushed me to perform at my highest potential. Through your example, you taught me how to communicate effectively and think critically, along with the true meaning of the words efficiency and multitasking. Thank you for accepting me as your first student and allowing me to participate in the lab-building process.

I would also like to thank all the Voldman babies. Thanks to Brian for being a great officemate. I will miss your eclectic choice in music, your adventures in dating, the Pika stories, the leg lamp, and your dirty sense of humor. Thanks to Lily for sharing the HST experience with me, for always being willing to chat about politics or career stuff, and for understanding my pain when we had to come in during the weekend to feed our hungry stem cells. Thanks to Mike for being so generous, with everyone in the lab, and for being a supermodel-er. Thanks to Salil for being the master of microscopy, for constantly feeding me new music, and for being a worthy movie critic. Thanks to Joseph for challenging my political viewpoints, sharing the Baker House experience with me, and for being a good cowboy. Thanks to Pat for his enthusiasm about stem cells and sharing his love of Thailand. Thanks to Nick for his hard work on the DEP Microwells, not DEPelles ☺, and for bringing his physics perspective to the lab.

And thanks to the rest of the Voldman lab graduate alums: Nitzan, Katya, Nina, and Rikki, who have made the lab such a nice environment to work. I would also like to specially thank my UROPs, who have helped me enormously throughout the years: Maia for your help on the DEP trapping, Alice for being vital to the development of the BFC and for teaching me how to play Sudoku, and Steph for helping to carry the torch into the future of the BFC technology. And to the people in the MTL, thank you for transforming me from a young kid who knew nothing about fab into an old man who knows a little more about fab. Special thanks to Kurt for sharing all your knowledge and for making my long hours in the fab entertaining.

And lastly, and most importantly, I'd like to thank my family. My Mom for her spirituality, my Dad for his infectious curiosity, Paulette for her caring and generosity, Renuka for her for wisdom, and Brinda for her love.

Table of Contents

Table of Figures

Chapter 1: Introduction

In this thesis, we describe the development of two cell patterning technologies. The first uses dielectrophoresis (DEP) to trap and position cells. The second is a cell patterning technology that we created, called the Bio Flip Chip (BFC). Using the BFC, we then answer an important biological question – how do the seeding conditions of mouse embryonic stem cells (mESCs) affect their proliferation? More specifically, why do mESCs need to be seeded as single cells?

In this chapter, we will first describe the factors affecting mESC self-renewal and further discuss the role of cell-cell signaling in this process. Then, in order to answer the above biological questions, we describe the types of experiments that are required, thus motivating the need for new types of cell patterning tools. We will then discuss our two cell patterning technologies and conclude with an outline of the rest of the thesis.

1.1 Mouse Embryonic Stem Cell Self-Renewal

Embryonic stem cells (ESCs) serve as powerful models for the study of development and disease and hold enormous potential for future therapeutics. Stem cells can generally be manipulated in culture in two ways. The first is to drive them to differentiate to a specific phenotype – such as cardiomyocytes[1], hematopoietic cells[2], hepatocytes[3], pancreatic islets[4], neurons[5,6], etc. The second is expand ESCs thru self-renewal, allowing proliferation and maintaining pluripotency so that they can form derivatives of all three embryonic germ layers[7].

While ESCs have been isolated from a number of organisms, the most useful applications have come from studying mouse and human ESCs. However, mouse embryonic stem cell (mESC) biology is more mature, primarily because mESCs were isolated almost two decades before human embryonic stem cells (hESCs) were first derived in 1998[7]. mESC self-renewal is thought to involve both intracellular and extracellular factors (Figure 1-1). Intracellularly, Oct4 and Nanog are thought to be the two most important transcription factors. Both factors are required in order to maintain self-renewal, although the level of Oct4 expression must be tightly controlled[8,9,10].

Extracellularly, there have been a number of signals that are necessary for self-renewal. It was discovered that mESCs remain undifferentiated when grown in the presence of Leukemia Inhibitory Factor (LIF) and serum[11]. LIF binds to its receptor (LIFR), complexes with gp130[12], and activates the STAT3 pathway. While there is evidence to suggest STAT3 activation alone is sufficient for self-renewal[13-15], these analyses where done in serum or at relatively high cell densities, and thus serum or autocrine diffusible signaling could have been involved in affecting self-renewal[10]. Recently, other important extracellular mediators of self-renewal have been identified. Researchers have shown that culturing with LIF and Bone Morphogenetic Protein (BMP) can cause mESCs to self-renew in the absence of serum, by inducing the Id family of genes via the Smad pathway[16]. The Id proteins block lineage-specific transcription factors, enabling the self-renewal response to LIF/STAT3. The Wnt family of proteins also seems to be important in self-renewal, as researchers have been able to cause mESCs to self-renew by using a small-molecule inhibitor of glycogen synthase kinase-3 (GSK-3), facilitating efficient Wnt pathway activation[17].

Extracellularly, there is another important component of mESC self-renewal, cell-cell signaling – consisting of diffusible signaling and cell-cell contact (e.g., juxtacrine signaling). The contribution of cell-cell signaling in mESC self-renewal is described in detail in the next section.

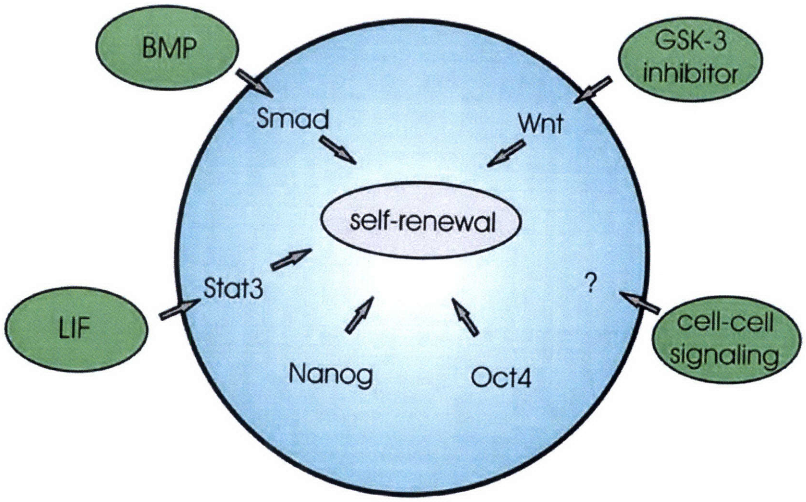

Figure 1-1: Intracellular and extracellular factors involved in mESC self-renewal. Extracellularly, the effects of cell-cell signaling – including diffusible signaling and cell-cell contact – also contribute to self-renewal.

1.2 Cell-Cell Signaling in mESC Self-Renewal

Cell-cell signaling can be modulated *in vitro* in several ways, using molecular inhibitors[17-19] or genetic approaches[8,9,14], but both are limited to manipulating single or known molecules. Alternatively, one can manipulate the general class of cell-cell interactions by modulating the cells' relative positions, which has generally been accomplished by modulating the cell seeding density.

Several examples have demonstrated that cell seeding density affects stem cell behavior. Central nervous system stem cells differentiate into neurons, astrocytes, and oligodendrocytes when plated at high density, but generate smooth muscle at low density[20]. Rat mesenchymal stem cells have been shown to expand more rapidly and formed more single-cell-derived colonies as the cell seeding density was decreased[21], while rat osteogenic cells expanded more rapidly as the cell seeding density was increased[22]. In serum without LIF, ESCs differentiate less as the cell seeding density is increased[19], supporting the belief that ESCs secrete autocrine diffusible factors that maintain self-renewal[10]. However, these cells were seeded at densities up to 25,000 cells/cm^2, allowing cells to combine, confounding their results with effects from cell-cell contact.

There are several possible candidates for the diffusible factors involved in self-renewal. Even without LIF supplementation of the medium, some cells stay undifferentiated, consistent with the fact that ESCs are known to secrete LIF[19,23], which has shown to be activated upon early differentiation[24]. The evidence for autocrine LIF secretion is further supported by the fact that the addition of anti-LIF antibody to media without LIF increases differentiation[19] and LIF-deficient clones exhibited more differentiation than normal ESCs[23]. However, the fact that ESC self-renewal is not completely abolished in these two cases suggests that soluble factors other than LIF might prevent ESC differentiation and that they are synthesized by both wild type and LIF-deficient cells. This factor has been given the name ES cell renewal factor (ESRF)[23]. Although ESRF is present in conditioned medium, it has not been identified using standard protein purification and COS cell expression cloning strategies[10]. Another candidate for autocrine factors involved in self-renewal is BMP. ESCs have the receptors for BMP and may have the potential for autocrine stimulation via BMP production[16]. Furthermore, some suggest there may also be ESC secretion of a differentiation-inducing agent[19].

Unfortunately, even less is known about the effects of cell-cell contact on mESC self-renewal. Convention has dictated that mESCs should be seeded as single cells[8,9,13,16,25,26] – anyone propagating mESCs follows these protocols and is certain to triturate down to single cells during cell seeding. However, these strict recommendations are based on qualitative observations that seeding mESCs as clusters decreases self-renewal. Of the studies that have quantitatively investigated this phenomena, they showed that seeding mESCs as clusters of thousands of cells can cause differentiation[27]. Therefore, most of the research exploring the importance of the cell seeding conditions on self-renewal (e.g., whether or not cell-cell contact has an effect) only investigated mESC behavior at both extremes of cell seeding conditions, as single cells or clusters of thousands of cells. However, there have been no reports quantitatively studying the effects of seeding smaller cell clusters, such as a few cells, allowing incremental changes in cell-cell contact. Traditional cell-culture techniques cannot reliably seed small groups of cells in a scalable fashion, with or without cell contact. To do this, we require cell patterning.

1.3 Cell Patterning

Cell patterning – the ability to place cells in a desired location – has become an increasingly important tool for control of the cellular microenvironment. Cell patterning can be used to manipulate cell-cell interactions, varying the contact area between two cell types in co-culture[28]. Cell patterning can also be used to direct cell-matrix interactions, controlling the amount of contact area with the extracellular matrix (ECM)[29] or the type of ECM that the cell sits on[30]. Techniques have even been developed to extend these planar interactions into a three-dimensional cellular matrix[31]. Cell patterning also has the potential to improve devices like cell-based biosensors – using living cells as sensing elements for applications like toxin detection[32] and defense monitoring[33]. Cells have successfully been interfaced to sensing elements to form cell-based biosensors and recent advances in cell patterning may enable reproducible and manufacturable biosensor devices[34].

Several techniques exist for patterning cells. Some techniques use physical barriers to place cells, such as elastomeric stencils[35,36] or microwells[37,38]. The substrate that the cells sit on can also be modified to selectively pattern cells. Microcontact printing uses a PDMS stamp to pattern matrix proteins onto a substrate[29,39] while electroactive substrates use an applied voltage to switch the surface properties of a substrate, both allowing cells to selectively attach in specific areas[40,41]. Electromagnetic forces can also be used to pattern cells. Electrophoresis utilizes the negative charges of cell-membrane proteins to exert forces on cells in a constant (DC) electric field, creating patterned cellular arrays[42]. Optical tweezers use optical frequency non-uniform electromagnetic fields to manipulate cells[43,44], while dielectrophoresis (DEP) uses non-uniform AC electric fields in the range of 10 kHz-100 MHz to position cells on or between electrodes[45,46].

When choosing a cell patterning technology, there are several capabilities to consider: patterning cells with single-cell resolution, patterning large numbers of cells, allowing the patterned cells room to grow and move, being gentle on the cells, and being easy to use. To answer our questions about the seeding conditions of mESCs, we need to be able to create patterns of single (or small numbers of) cells onto a variety of substrates and monitor their proliferation over time. Therefore, first we need a technique that can pattern with single-cell resolution. Second, since mESCs divide rapidly (with a doubling time of ~14 hours[19]), we also need to be able to pattern cells onto an unconfined area, allowing the patterned cells room to proliferate. μCP, for instance, restricts motility and proliferation by chemically patterning the substrate, leading researchers to develop switchable substrates that in turn require chemical synthesis[41] or uncommon materials[40] (e.g., ultrapure gold). Third, to ensure meaningful results, we need to perform our experiments with significant numbers of cells, so we require a cell patterning technique that is scalable. Lastly, since mESCs are so sensitive to their microenvironment, we need a technology that is gentle on the cells. Both of our chosen cell patterning technologies, DEP and the Bio Flip Chip, can be operated to meet these requirements.

1.4 Dielectrophoresis

Dielectrophoretic (DEP) traps use the interaction of an induced multipole with a nonuniform electric field to create forces that will stably position particles[47]. DEP traps can use either positive dielectrophoresis (pDEP) – pulling cells toward the electrodes (Figure 1-2A) – or negative dielectrophoresis (nDEP) – pushing cells away from the electrodes (Figure 1-2B). DEP forces can be used to trap a variety of particles - including micron and submicron polymer beads[48,49], cells[50-52], viruses[53,54], and bacteria[55,56].

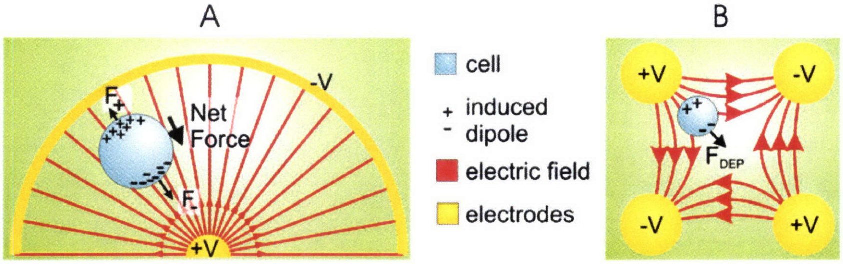

Figure 1-2: The two kinds of DEP traps: (A) pDEP trapping, where the cells are pulled towards the electrodes and (B) nDEP trapping, where the cells are pushed away from the electrodes.

DEP fulfills many of our requirements in a cell patterning technique. Since DEP traps consist of scalable electrode arrays, they can be designed to pattern thousands of cells on a single glass slide and be made small enough to ensure single-cell resolution[57]. In addition, DEP can be used to place cells without the need for patterning the substrate[58], thus giving the cells room to proliferate[52,58]. This ability to simultaneously pattern single cells and allow them room to proliferate is not possible using many other scalable, cell patterning techniques (Figure 1-3). Lastly, the effects of DEP on cell health can be quantitatively modeled, allowing DEP trap operation that minimizes damage to the cells while still maximizing trap performance.

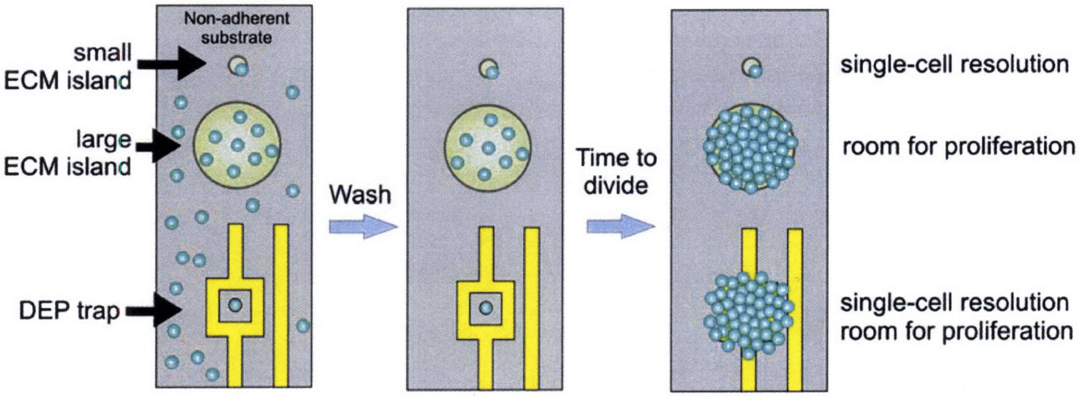

Figure 1-3: Comparison of substrate modification techniques and DEP. DEP can pattern with single-cell resolution *and* allow room for cells to proliferate, while substrate modification techniques cannot simultaneously enable both of these capabilities.

1.4.1 DEP Trap Requirements

Prior single-cell DEP traps include nDEP octopole [59], nDEP cages[60], nDEP posts[61], pDEP circles[58], and a pDEP points-and-lid geometry[52,57]. Previous single-cell DEP traps designed for cell patterning all use pDEP, which require the cells to be immersed in an artificial low-conductivity media[52,57,58]. Although these pDEP traps only need to use this low-conductivity media while trapping, which can be accomplished within minutes, overnight exposure to this media caused cells to detach more frequently and proliferate more slowly than controls[57]. mESCs were even more sensitive and showed decreased proliferation after only thirty minutes of exposure to this low-conductivity media (Figure 1-4). nDEP traps, however, allow the use of normal cell-culture media. Therefore, in order to avoid any negative interactions with the pDEP media, we chose to restrict ourselves to the use of nDEP to pattern mESCs.

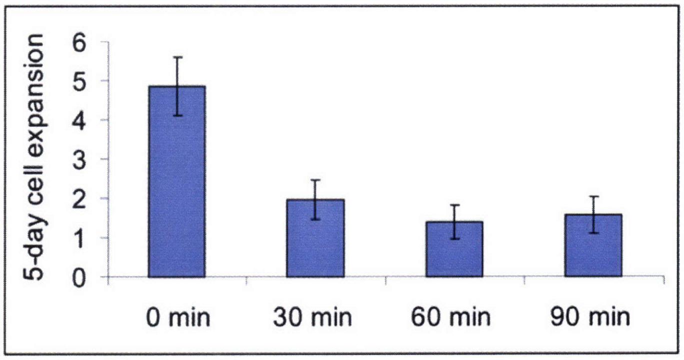

Figure 1-4: Effects of low-conductivity media exposure on proliferation. mESCs were exposed to low-conductivity media (21% of 50% w/v sucrose solution in 18.2-MΩ-cm deionized water, 1% ES-qualified fetal bovine serum (Invitrogen, 16141-079), 78% 18.2-MΩ-cm deionized water) for 30-90 min and then transferred to normal mESC media and grown for five days. At day 5, cell numbers were counted using a Coulter counter (Beckman Coulter, Z2), measured three times for each of three separate wells. The 5-day cell expansion was calculated by dividing the number of cells on day 5 by the starting cell number, showing that the pDEP media significantly affects mESC proliferation even for exposures as short as 30 min. Bars on experimental data indicate 1 standard deviation from the mean.

In addition to using nDEP, we require a trap that has multidirectional stability (in x, y, and z), allowing the particle to remain stably held in the trap. And while some DEP traps can operate without using flow[52,58,62-65], most scalable, single-cell DEP traps require this wash step to remove untrapped cells. Therefore, the DEP traps need to be strong enough to hold particles against this fluid flow. Stability in the plane of the electrodes (x and y) had been achieved with previous single-cell nDEP traps by surrounding the trapped particles with electrodes, usually in a quadrupole geometry[59,61,66,67]. This creates a stabilizing force that pushes the particle back into the center of the trap, away from the electrodes (Figure 1-5A). However, these planar quadrupole geometries[66,67] have an upward DEP force everywhere in the trap (Figure 1-5B) and are not stable in the z-direction. Once a certain voltage is reached, the upward DEP force exceeds the gravitational force, causing the particles to be levitated into higher velocity flows and washed away. This causes the maximum flow rate, the highest flow rate where a particle is stably held in the trap, to decrease with increasing voltage[67].

One can add trap stability in the z-direction by building the trap in three dimensions, either by using electrodes on a top and bottom substrate, forming an octopole[59,68] (Figure 1-5C), or by extruding the actual electrodes into posts[61] (Figure 1-5D). However, the octopole trap positions cells in the center of the chamber, away from the bottom substrate, making it less appropriate for cell patterning. In addition, if the top and bottom quadrupoles are not precisely aligned, trap performance is compromised, making packaging difficult. The DEP posts, on the other hand, are difficult to fabricate and would not allow *unobstructed* cell proliferation. Overall, we need a strong, planar, single-cell nDEP trap. These requirements necessitate a quantitative modeling tool capable of designing a trap to meet these increased demands.

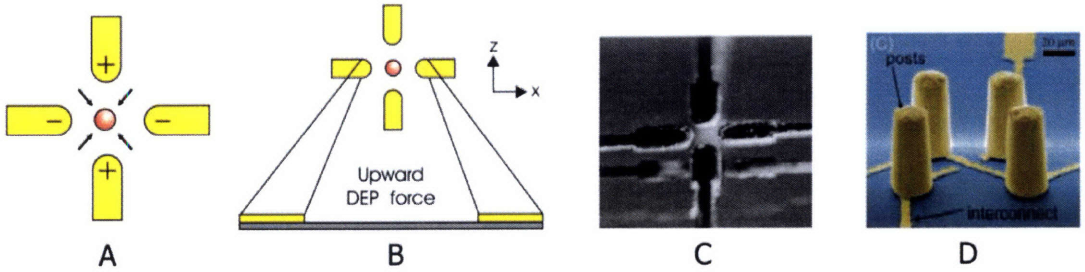

Figure 1-5: DEP trap requirements. (A) The planar quadrupole has stability in the *x* and *y* direction, but (B) does not have stability in the *z*-direction, since the DEP force is upward everywhere in the trap. To provide the planar quadrupole with stability in the z-direction, the trap can be made 3-D, into either (C) an octopole trap[68] or (D) extruded quadrupole posts[61].

1.4.2 Modeling DEP Trap Behavior

For a variety of reasons, much of the DEP-based trap design to date has been qualitative in nature. Most current microscale DEP traps are meant to capture many particles at once. The electrostatic interactions between the many particles in such a trap make the trapping behavior very difficult to quantitatively analyze. Additionally, traps for large particles, such as cells, are relatively simple to design and fabricate – many electrode configurations and experimental conditions will generate some kind of trapping, and thus detailed analysis may not be necessary. However, the maturation of DEP-based microsystems necessitates a quantitative modeling tool that enables trap designs that can meet these increased demands.

Before the creation of our modeling software, several groups had performed quantitative analysis of DEP-based microsystems. Pioneering work in validating the shape of the force fields was first reported by the German group for quadrupole[66] and octopole DEP traps[59]. DEP forces have also been quantified using gravity as a counterforce, by measuring particle levitation over quadrupoles[66,69] or interdigitated electrodes[65,70]. Several other groups have analyzed the balance of DEP forces and hydrodynamic drag. Watarai *et al.* measured the migration velocity of a particle traveling through a quadrupole trap[71]. Similar experiments where later done by the German group measuring the particle displacement in an octopole trap against flow[72] and the critical flow velocity needed to break through paired electrodes on the top and bottom of the flow chamber[73] – both correlating modeling predictions to experiments. Hughes *et al.* quantified the DEP force by using quadrupole traps to confine motile bacteria[74]. From the DEP trapping force, they calculated the bacterial swimming velocity and found good agreement compared to published values. While all of these quantitative analyses have worked well for their specific applications, they investigate only limited aspects of DEP trapping behavior – such as particle levitation, velocity, or displacement within a DEP trap. Therefore, we created a novel modeling software, described below, that could perform comprehensive analysis of DEP trapping and allow us to create the types of highly-functional DEP traps that we require.

The software was originally created by Joel Voldman in his PhD thesis[75], which he validated with both beads[61,67] and cells[76], allowing him to create the extruded quadrupole electrodes, the strongest-known 3-D, nDEP trap[61]. Since then, we have made further improvements to the modeling software, increasing its performance and ease-of-use, described below in Section 1.4.3:Modeling Software Overview.

Furthermore, since the initial creation of our modeling software, other groups have started to comprehensively model DEP trapping for other applications. Li *et al.* used a 2-D model, very similar to ours, to create a microfluidic DEP filter for yeast, spores, and bacteria[48].

1.4.3 Modeling Software Overview

We wrote the software using Matlab (The Mathworks, R14) to take advantage of the diverse numerical and visualization algorithms available within. The modeling software, though general, was written expressly for analyzing the problem of DEP trapping of single particles against fluid flows. An overview of the software is given in Figure 1-6. The software takes electric-field data and other experimental parameters and computes each of the five forces on the particle – the multi-order DEP force (Eq. 1-3), the hydrodynamic drag force (Eq. 1-6 and 1-7), the gravitational force (Equation 1-8), the hydrodynamic lift force (Equation 1-9), and the normal force from the top and bottom substrates.

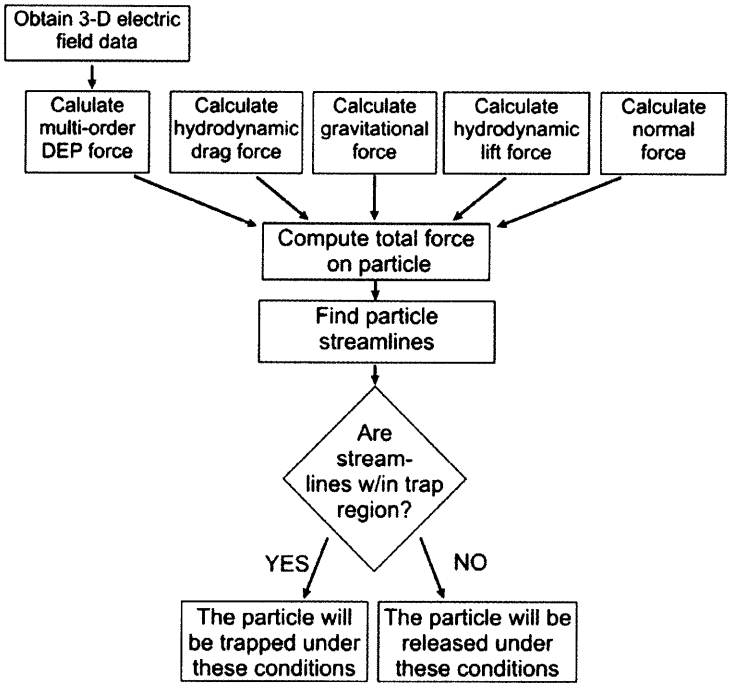

Figure 1-6: Overview of the modeling software, showing the major steps. From user-provided electric field data and other experimental parameters, the forces on the particle (DEP, HD drag, gravitational, HD lift, and normal) are computed everywhere in space. The total force on the particle is used to generate streamlines that determine if the particle is stably held in the trap.

The DEP force can be in the x, y, and z directions, depending on the trap geometry. The HD drag force is applied in the $+x$ direction in our microsystem. The gravitational force pushes down on the particle in the $-z$ direction, since the particles are more dense than the surrounding media. The HD lift force is caused by low-Reynolds-number viscous flow over an object near a solid plane, which tries to levitate the particle in the +*z* direction[77,78]. Our final force is the normal force in the -*z* and +*z* direction, respectively defined by the top and bottom of the flow chamber.

After each force is individually calculated, the total force in all directions (*x, y,* and *z*) is summed on a uniformly spaced grid. Streamlines are then generated from these total force calculations, mapping its trajectory from a specified starting position, allowing us to determine whether the particle is stably held in the trap. If the particle is held at that flow rate, the program continues to step up the flow rate to determine the maximum flow rate – the highest flow rate where the particle is still stably held in the trap. Any increase in flow above this rate will knock the particle out of the trap, producing streamlines highlighting this removal (Figure 1-7).

In calculating the maximum flow rate, we can easily vary certain parameters in the microsystem to determine their effects on the trapping behavior. Such parameters may include the applied voltage, the applied signal frequency, the particle diameter, the flow chamber geometries, and a number of other variables. In its current form, the program allows for the simultaneous variation of two parameters at once, so that for instance, sweeps in voltage and frequency can be performed, thus enabling the user to rapidly test a large range of experimental conditions simultaneously.

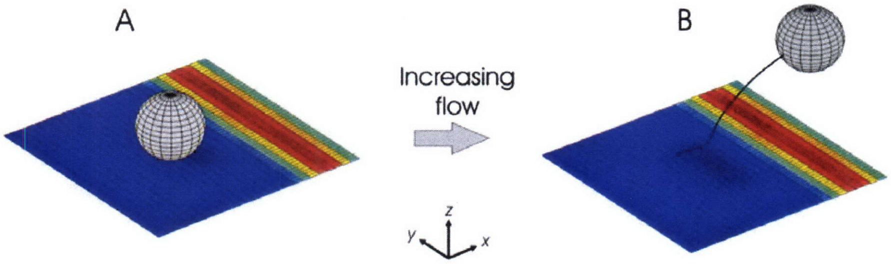

Figure 1-7: Particle streamlines. (A) The cell is stably held in the DEP trap. (B) The flow exceeds the maximum flow rate and the cell is pushed out of the trap. The color bar on the bottom substrate shows the electric field intensity in a given DEP trap.

Since its initial creation, we have improved the modeling software, using streamlines to make the program more efficient and visually-interactive. Originally, the software calculated the particle's stable points by using Matlab's *isosurface* function, finding the surface for each component of total force (F_x, F_y, F_z) where that force is zero[75]. Then, by determining if the three-way intersections of these points are stable, the software determined if the particle was held in the trap for a given set of experimental conditions. The use of streamlines obviates the need for these isosurfaces, since the streamlines generate the particle's trajectory directly from the total forces, automatically determining if a stable point exists. Brian Taff first explored using streamlines to investigate DEP trapping behavior. Then, to make the improved version of the software, we incorporated the *streamline* function into the automated software, replacing the *isosurface* subprogram to solve for the maximum flow rate. Currently, everyone in the Voldman Lab now uses this improved version to do their DEP modeling and trap design.

In addition, we used this improved version to create our nDEP square traps, the strongest-known planar, nDEP trap[50] (see Section 2.1.1: nDEP Square Trap Design) and demonstrated its functionality by comparing this trap to two other common traps in the literature[79] (see Appendix A). We have made this latest version of the software freely available to the scientific community at: www.rle.mit.edu/biomicro.

1.4.4 The DEP Force

The dielectrophoretic force in its simplest implementation is the interaction of a nonuniform electric field with the dipole moment it induces in an object. The typical case is the induced dipole in a lossy dielectric spherical particle. The force in this case, where the particle is much smaller than the electric field nonuniformities, is given by:

$$\mathbf{F} = 2\pi\varepsilon_m R^3 \operatorname{Re}\left[\underline{CM}(\omega)\cdot\nabla\underline{\mathbf{E}}^2(\mathbf{r},\omega)\right] \tag{1-1}$$

where **F** refers to the dipole approximation to the DEP force, ε_m is the permittivity of the medium surrounding the sphere, R is the radius of the particle, ω is the radian frequency of the applied field, **r** refers to the spatial coordinate, and $\underline{\mathbf{E}}$ is the complex applied electric field. $\underline{CM}$ is the Clausius-Mossotti (CM) factor, which, for a lossy dielectric uniform sphere, such as a bead, is given by:

$$\underline{CM} = \frac{\underline{\varepsilon}_2 - \underline{\varepsilon}_1}{\underline{\varepsilon}_2 + 2\underline{\varepsilon}_1} \tag{1-2}$$

where $\underline{\varepsilon}_1$ and $\underline{\varepsilon}_2$ are the complex permittivities of the medium and the particle, respectively, and are each given by $\underline{\varepsilon} = \varepsilon + \sigma/(j\omega)$, where ε is the permittivity of the medium or particle, σ is the conductivity of the medium or particle, and j is $\sqrt{-1}$. If the CM factor is positive, then the DEP force pulls particles toward the electric-field maxima (positive DEP, or pDEP). If the CM factor is negative, the DEP force pushes the particles towards the electric-field minima (negative DEP, or nDEP).

Most previous analyses incorporate only the dipole approximation to the DEP force[51,57] which does not account for higher-order components, where the field is sufficiently spatially nonuniform (in comparison to the size of the particle) to induce significant quadrupole and higher-order moments in the object. Analyses including higher-order multipoles have shown that these terms often make significant contributions to the total DEP force[48,79,80] (see Appendix A: Multipolar DEP Force Effects). In the mid-nineties, Washizu and Jones[81-83] developed a computationally accessible approach to calculating higher-order DEP forces. A compact tensor formulation of their result[81] is:

$$\mathbf{F}^{(n)} = \frac{\overset{\vdots}{p}^{(n)}[\cdot]^n(\nabla)^n\mathbf{E}}{n!} \tag{1-3}$$

where n refers to the force order (n=1 is the dipole, n=2 is the quadrupole, etc.), $\overset{\vdots}{p}^{(n)}$ is the multipolar induced-moment tensor, and $[\cdot]^n$ and $(\nabla)^n$ represent n dot products and gradient operations. Thus, we see that the n-th force order is given by the interaction of the n-th-order multipolar moment with the n-th gradient of the electric field. This expression can be rewritten more explicitly for the time-averaged force in the i-th direction as:

$$\begin{aligned} \left\langle F_i^{(1)} \right\rangle &= 2\pi\varepsilon_1 R^3 \,\mathrm{Re}\left[\underline{CM}^{(1)} \underline{E}_m \frac{\partial}{\partial x_m} \underline{E}_i^* \right] \\ \left\langle F_i^{(2)} \right\rangle &= \frac{2}{3}\pi\varepsilon_1 R^5 \,\mathrm{Re}\left[\underline{CM}^{(2)} \frac{\partial}{\partial x_m} \underline{E}_n \frac{\partial^2}{\partial x_n \partial x_m} \underline{E}_i^* \right] \\ &\vdots \end{aligned} \tag{1-4}$$

for the dipole (n=1) and quadropole (n=2) force orders[81]. The Einstein summation convention has been applied in Eq. 1-4. The multipolar CM factor for a uniform lossy dielectric sphere, such as a bead, is given by:

$$\underline{CM}^{(n)} = \frac{\underline{\varepsilon}_2 - \underline{\varepsilon}_1}{n\underline{\varepsilon}_2 + (n+1)\underline{\varepsilon}_1} \tag{1-5}$$

while the CM factor for cells, viruses, and bacteria is calculated using expressions from the literature[84].

1.4.5 The Other Forces

In our modeling software we include four other forces – the hydrodynamic (HD) drag force, the HD lift force, the gravitational force, and the normal force from the rigid substrate top and bottom boundaries.

The HD drag force imposed on a stationary particle by a moving fluid is governed by low-Reynolds-number flow because of the small dimensions and low flow rates involved in these microsystems. When the particle sits close to the substrate, we are justified in using a shear flow approximation. The HD drag force is then similar to Stokes' drag on a sphere, with a correction for the effects of the wall[85]:

$$F_{drag} = 6\pi\mu R\dot{\gamma} F^*_{drag} z = 6\pi\mu R \left(6Q/wh^2 \right) F^*_{drag} z \tag{1-6}$$

where μ is the viscosity of the liquid, F^*_{drag} is a nondimensional factor incorporating the wall effects, z is the distance from the particle center to the substrate, and $\dot{\gamma}$ is the shear rate at the wall in a parallel plate flow chamber, where Q is the flow rate, w is the chamber width, and h is the chamber height[86]. Li *et al.* showed that this shear flow approximation is valid even when the particle diameter occupies a significant fraction of the chamber height[48].

When the particle is not near the substrate, we use a parabolic Poiseuille flow profile. The HD drag force is then[87]:

$$F_{drag} = 6\pi\mu R V_c F(z) = 6\pi\mu R\left(1.5Q/wh\right)F(z) \tag{1-7}$$

where V_c is the centerline velocity in the flow chamber and $F(z)$ is a nondimensional factor incorporating the height of the particle in the chamber. Other analytical or non-analytical flow profiles can also be implemented.

The magnitude of the gravitational force is given by:

$$F_{grav} = -\frac{4}{3}\pi R^3(\rho_p - \rho_m)g \tag{1-8}$$

where ρ_m and ρ_p refer to the densities of the medium and the particle, respectively, and g is the gravitational acceleration constant.

The HD lift force is caused by low-Reynolds-number viscous flow over an object near a solid plane, which tries to levitate the particle. For a stationary sphere in contact with the plane, the lift force becomes[77,78]:

$$F_{lift} = 9.22\dot{\gamma}^2\rho_m R^4 = 9.22\left(36Q^2/w^2h^4\right)\rho_m R^4 \tag{1-9}$$

At lower flow rates, the lift force is negligible compared to the z-directed DEP force and gravity. However, since the lift is proportional to Q^2 and R^4, the lift force could become significant for higher flow rates and larger bead diameters.

Our final force is the implementation of a normal force produced by the top and bottom substrates. We implement this force using an algorithm that automatically adjusts the z-directed total force on the particle so that it is zero when the particle contacts the top or bottom surface. For example, when a particle contacts the bottom surface, the particle center will be located at $z = R$. Without this algorithm, if the total z-directed total is less than zero for $z < R$, then the particle would get pushed downward, which is physically impossible because the normal force of the bottom substrate would push back. Therefore, if the total z-directed force is less than 0 for $z < R$, this algorithm modifies the total z-directed force to equal zero, removing any downward force and keeping the particle sitting on the bottom substrate at $z = R$.

1.5 Microwells and the Bio Flip Chip

In addition to using DEP, we looked into other methods of cell patterning that could pattern large numbers of cells, with single-cell resolution, were easy to use, and gentle on the cells. Microwells have started becoming widely-used in the last few years as a cell patterning technique and offer all of these capabilities. The microwells can be made from a variety of materials – including polystyrene[88], polyethylene glycol (PEG)[37,89], and most commonly, polydimethylsiloxane (PDMS)[38,90,91] (Figure 1-8).

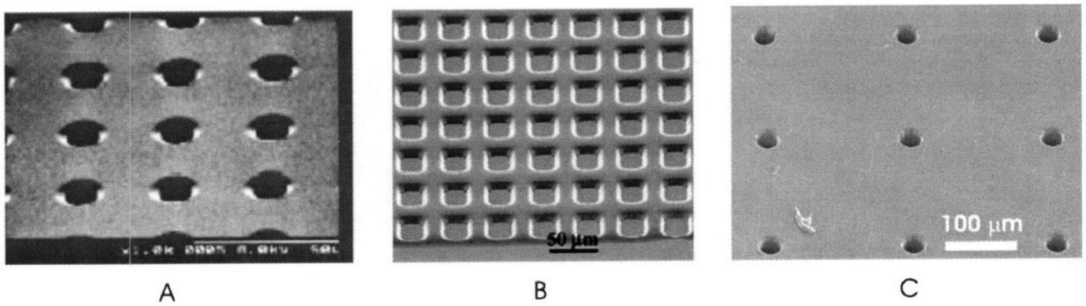

Figure 1-8: Microwells can be made from a variety of materials – including (A) polystyrene[88], (B) polyethylene glycol (PEG)[37], and (C) polydimethylsiloxane (PDMS).

Microwells are generally made using soft lithography, using a transparency mask to photopattern the microwell array, either directly into the desired material[37], or into a photoresist that will later be used as an inverse mold for the final microwell array. Using the latter process, molding requires only initial fabrication of the master wafer. Afterward, whenever a new chip needs to be made, the desired material is simply poured onto the master wafer, cured, and then peeled off (Figure 1-9A). The master wafer can be reused numerous times, making the overall chip creation fast and inexpensive (e.g., a microwell chip made from PDMS costs less than fifteen cents to make).

The operation of the microwells is also very easy. A single-cell solution is deposited onto the microwell array. The cells settle into the microwells, generally after a few minutes. Then, the remaining cells are washed away, while the cells in the microwells are protected from the high shear flows and remain trapped (Figure 1-9B). While microwells can be used for non-adherent cells[88], patterning adherent cells requires coating the bottom of the microwells with an adherent protein – such as collagen[37] or fibronectin[89,90].

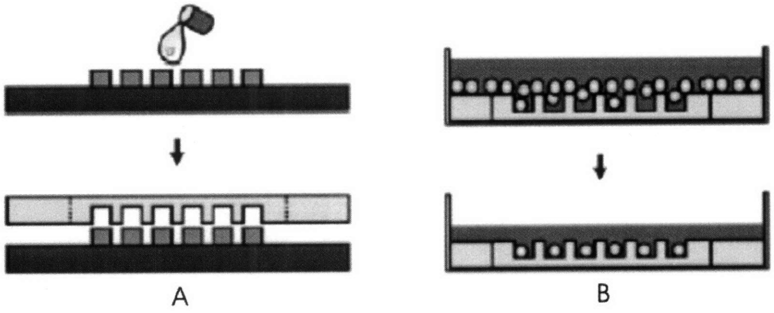

Figure 1-9: Fabrication and operation of microwells[38]. (A) Polymer is poured over the master wafer, molding the microwell array. (B) A single-cell solution is poured over the microwell, allowing the cells to settle in the wells, while the other cells are washed away.

To date, most microwell research has simply demonstrated patterning cells in microwells – with variations on the microwell material, the proteins inside and outside the microwell, or the microwell dimensions – although some groups are beginning to use them for enabling applications. Yamamura *et al.* patterned single B-cells in microwell arrays, monitoring which cells were activated after stimulation with antigen, then retrieved the activated cells using a micromanipulator[88] (Figure 1-10).

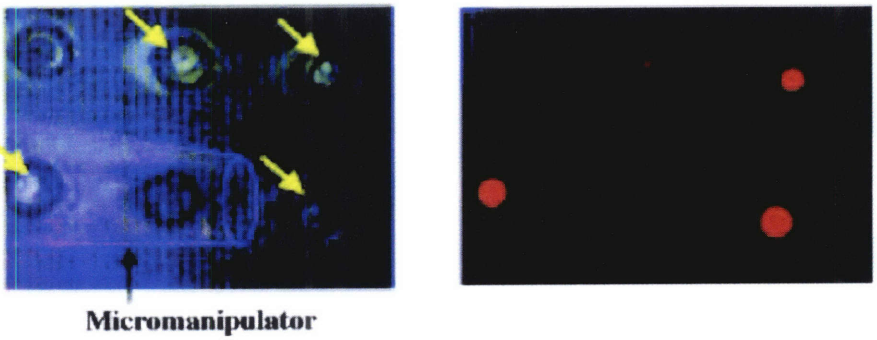

Figure 1-10: Using microwells for monitoring cell behavior, with subsequent retrieval of desired cells using a micromanipulator[88].

In our case, to answer how seeding conditions affect stem cell proliferation, we need to be able to pattern small numbers of cells, with and without cell contact, and monitor their proliferation over time. The use of microwells in its current state only enables short-term assays (usually < 24 hours), before the cells start to proliferate and require additional space. In addition, while microwells can pattern small clusters of cells inside a microwell (allowing cell-cell contact), they do not offer precise enough patterning resolution to pattern single cells close together (but without cell-cell contact). Therefore, to combine the benefits of the microwell mentioned above, while still enabling increased patterning resolution and room for cell proliferation, we created a new cell patterning tool called the Bio Flip Chip (BFC). Essentially, it traps the cells exactly like other microwell applications, depositing a single-cell solution onto an array of PDMS microwells and washing away the cells outside the microwells. However, the BFC then takes an additional step that enables some powerful capabilities. By flipping the microwell array upside down onto another substrate, the cells fall out onto an unconfined area. While still retaining the same pattern as when they were in the microwells, the cells now have room to proliferate and move. In addition, having the flexibility to pattern cells onto any substrate allows us to seed mESCS on their standard *in vitro* substrate of tissue-culture polystyrene (TCPS). We describe the development and use of the BFC in detail in Chapter 4.

During the time we were working on the BFC, Love *et al.* used microwells in a similar fashion for another elegant application[91] (Figure 1-11). By trapping single cells in microwells, they also flipped the microwell chip upside down, onto a glass slide. But, instead of patterning cells, they patterned the cells' secreted products on the glass slide. Those products were then recovered and identified, while the cells were still retained in their original microwells, allowing subsequent recovery of desired cells for clonal expansion. This technology has already been successfully used for fast antibody screening and efficient isolation of monoclonal hybridomas.

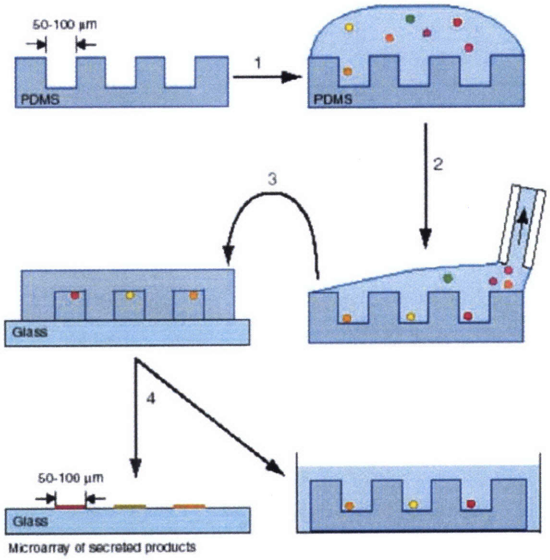

Figure 1-11: Flipping cells in microwells to recover their cell-secreted products[91].

1.6 Scope of the Thesis

The primary goal of the thesis is to develop a cell patterning technology that allows precise control of the stem cell environment, allowing us to modulate cell-cell signaling and monitor cell proliferation over time.

In Chapter 2, we describe the initial design and development of our DEP cell patterning technology, using beads as model particles. In Chapter 3, we describe the challenges associated with transitioning from beads to cells, along with creation of our second generation DEP trap, designed for use with cells. In Chapter 4, we describe the design and development of a new cell patterning technology, the Bio Flip Chip (BFC), and demonstrate the numerous capabilities this technology has to offer. In Chapter 5, we use the BFC to control the mouse embryonic stem cell (mESC) microenvironment to answer the question – why do mESCs need to be seeded as single cells? We finish in Chapter 6 with remarks on the significance of the thesis, ongoing collaborations to extend the BFC applications, and directions for future work.

Chapter 2: DEP Bead Trapping

Now that we have presented an overview of our cell patterning technologies – DEP traps and the Bio Flip Chip – we will further describe the functionality of each technique. In this chapter, we present a novel nDEP trap geometry that is strong and capable of single-cell trapping[45]. We demonstrated the trap strength by measuring the maximum flow rate that test particles could withstand while remaining trapped, and matched this to our predictive model with excellent agreement. In addition, the model provided us with a clear understanding of how our traps work and allowed us to create a set of design rules describing how the trap behavior changes as a function of the trap geometry.

2.1 The nDEP Square Trap

2.1.1 nDEP Square Trap Design

In the Introduction, we motivated the requirements of patterning mESCs and determined that the trap needed to be a planar, single-cell nDEP trap that had multidirectional stability and was strong enough to hold cells against substantial fluid flows. To create a trap with *x*- and *y*-directed stability, we decided to use a similar principle as the quadrupole electrodes and closely surround the particle with stabilizing electrodes. However, since the quadrupole geometry lacks *z*-directed stability, we decided to try a variation of this geometry and combine the four separate electrodes into a single surrounding electrode (Figure 2-1A). To minimize the loading of multiple particles, we made the surrounding electrode just bigger than the size of the desired cell. Furthermore, since cells are spherical, we first tried a circular electrode geometry. However, the circular geometry was not optimally strong because the curving electrode splits up the DEP force into *x* and *y* components, providing less force to counteract the *x*-directed flow (Figure 2-1B).

Therefore, in order to hold against higher velocity flows, we decided to remove the curvature, thus maximizing the *x*-directed DEP force. This provides us with two possible geometries for the simplest surrounding electrode, a rectangle and a square. Rectangular geometries did have an increased trap strength due to this higher *x*-directed DEP force, but also had an increased probability of trapping more than one particle in the trap (Figure 2-1C). Therefore, to maximize trap strength and the probability of single-cell trapping, we chose a square electrode geometry for our nDEP trap (Figure 2-1D).

However, we still needed an opposite polarity electrode to create the electric field, and in order to maximize trap strength, we wanted it close to the square electrode. We chose a simple line electrode, placed 10 μm away from the square electrode (Figure 2-1E). This was a large enough distance to allow us to still use a transparency mask for processing, allowing lower fabrication costs, while still being close enough to produce a strong DEP trap.

Finally, returning to the requirement for *z*-directed stability. It turns out that this square and line electrode trap creates a unique electric field geometry, producing the required downward DEP force inside the trap, thus providing stability in the *z*-direction (Figure 2-1F). We describe this unique geometry of the force fields in detail in Section 2.3.2: Size-Selectivity Behavior.

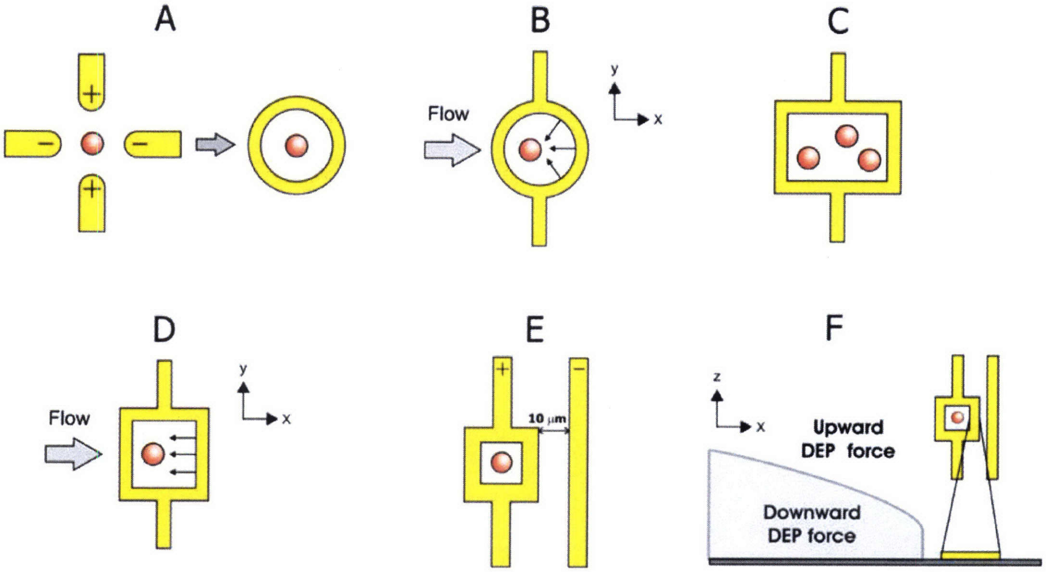

Figure 2-1: nDEP square trap design. (A) Instead of using a quadrupole geometry, we chose to surround the trapped particle with a single electrode. (B) The circular electrode geometry splits the DEP force into *x* and *y* components, providing less force to counteract the *x*-directed flow. (C) The rectangle electrode increased the probability of trapping more than one particle. (D) The square geometry provided a higher DEP force to counteract the *x*-directed flow. (E) We made the opposite polarity electrode a line electrode, spaced 10 μm away from the square electrode edge. (F) This nDEP square trap has a downward DEP force within the square electrode, thus providing stability in the *z*-direction.

2.1.2 nDEP Square Trap Operation

The operating scheme for our single-particle traps consists of three steps. First, with the flow on and the traps off, we initially flood the patterning space with a high density solution of particles (Figure 2-2A). Because of the *z*-directed DEP forces outside the trap (Figure 2-1F), particles are only able to be trapped if they initially reside within the inner square electrode. Therefore, we initially flood the patterning space with an excess of particles, increasing the probability that at least one particle will be located within the trap. The flooding time is small because the particles can be flowed in at very high speeds, being limited by the maximum pressures the flow chamber can withstand. The flooding time will then be a function of the maximum flow rate and the combined chamber and tubing volume. The smaller this combined volume, the less time it takes for flooding.

Once the patterning space is covered with particles, with enough particles filling the square traps, we turn off the flow and then turn the traps on (Figure 2-2B). The time needed for trapping is negligible, usually within seconds. The particles in the trap are forced into the electric field minimum, which without flow, is in the center of the square electrode. The particles outside of the square electrodes also align with the minimum electric field, which is located in between the traps in the array (Figure 2-2B).

Third, with the traps on, we turn the flow on, washing away the untrapped particles and leaving only single particles within each trap (Figure 2-2C). This wash step is usually the rate-limiting step in patterning particles since the flow rate cannot exceed the maximum flow rate of the trapped particle. Therefore, we require a strong trap that allows high enough flow rates for practical experimental times. The wash time is also dependent on the combined chamber and tubing volume, so minimizing this volume will help to reduce wash times. Once the particles are washed away, leaving only particles within the traps, the flow and the traps can be turned off.

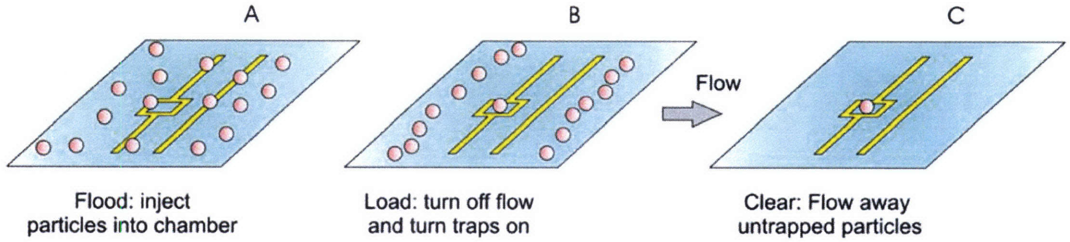

Figure 2-2: nDEP square trap operation. (A) Flood the patterning space with a high-density solution of particles. (B) Turn off the flow and turn on the DEP traps. (C) Turn on the flow and clear away the untrapped particles.

2.2 Materials and Methods

2.2.1 Beads and Bead Stock Solutions

We used polystyrene beads, with density of 1.062 g/cm^3, at five different bead diameters. The 4.2- and 8.2-µm diameter beads (Polysciences), with standard deviation of 0.33 and 0.17 µm respectively, were packaged as 1% solids in water. We made these bead solutions by using a 2.0-mL aliquot of the beads, washed in 1.0 mL of stock solution, and resuspended in 1.0 mL of stock solution.

The polystyrene beads (incorporating 2% divinyl benzene) with diameters of 9.7, 14.2, and 19.5 µm (Bangs Laboratories) with standard deviations of 0.10, 0.72, and 0.31 µm respectively, were packaged as 10% solids in water. We made these bead solutions by using a 0.5-mL aliquot of these beads, washed in 0.5 mL of stock solution, and resuspended in 1.0 mL of stock solution.

Bead stock solutions were made with conductivity of 0.01 S/m by combining appropriate volumes of 18.2-MΩ-cm deionized water and Dulbecco's PBS (Gibco), both containing 0.1% Triton X-100 (Sigma). Conductivities were measured using a conductivity meter (Thermo Orion, 555A).

2.2.2 Electrode Traps

We fabricated the DEP traps by patterning gold onto glass slides. We cleaned standard microscope slides of 38 × 75 mm in a Piranha solution (3:1 H_2SO_4:H_2O_2) for 10 min, blow dried them with N_2, and then dehydrated them in a 225 °C oven for 30 min (Figure 2-3A). We coated the slides with Hexamethyldisiloxane (HMDS oven, recipe #4) and then coated them with image-reversal photoresist (Hoechst, AZ-5214), dispensed at 500 rpm for 6 s, spread at 750 rpm for 6s, and ramped to 3000 rpm for 30s (Figure 2-3B). After spinning, we baked the slides in an oven at 95 °C for 30 min. Afterward, we exposed the slides to a UV dose of 390 mJ/cm^2 on a contact aligner (Karl Suss, MA6 Mask Aligner) using a dark-field mask printed at 40,640 dpi (Fine Line Imaging). We placed the slides on a 125 °C hotplate for 10 min. We then flooded the slides with a 1200 mJ/cm^2 on the same contact aligner (Figure 2-3C) and developed them for 2.5 min (AZ422-MIF developer). We then deposited them with metal, 250 Å of titanium and 2500 Å of gold (Figure 2-3D). Lastly, liftoff was performed by developing the slides in acetone for 30 min (Figure 2-3E).

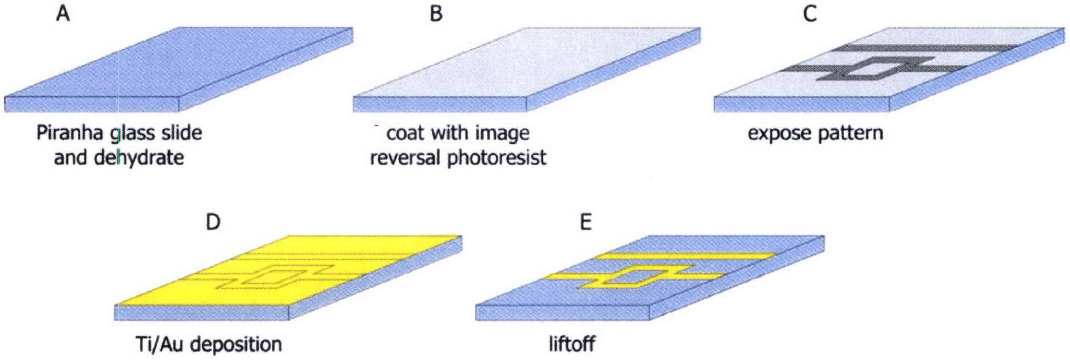

Figure 2-3: nDEP square trap fabrication. (A) We cleaned the slides in a Piranha solution and dehydrated them at 225 °C. (B) Then we coated them with image reversal photoresist (Hoechst AZ-5214). (C) Next we exposed the pattern using a transparency mask. (D) Then we deposited the Ti and Au. (E) Lastly, we performed liftoff using acetone.

The traps were designed as one square electrode with inner square side length (ISSL) of 25 μm and another line electrode spaced 10 μm away. All electrode widths were 10 μm (Figure 2-4A). The as-fabricated trap dimensions differed from the designed dimensions submitted to the transparency mask manufacturer (Figure 2-4B). This is because our minimum feature size of 10 μm is also the minimum allowed by the mask manufacturer, and the variance at this feature size is 3.2 μm. In addition, variations in photolithography exposure times significantly changed the trap dimensions and our exposure times were chosen to yield as-fabricated dimensions that were closest to the designed dimensions. However, this discrepancy in designed and as-fabricated trap dimensions did not significantly affect the trapping behavior. For example, using a 5 V_p applied voltage to trap a 12-μm-diameter bead, the maximum flow rate was 43 μL/min using the designed trap geometry and 44 μL/min using the as-fabricated geometry, a difference of only 2%.

The DEP traps were designed in a 5×5 square array, with a trap-to-trap distance of 200 μm (Figure 2-4C). The minimum feature size of the traps is ≥ 10 μm, which allows the use of inexpensive transparency masks for photolithography (CAD Art Services).

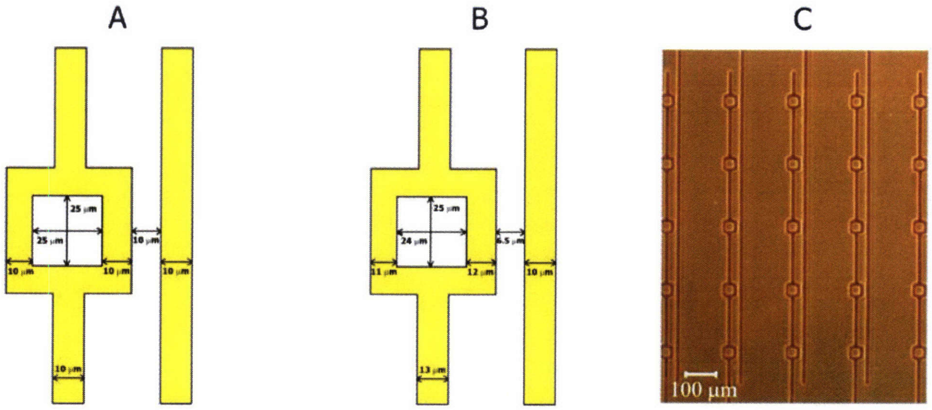

Designed

As-fabricated

Figure 2-4: Overview of the DEP trap and trap array. The DEP geometry consists of a square electrode and a line electrode. (A) The designed trap dimensions. (B) The as-fabricated trap dimensions. (C) A micrograph of the fabricated 5x5 trap array.

2.2.3 Flow Chamber, Packaging, and Fluidics

The flow chambers were made using a Si master wafer to mold the polydimethylsiloxane (PDMS) gasket. The Si wafers were cleaned for 10 min using the same Piranha solution described above, blow dried with N_2, and dehydrated for 10 min at 130°C. Photolithography was then performed using SU8-50 (Microchem) to define the flow chamber patterns. The wafers were developed for 10 min using PM acetate (Doe and Ingalls) and then silanized for 30 min using hexamethyldisiloxane (Shin-Etsu MicroSi). PDMS (Sylgard 184, Dow Corning) was then poured over the master Si wafer to form a gasket, using the "sandwich molding process[92]. The PDMS gasket was then plasma oxidized and bonded to a standard (25×75 mm) microscope slide and two holes were drilled to define inlet and outlet ports for the tubing. The tubing was epoxied (Radioshack, Quick Setting Epoxy) to this chamber top. The chamber top was then clamped to the bottom electrode slide using 4 binder clips for easy assembling and disassembling. Wires were electrically connected to the electrodes using conductive epoxy (Circuit Specialists). An overview of the packaging is shown in Figure 2-5A.

For the fluidics, the two inputs of a 4-way valve (Upchurch Scientific, V-101D) were connected to a 5-mL syringe filled with beads and a 10-mL syringe filled with stock solution. The 10-mL syringe was controlled using a syringe pump (KD Scientific, 210C). One output on the 4-way valve was connected to 1/16" OD PEEK tubing (Upchurch Scientific, 1536) and the other was connected to waste. The 1/16" OD tubing was then adapted to the 1/32" OD PEEK tubing (Upchurch Scientific, 1575) at the inlet on the flow chamber top. The 1/32" OD tubing connected to the outlet on the flow chamber top was connected to waste. The fluidics setup is shown in Figure 2-5B.

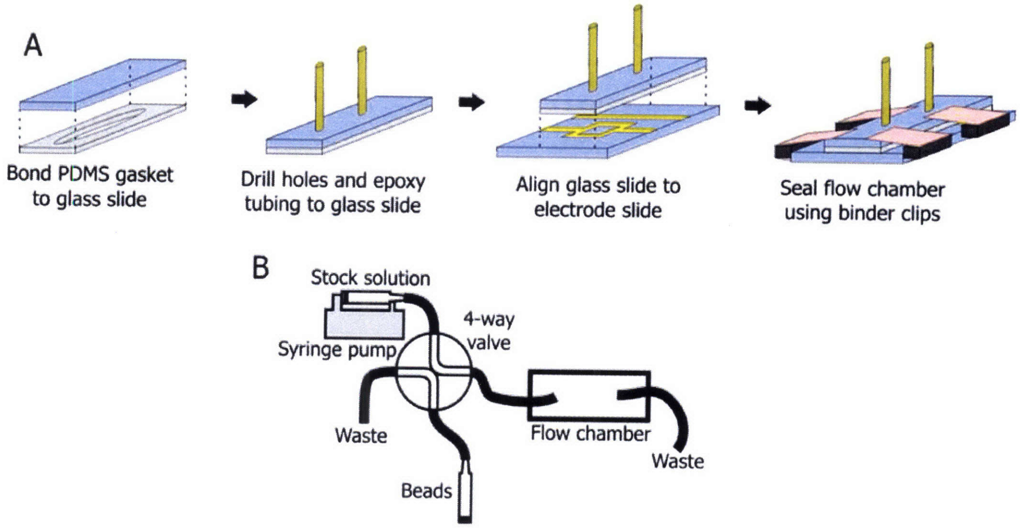

Figure 2-5: Overview of the flow chamber, packaging, and fluidics. (A) Flow chamber packaging involved bonding a glass slide to a PDMS gasket, drilling holes into the top chamber and epoxying tubing, and aligning and sealing to the electrode slide using 4 binder clips. (B) The fluidics consisted of one free syringe and one syringe powered by a syringe pump, connected to a 4-way valve, with valve output connected to the flow chamber. The flow chamber output was connected to waste.

2.2.4 Optics and Measuring Chamber Height

An automated upright microscope (Zeiss Axioplan 2 imaging) was used in the bead experiments and an inverted microscope (Zeiss Axiovert 200), along with a SPOT digital camera (Diagnostic Instruments), was used to take pictures of the trap geometries to determine as-fabricated trap dimensions.

We measured the flow chamber height with an automated microscope by focusing on the electrodes on the bottom glass slide and then focusing on the top of the PDMS gasket. The difference between the two focus points was called the chamber height. The microscope has a motorized focus, allowing a minimum step resolution of 25 nm.

Since the device flow chamber is sealed using binder clips, the height of the flow chamber varied depending on how the slides were clipped together. Because the HD force is very sensitive to the flow chamber height (Eq. 1-6), the flow-chamber height was measured at the same location in the flow chamber, twice before the experiment and once after the experiment. These three values were averaged together to give the height used in the model. The two chamber heights measured before the experiment differed by up to ~5 μm, due to the variability in focusing on the substrate. The chamber height after the experiment never varied by more than ~2 μm from the before measurements, suggesting that the chamber height did not significantly drift over the course of the experiment. Bead experiments for bead diameters 4.2 and 8.2 μm were performed sequentially with the same experimental setup at a flow chamber height of 103 μm and bead diameters 9.7, 14.2, and 19.5 μm were performed sequentially with the same experimental setup at a flow chamber height of 95 μm.

2.2.5 Determining Peak Holding Diameter

For the design rule simulations, to be objective in choosing the peak holding diameter from the size-selectivity curves, the curves were cubically fit using MATLAB and the peak holding diameter was chosen as the diameter at the peak maximum flow rate.

2.2.6 Electrical Excitation

Sine wave excitation at 5 MHz was generated by a signal generator (Agilent, 33250A). One trap electrode was set to ground while the other trap electrode was set to either 0, 1, 2, 3, 4, or 5 V_p (peak voltage), while the signal was measured using a digital oscilloscope (Tektronix, TDS 2024) and found to be 0, 1.08, 2.08, 3.08, 4.08, and 5.08 V_p.

2.2.7 Bead Experiments

The flow chamber was initially primed with ethanol to remove any bubbles and then flushed with stock solution to remove the ethanol from the chamber. The bead solution was then injected into the flow chamber so the maximum number of traps in the 5×5 array had beads in them ($n \geq 3$). The signal generator was turned on to 5 V_p, trapping beads that were already inside the square electrode. The syringe pump was then turned on and stock solution was flowed through the chamber at 20 μL/min to clear all the untrapped beads from the field. The flow rate was then set to 1 μL/min so the signal could be set to the desired voltage without losing any of the trapped beads. The flow rate was then stepped up, at 1 μL/min intervals, until the maximum flow rate was reached. The maximum flow rate was determined to be the highest flow rate at which the beads would remain trapped for 1 min, observed through the microscope. This time was chosen empirically by observing that beads held for 1 min, if the flow was continued, would usually (> 90%) be held indefinitely. The maximum flow rate was recorded for all the trapped beads in the array. Then the procedure was repeated at a different applied voltage. For each bead diameter, maximum flow rate measurements were made every 1 V_p from 0-5 V_p.

2.2.8 Modeling Parameters

We generated electric field data from simulations using the commercial field solver FEMLAB (Comsol) (Figure 2-6). The simulated domain includes a flow chamber with variable height, sandwiched between two 1-mm-thick glass slides. The boundary conditions are electric potential on the electrodes, electric insulation on the outer surfaces, and continuity at the interfaces of different materials in the system. Field data is written to a 3-D grid, using a grid spacing of 1.0 μm, and smoothed using a Gaussian low-pass filter. Simulations are run using a 5V_p (peak voltage) potential difference between electrodes. We evaluate results for other applied voltage differences by scaling the electric field, using the linear dependence of electric field on voltage.

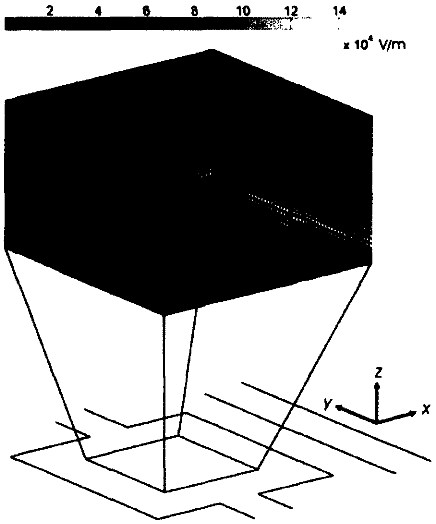

Figure 2-6: Electric-field magnitude (in V/m) inside a DEP trap at an applied voltage of 5 V_p. The contour lines show the lines of equal electric-field magnitude.

The simulations were performed on polystyrene beads with a bead density of 1062 kg/m^3, medium density of 1000 kg/m^3, bead conductivity of 2×10^{-4} S/m and relative permittivity of 2.5, in media with a conductivity of 0.01 S/m and relative permittivity of 80.

The applied signal was always a sine wave at 5 MHz. For the bead experiment simulations, the maximum flow rate was determined for each of the bead diameters as a function of the measured voltages of 0, 1.08, 2.08, 3.08, 4.08, or 5.08 V_p. For the size-selectivity simulations, the maximum flow rate was determined at a fixed voltage of 5.08 V_p, as a function of bead diameter that ranged from 2-24 μm, with 2-μm resolution. For the design rule simulations, the maximum flow rate was determined as a function of electrode geometry, at a fixed voltage of 5 V_p.

The flow chamber geometry was 3-mm wide. The chamber height was either 95- or 103-μm high for the bead experiment simulations, 95 μm for the size-selectivity simulations, and 100 μm for the design rule simulations. All simulations used a flow rate resolution of 1.0 μL/min. The bead experiment simulations (shown in Figure 2-7 and Figure 2-8) used the as-fabricated geometry (Figure 2-4B) while the design rule simulations (shown in Figure 2-9 and Figure 2-10) used the designed trap geometry (Figure 2-4A).

2.3 Results

Since flowing away untrapped cells is often the rate-limiting step during cell patterning, with the fluid flow limited by the maximum *x*-directed DEP force, the DEP traps need to be strong. To demonstrate the strength of our DEP traps, we used beads as model particles to measure the flow rate that test particles could withstand while remaining trapped. Compared to cells, beads are simpler to model and have less variability in size, making them an ideal particle for trap proof-of-concept[59,61,62,67,93,94]. The measurements were in excellent agreement with our modeling predictions. By modeling the maximum flow rate as a function of bead diameter, we were able to determine that the trap displayed a size-selectivity behavior, being optimized to hold ~9 μm diameter beads.

2.3.1 Bead Experiments

For each bead diameter of 4.2, 8.2, 9.7, 14.2, and 19.5 μm, maximum flow rate measurements were made every 1 V_p from 0-5 V_p, allowing us to generate the holding characteristic for the trap (Figure 2-7). We then compared these measurements to predictions generated by our modeling software. Each subfigure represents a different bead diameter and plots the predicted and experimental maximum flow rate versus the applied voltage. The maximum flow rate always increased as the applied voltage increased. In addition, at 0 V_p the maximum flow rate was always zero, suggesting that the beads did not stick to the glass slide. The difference between the predictions and experimental mean was found to be ≤ 16% in all cases, except for the 4.2 μm beads which had a difference of 26%. The difference was calculated as:

$$\frac{\left|Q_{\text{exp}} - Q_{\text{model}}\right|}{Q_{\text{model}}} \tag{2-1}$$

where Q_{exp} is the experimental mean maximum flow rate at a given voltage and Q_{model} is the predicted maximum flow rate at a given voltage. These maximum flow rate measurements were shown to be repeatable over different days.

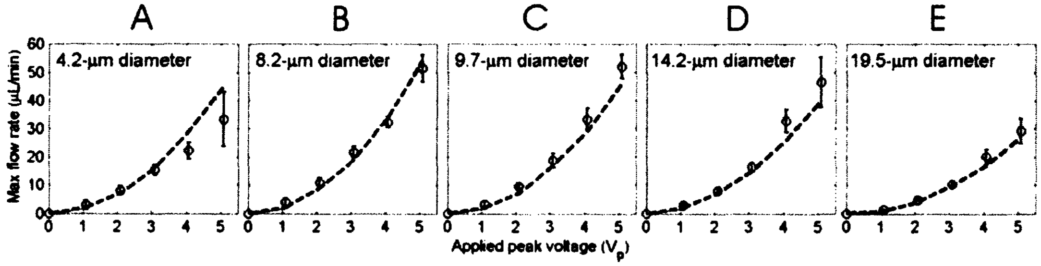

Figure 2-7: Experimental and simulated results for 5 different diameter beads. We vary the applied voltage from 0-5 V_p and measured the maximum flow rate at which the beads are still trapped. Bead diameters are (A) 4.2 μm (B) 8.2 μm (C) 9.7 μm (D) 14.2 μm (E) 19.5 μm. Shown are the predicted values (--), mean (o), and standard deviation (–) (n ≥ 3, at least 3 of the 25 traps were filled at each voltage). Model and experiment differ by ≤ 16% in all cases, except for the 4.2 μm beads which had a difference of 26%.

Over the course of all the experiments, certain traps in the 5×5 array were repeatedly stronger while others were repeatedly weaker, which we believe is the major contributor to the standard deviation in the experiments. In order to understand this observed behavior, we analyzed the differences in maximum flow rate caused by variations in the most sensitive parameters in the system – the trap geometry, the bead size, and the flow chamber height. The upper and lower limits for these parameters were used to calculate the upper and lower limits for the maximum flow rate. By taking the difference of these flow rates and dividing by the average, we were able to calculate a contribution to the variability.

There were variations in trap geometry due to fabrication heterogeneity, so we measured the dimensions of both the strongest and weakest DEP trap and used our modeling software to determine how it affected the maximum flow rate. Most dimensions differed by less than 1 μm, with maximum flow rates that yielded a ~7% contribution to variability. Although the standard deviations in bead sizes were all < 1 μm, we looked at how differences in bead diameter of ± 1 μm affected the maximum flow rate. Our model predicted that these bead variations caused a contribution to variability of ~13%. Finally, we looked at variations in flow chamber height because we noticed that the stronger and weaker traps were located on different sides of the 5×5 array, suggesting that the flow chamber height was non-uniform across the array. We measured the flow chamber height three times at both sides of the array and found a height difference of ~7 μm, which caused differences in maximum flow rates that yielded a contribution to variability of ~13%. This variation in flow chamber height is probably due to differences in clamping force for the 4 binder clips or non-uniform height of the PDMS gasket.

2.3.2 Size-Selectivity Behavior

Using the 5 V_p data of each bead diameter from Figure 2-7, we can plot the maximum flow rate as a function of bead diameter (Figure 2-8A). Since the 4.2 and 8.2 μm bead diameter experiments were performed at a different flow chamber height than the other three bead diameter experiments, we normalized the experimental maximum flow rate for these two smaller bead sizes. As the maximum flow rate is determined by the detailed interactions between the DEP, drag, and gravitational forces, we chose to normalize the experimental maximum flow rate numerically by using the ratio of the simulated maximum flow rates at both chamber heights.

Since the DEP force increases with R^3 (Eq. 1-1), we would expect the maximum flow rate to increase with bead size for a given DEP trap. However, in our trap, the maximum flow rate increases and then decreases with bead diameter, creating a size-selectivity behavior that is optimized for ~9 μm particles. The trapped bead experiences *x*, *y*, and *z*-directed electric fields and is pushed out of the trap when its center of mass sees upward *z*-directed electric fields, pushing it up into higher shear flows and therefore out of the trap. The bead remains trapped when the bead center of mass experiences the downward *z*-directed electric fields. The line defining the transition from upwards to downwards *z*-directed electric fields – the stability transition line – was determined from the modeling software to have the shape in Figure 2-8B. Although the trap has strong enough *x*-directed electric fields to resist flow rates > 100 μL/min, it is the upward *z*-directed fields that push the beads out of the trap at lower flow rates. Therefore, this stability transition line is the critical determinant of the size-selectivity behavior.

The size-selectivity behavior occurs because of two effects. First, at low flow rates, the geometry of the electric fields pushes larger beads further away from the right side of the square electrode (RSSE), allowing them to travel a greater distance in the +*x*-direction (to the right) before they get to the upward *z*-directed electric fields near this electrode (Figure 2-8C). Second, at higher flow rates the beads are pushed to the right, towards the upward *z*-directed fields near the RSSE. The smaller-diameter beads started out closer to the RSSE, so with flow they get pushed near this electrode and experience the upward *z*-directed fields there (Figure 2-8D, top). The larger-diameter beads have centers of mass that are high enough to experience the upward *z*-directed fields further away from the RSSE (Figure 2-8D, bottom). The medium-sized beads do not experience the upward *z*-directed fields until higher flow rates, making the trap optimized for these bead sizes (Figure 2-8D, middle).

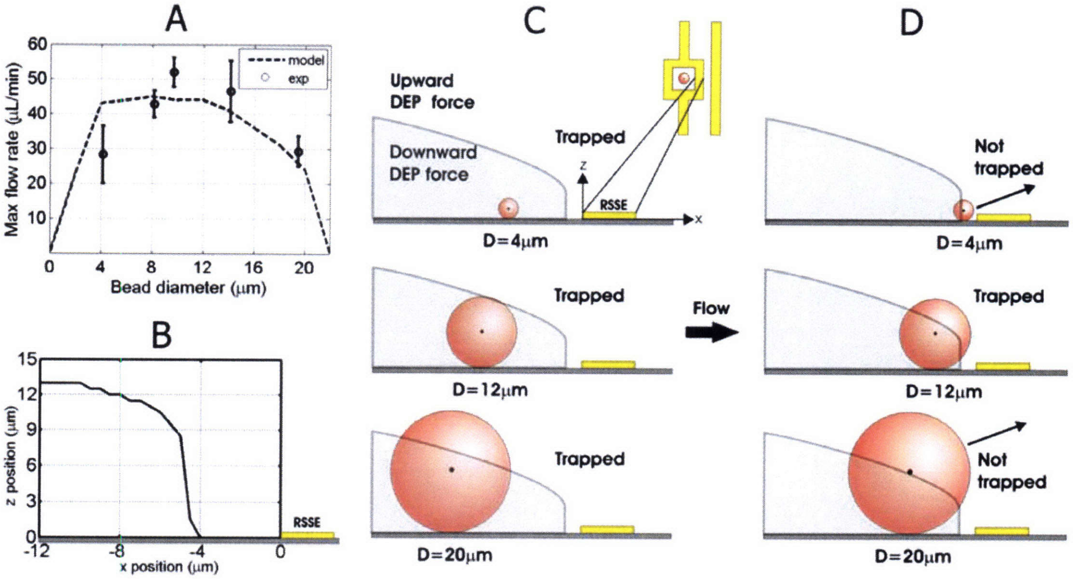

Figure 2-8: Size-selectivity behavior. (A) Experimental and simulated results for all bead diameters at a 5 V_p, 5 MHz applied signal. Shown are the predicted values (--), mean (o), and standard deviation (–) (n ≥ 3 at each voltage). Experimental results were normalized for flow chamber height variations between experiments. (B) The stability transition line was determined from the modeling software. (C) Low flow rates. All bead centers are in the stable region such that the bead is being pushed down by the downward DEP force. Importantly, larger beads are trapped further away from the right side of the square electrode (RSSE). (D) High flow rates. Upon starting flow, the beads are pushed to the right. Both smallest and largest bead centers leave the stable region and are pushed out of the trap by the upward DEP force, while the medium-sized beads do not leave the stable region until higher flow rates are reached.

2.3.3 Multiple- and Single-Bead Trapping

The 4.2, 8.2, and 9.7 μm beads were small enough to have multiple beads trapped inside the inner square area, while the 14.2 and 19.5 μm diameter beads were large enough that we never observed trapping of more than one bead. When the traps were turned on with two of these larger beads inside, the additional bead would always be pushed out of the trap, leaving one remaining trapped bead. Therefore, one can ensure single-particle trapping using size exclusion. Our 25 μm-ISSL trap was shown to ensure single-particle trapping for beads ≥ 14.2 μm. Thus, to ensure single-particle trapping, we recommend a square trap with ISSL that is < 10 μm bigger than the diameter of the desired particle. And although this trap is optimized for ~ 9 μm particles, the difference in maximum flow rate between 9 and 14.2 μm bead diameters is < 5 μL/min (Figure 2-8A), a minimal decrease in trap strength. Overall, we demonstrated a strong, planar, nDEP trap that is capable of single-particle trapping.

Besides size exclusion, another way to ensure single-particle trapping is using flow. It was observed during the 4.2, 8.2, and 9.7 μm bead experiments that when there were multiple beads trapped inside the inner square, the multiple-particle maximum flow rate was less than the single-particle maximum flow rate. When the flow rate exceeded the multiple-particle maximum flow rate, sometimes all of the beads were removed at once, while other times only some of the beads were removed until a single bead remained in the trap. Therefore, one could operate the flow rate near the single-particle maximum flow rate so multiple particles are unable to remain trapped.

2.3.4 Design Rules

Because the bead-trapping experiments show excellent agreement with our predictions, we can use the modeling software to extend beyond the experimental space and develop a set of design rules to tune the size-selectivity behavior shown in Figure 2-8A. This allows us to design traps optimized for placing cells of various sizes. We show that changing the electrode inner square area and the spacing between electrodes grants us the freedom to optimize the traps for a specific particle size.

Since it is the *z*-directed electric fields that determine the stability of the trap, this stability transition line is the critical determinant of the size-selectivity behavior. Therefore, when analyzing how changing the trap dimensions affects the size-selectivity behavior, we only needed to look at the stability transition line. For instance, increasing the slope of the stability transition line allows larger particles to remain in the downward *z*-directed electric fields, and therefore increases the peak holding diameter, the bead diameter where peak holding occurs. Shifting the stability transition line further from the RSSE decreases the magnitude of the maximum flow rate because it takes less flow to push the particles into the upwards *z*-directed electric fields, but with the slope unchanged, will not change the peak holding diameter.

We simulated varying the electrode inner square side length (ISSL) from 15-35 μm (Figure 2-9A). The maximum flow rate was calculated at 5 V_p as a function of bead diameter for a given ISSL (Figure 2-9B). As the ISSL increases, the stability transition line increases in slope (Figure 2-9C), causing the peak holding diameter to increase (Figure 2-9D). As the ISSL increases, the stability transition line also shifts further from the RSSE (Figure 2-9C), causing a decrease in the maximum flow rate magnitude (Figure 2-9E). Notice that for the smaller ISSL traps, the size-selectivity curve ends before 24 μm. This is because these larger beads experience the upward *z*-directed electric fields no matter where they are in the smaller inner square area traps, causing them to be pushed out of the trap even at zero flow. Therefore, as the ISSL decreases, the size-selectivity curve ends at smaller bead diameters with larger peak maximum flow rates, making the degree of size-selectivity more pronounced. The converse is also true: as the ISSL increases, the degree of size-selectivity becomes less pronounced.

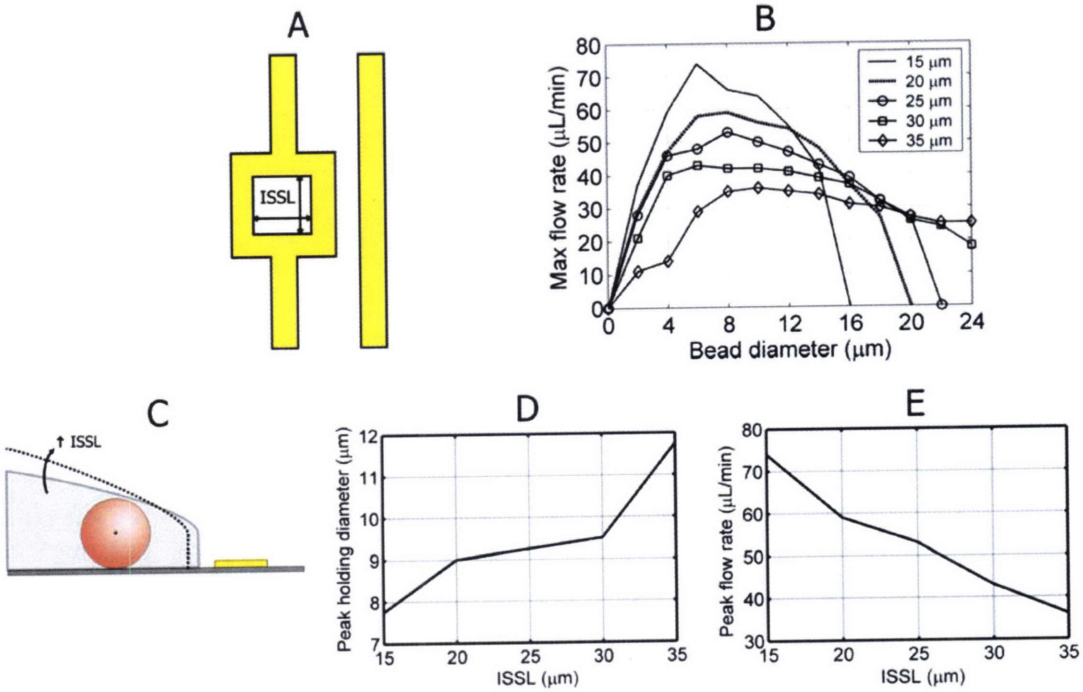

Figure 2-9: Size-selectivity behavior due to changing inner square side length (ISSL). All other dimensions were held constant. (A) The ISSL was varied from 15-35 μm to determine the effects on size-selectivity behavior. (B) The maximum flow rate was calculated at 5 V_p as a function of bead diameter for a given ISSL. (C) Increasing the ISSL increases the slope of the stability transition line and shifts it further away from the RSSE. (D) As the ISSL increases, the peak holding diameter increases. The peak holding diameter was determined by cubically fitting the size-selectivity curves. (E) As the ISSL increases, the maximum flow rate magnitude decreases.

Varying the ISSL was designed to allow control over the peak holding diameter, but additionally affected the maximum flow rate magnitude. Therefore, we wanted to find a way to independently control the maximum flow rate magnitude. We did this by varying the spacing between the electrodes (SBE) from 5-25 μm (Figure 2-10A) and calculated the maximum flow rate at 5 V_p as a function of bead diameter (Figure 2-10B). As SBE was varied, the stability transition line did not significantly change, so the bead peak holding diameter stayed roughly the same (Figure 2-10C). However, as the SBE increases the electric fields become weaker, causing the maximum flow rate magnitude to decrease (Figure 2-10D).

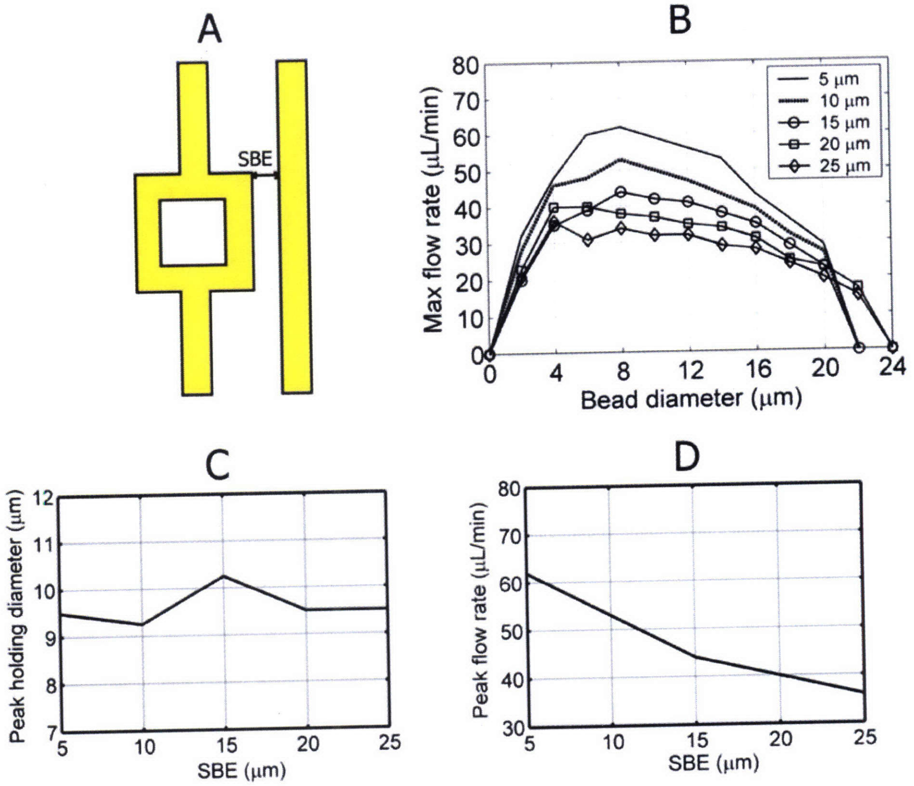

Figure 2-10: Size-selectivity behavior due to changing spacing between electrodes (SBE). All other dimensions were held constant. (A) The SBE was varied from 5-25 μm to determine the effects on size-selectivity behavior. (B) The maximum flow rate was calculated at 5 V_p as a function of bead diameter for a given SBE. (C) As the SBE increases, the peak holding diameter stays roughly the same. The peak holding diameter was determined by cubically fitting the size-selectivity curves. (D) As the SBE increases, the maximum flow rate magnitude decreases.

In addition to varying the ISSL and SBE, we also varied the actual electrode width and the inner square length and width independently. Although these variations produced similar size-selectivity profiles to those generated by varying ISSL and SBE, these variations did not offer any additional ways to tune the profiles – they also only altered the bead diameter where peak holding occurs and the maximum flow rate magnitude. Therefore, by varying only the ISSL and SBE, we maintain the trap geometry in its simplest form, keeping the inner electrode shape as a square and all electrode widths as 10 μm.

2.4 Discussion

The bead experiment results showed remarkable agreement with our modeling predictions, without the use of fitting parameters. Our modeling software has now been validated numerous times[45,61,67,76], enabling one to design and evaluate a new trap's performance against previously-used DEP traps (see Appendix A: Modeling Software Functionality), understand how a new trap works, and optimize its geometry – all before the trap is even fabricated. We have made this modeling software freely available to the public at: www.rle.mit.edu/biomicro.

Overall, we demonstrated the functionality of our strong, planar, single-particle nDEP trap using beads as model particles. While transitioning from beads to cells has been demonstrated repeatedly in the past[50,60,62,76,93], there are several issues that make this jump less than trivial. Since beads are not damaged by high strength electric fields, higher operating voltages can be used, making strong trapping against fluid flow much easier. Yet, cells *are* affected by electric fields that can damage them through cell heating or transmembrane loading, forcing us to use lower operating voltages that might not enable strong trapping. Furthermore, beads can be mixed with a surfactant to make them less sticky, preventing them from sticking to the glass bottom substrate or each other. Reducing stickiness in cells is much harder, and they tend to significantly stick to the glass substrate and clump with each other, reducing both pattern fidelity and single-cell trapping. These issues will be addressed in the next chapter.

Chapter 3: DEP Cell Trapping

In this chapter, we show how we model the media temperature rise and induced transmembrane voltage, allowing us to minimize effects on cell health while maximizing trap strength. In addition, we demonstrate efficient cell patterning with multiple cell types, using two generations of DEP traps. The second generation trap has the capability to minimize cell-substrate interactions, using DEP to levitate the cells outside the traps, preventing them from sticking to the glass substrate.

3.1 Materials and Methods

3.1.1 Cell Culture

We cultured ABJ1 mESCs with a stably integrated GFP reporter for Oct-4 without feeders in mESC media: DMEM (Invitrogen, 11960-044) supplemented with 15% ES-qualified fetal bovine serum (Invitrogen, 16141-079), 4 mM L-glutamine (Invitrogen, 25030-081), 1 mM non-essential amino acids (Invitrogen, 11140-050), 50 U/mL penicillin, 50 μg/mL streptomycin (Invitrogen, 15140-122), 100 μM β-mercaptoethanol (Sigma-Aldrich, M7522), and 500 pM leukemia inhibitory factor (Chemicon, ESGRO ESG1107).

We cultured 3T3 murine fibroblasts and HeLa cells in: DMEM (Invitrogen, 11960-044) supplemented with 10% bovine calf serum (Hyclone, SH30072.03), 4 mM L-glutamine (Invitrogen, 25030-081), and 50 U/mL penicillin, 50 μg/mL streptomycin (Invitrogen, 15140-122).

We cultured cells directly on 100×20 mm TCPS dishes (Corning, 430167) in a 37 °C humidified environment with 7.5% CO_2. For maintenance of cells, we fed cells daily and passaged using 0.25% trypsin-EDTA (Invitrogen, 25200-056). We passaged the ABJ1 cells every other day and the 3T3 and HeLa cells when they were 90% confluent, seeding all cell types at a density of $\sim 5\times10^5$ cells/cm^2.

3.1.2 Cell Solution

Since our traps use nDEP to position cells, we can use normal cell-culture media when trapping, measured to have conductivity of 1.5 S/m, using a conductivity meter (Thermo Orion, 555A). Our cell solution is cell-culture media with cells at a density of 1×10^6 cells/cm^2.

3.1.3 Cell Trapping Electrodes

The DEP traps were fabricated in a similar manner to the traps used in the bead trapping experiments (Section 2.2.2: Electrode Traps), however these electrodes were patterned onto pyrex wafers instead of glass slides. Patterning onto the glass slides often caused parts of the gold electrodes to rip off, either leaving missing parts in the electrode patterns or causing shorts between opposite polarity electrodes, which can sometimes render an entire electrode array useless. The pyrex wafers, however, turned out to be a much better substrate, creating electrode patterns that were much closer to our mask.

We cleaned 6" pyrex wafers in a Piranha solution (3:1 H_2SO_4:H_2O_2) for 10 min, followed by a spin rinse. We coated the wafers with hexamethyldisiloxane (HMDS oven, recipe #4) and then coated them with image-reversal photoresist (Hoechst, AZ-5214), dispensed at 0 rpm for 8 s, spread at 500 rpm for 6s, and ramped to 2500 rpm for 30s. After spinning, we baked the wafers in an oven at 95 °C for 30 min. Then we exposed the wafers to a UV dose of 30 mJ/cm^2 on a contact aligner (Electronic Visions, EV620 Mask Aligner) using a dark-field mask printed at 40,640 dpi (Fine Line Imaging). We placed the wafers in an oven at 95 °C for 30 min. We then flooded the wafers with a 600 mJ/cm^2 on the same contact aligner and developed them for 90 s (AZ422-MIF developer). We then deposited them with metal, 100 Å of titanium and 2000 Å of gold. Lastly, liftoff was performed by developing the wafers in acetone overnight, then continuing to develop in acetone for 15 min with the wafers floating in an ultrasonic bath. We then rinsed with Methanol and Isopropanol, followed by another spin rinse. Then the wafers were coated with a thick resist (Hoechst, AZ-4620), dispensed at 0 rpm for 8 s, spread at 500 rpm for 6s, and ramped to 2000 rpm for 20s. Finally, they were then baked at 95 °C for 1 hr, cut into separate chips using a diesaw, and developed in acetone to remove the thick resist.

For patterning cells, we used the same nDEP square trap design (Figure 2-4A). The square electrode had inner square side length (ISSL) of 25 or 35 μm, to accommodate various cell diameters, and the line electrode was still spaced 10 μm away, enabling us to utilize a transparency mask to reduce fabrication costs. All electrode widths were 10 μm. These DEP trap arrays consisted of a 10×10 square array, with a trap-to-trap distance of 200 μm. Our second generation DEP traps for cell patterning, the DEP Microwells (Figure 3-5B), used this same trap design, except with interdigitated electrodes (IDEs) spaced between the traps, helping to prevent cells from sticking to the substrate outside the traps.

3.1.4 Flow Chamber, Packaging, and Fluidics

The flow chamber, packaging, and fluidics were also similar to that used in the bead trapping experiments (Section 2.2.3: Flow Chamber, Packaging, and Fluidics), however we made the PDMS gasket for the flow chamber (Figure 2-5A) using a significantly easier method. Rather than forming the gaskets around microfabricated SU8 features, requiring extra fabrication costs and time, we instead stamped out the flow chambers using a metal stamp (MIT Machine Shop) and a PDMS sheet (Silicone Specialty Products).

3.1.5 Optics

An inverted microscope (Zeiss Axiovert 200), along with a SPOT digital camera (Diagnostic Instruments), was used to take pictures of cell trapping and measure the chamber height in the cell loading experiments.

3.1.6 Electrical Excitation

Sine wave excitation at 10 MHz was generated by a signal generator (Agilent, 33250A). One trap electrode was always set to ground. For the initial cell trapping experiments, the other trap electrode was set to 1 V_p. For the DEP Microwell trapping experiments, this electrode was initially set to 0.75 V_p during cell loading, and then increased to 1.25 V_p

when clearing away the untrapped cells at higher flows. For the cell loading experiments, this electrode was varied between 0.25, 0.5, 0.75, 1.0, and 1.25 $V_{p.}$

3.1.7 Resistor-On-Chip Experiments and Modeling

The resistor-on-chip (ROC) was placed between eight rows of twenty-four nDEP traps (Figure 3-1A-B). To calibrate the ROC, in order to determine electrical resistance as a function of temperature, we placed the chip on a hotplate and measured the resistance for a range of temperatures. Using a thermocouple placed over the ROC, it was determined that the temperature of the chip differed slightly from the temperature of the hotplate, so we used the thermocouple temperature as the measured temperature. We measured the resistance at five degree increments between 25-60 °C, allowing us to generate a resistance versus temperature curve (Figure 3-3A).

We then measured resistance as a function of applied signal voltage, with a flow chamber over our ROC (Figure 3-1C). We flowed 70% ethanol through the chamber at a low flow rate to remove any bubbles, using our fingers pressed against the flow chamber to apply pressure and keep a tight seal. We then flowed 1 mL of PBS through the chamber to make sure all the ethanol was cleared away and then let the flow stabilize to zero. Then, at a frequency of 10 MHz, we applied a voltage of 0, 2.5, 3.5, 4.5, 5.5V and recorded the ROC resistance.

For the FEMLAB modeling of the ROC, due to memory limitations, we used a quarter symmetry model, consisting of four rows of twelve DEP traps, with the resistor located on the symmetric boundary. We first solved for the electric fields (described in 2.2.8: Modeling Parameters) and then restarted the simulation to solve for temperature, using thermal insulation boundary conditions on the outer surfaces and heat flux on the interfaces of different materials in the system.

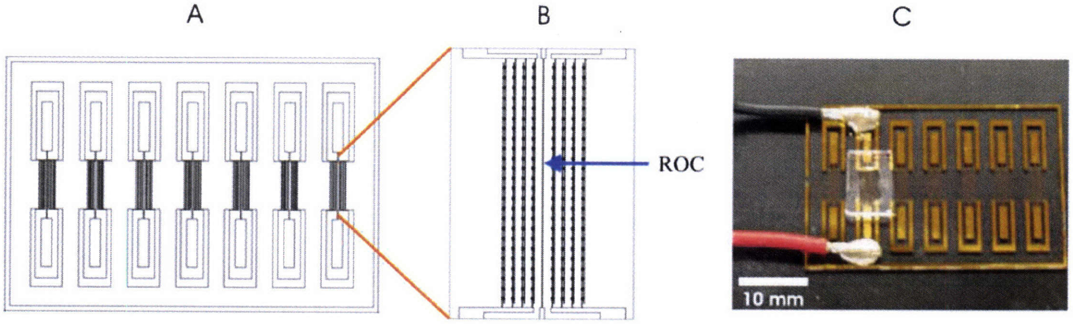

Figure 3-1: Resistor-on-chip (ROC) devices. Autocad layout of: (A) the entire ROC electrode slide and (B) one ROC array, showing the ROC between eight rows of twenty-four DEP traps. (C) Actual experimental setup with electrode slide and flow chamber over the ROC array.

3.1.8 Cell Health Modeling

When electric fields exist in a conductive medium, heating of the medium occurs, which can increase cell temperatures and damage cells. The power generation per unit volume of the media (W) is defined by[95]:

$$W = \sigma E^2 \tag{3-1}$$

where σ is the media conductivity.

Transmembrane loading occurs when the induced cell membrane voltage exceeds critical values, possibly causing electroporation or disruption of cell-cycle dynamics[96,97]. This maximal induced transmembrane potential, for a spherical cell, in a uniform electric field, assuming the cytoplasm and surrounding electrolyte are purely conductive (e.g., $\sigma \gg \omega\varepsilon\varepsilon_o$), is given by[98]:

$$V_m = \frac{1.5ER}{1+RG_m(\rho_i+0.5\rho_a)}\frac{1}{1+j\omega\tau} \tag{3-2}$$

where G_m is the membrane conductance, ρ_i is the cytoplasm resistivity, ρ_a is the media resistivity, and τ is defined as:

$$\tau = \frac{RC_m(\rho_i+0.5\rho_a)}{1+RG_m(\rho_i+0.5\rho_a)} \tag{3-3}$$

where C_m is the membrane capacitance. Because the membrane acts like an electrical high-pass filter, operating at applied signal frequencies in the MHz range and limiting the applied signal voltage helps to minimize transmembrane loading[96,97]. Therefore, we choose to operate our DEP traps at a frequency of 10 MHz.

3.1.9 Initial Cell Trapping Experiments

The flow chamber was initially primed with ethanol to remove any bubbles and then flushed with PBS to remove the ethanol from the chamber. Blank cell-culture media was then injected into the flow chamber, followed by a plug of cell solution. The traps are operated as described in detail in Section 2.1.2: nDEP Square Trap Operation (Figure 2-2). Briefly, with the flow on and the traps off, we initially flood the patterning space with a high density cell solution, maximizing the number of particles located inside the square electrodes. Second, we turn off the flow and then turn the traps on to 1.0 V_P. Third, with the traps on, we turn the flow on, washing away the untrapped cells.

3.1.10 DEP Microwell Experiments

The DEP Microwells are operated in a similar fashion, with some minor changes. First, when flooding the cells into the flow chamber, we keep the electrodes on at 0.75 V_P, allowing the IDEs to levitate the cells outside the DEP traps to prevent them from sticking to the glass surface there (Figure 3-2A). Second, keeping the electrodes on at 0.75 V_P, we use low flow (~10 μL/hr) to load the cells into the traps, letting them attach to the substrate (Figure 3-2B). Third, we increase the voltage to 1.25 V_P and increase the flow rate to ~100 μL/hr in order to wash away the untrapped cells (Figure 3-2C).

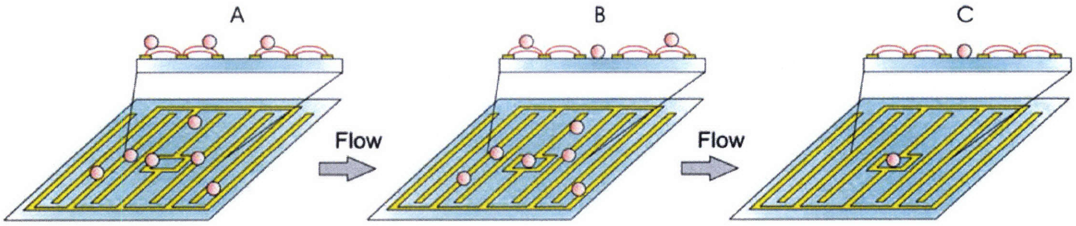

Flood: inject cells into chamber

Load: trap cells w/ low flow and let settle

Clear: Flow away untrapped cells

Figure 3-2: DEP microwell operation. (A) Flooding the cells into the flow chamber with the electrodes on, using the IDEs to prevent cells from sticking outside the traps. (B) Using low flow to load the cells into the DEP traps. (C) Increasing the voltage and the flow rate to wash away the untrapped cells.

3.1.11 Cell Loading Experiments and Modeling

The cell loading experiments were performed by flowing in cells into the flow chamber at a given flow rate, with the electrodes on at 0.25, 0.5, 0.75, 1.0, or 1.25 V_p. Although the flowed-in cells were located all over the trap array, we only observed cells that were flowing into and symmetrically aligned with the center of the square trap, since that is how we modeled the cells using our software. The maximum loading flow rate, at a given voltage, was determined to be the flow rate at which nine out of ten cells are able to successfully load into the DEP trap, without getting flowed away.

The electric fields were calculated as previously described (see Section 2.2.8: Modeling Parameters) and modeling was performed using the following parameters. The applied signal was a 10 MHz sine wave varied between 0.25, 0.5, 0.75, 1.0, and 1.25 V_p. The media density was 1000 kg/m^3 with a relative permittivity of 80. The solution conductivity was 1.5 S/m, which is the typical conductivity of cell-culture media.

We modeled all cells with a density of 1071 kg/m^3, a cell cytoplasmic relative permittivity of 75, and a cytoplasmic conductivity of 0.75 S/m. The cell membrane had a conductance of 22 mS/cm^2, a capacitance of 1.6 μF/cm^2, and a thickness of 1 nm. These values were taken from Gascoyne[99]. The cell diameter was 20 μm.

For all cases, the chamber width was 4 mm and the chamber height was 100 μm. The simulations used a flow rate resolution of 1 μL/hr. The starting position of the cell was placed 20 μm before the center of the square trap and at a height of 20 μm, which was determined by our software as the equilibrium height of the levitated cells.

3.2 Results

3.2.1 Resistor-on-Chip Experiments

In order to validate our temperature modeling of cell health, we wanted to match our modeling predictions to measured temperature values, caused by DEP-induced media heating inside a closed flow chamber. Since thermocouples are incredibly large in relation to a DEP trap, they can only measure the average temperature across a large area of the chip. In addition, it would be difficult to use a thermocouple while still keeping the flow chamber completely sealed. Therefore, in order to obtain a more precise measurement of the temperature near the nDEP trap and make the measurement process easier, we used a resistor-on-chip (ROC) to measure media heating.

The ROC was placed between eight rows of twenty-four nDEP square traps (Figure 3-1B). Since electrical resistance is a function of the resistor temperature, we can use the resistance value to determine temperature at the microscale level of the DEP trap. However, we must first calibrate the ROC to determine what the resistance values are at known temperatures. We measured the temperature between 30-60 °C, in five degree increments, and recorded the ROC resistance, allowing us to generate a resistance vs. temperature curve (Figure 3-3A).

Once we calibrated the ROC, we could now investigate the amount of media heating occurring in our DEP traps. We turned on the DEP traps, using an applied signal between 0-5.5 V_p, and recorded the corresponding ROC resistance. Then, using the resistance versus temperature calibration curve, we converted our resistance measurements to temperature values. This enabled us to create a temperature versus voltage curve, which we can then compared to our modeling predictions (Figure 3-3B). We see that at lower voltages, the modeling predictions are within a few degrees of the experimental measurements, while at higher voltages, the model begins to overpredict the measured temperature. The model temperature increase is proportional to V^2, however at higher voltages, the experimental measurements increase at a slower rate than this. This could be due to convection, from either unintentional flows within the chamber, or from electrohydrodynamic (EHD) flows, caused by a temperature gradient existing in the conductive media. However, from the results of our cell health modeling (Figure 3-4), we see that our voltages are limited to below 1.5 V_p, where the model and experimental results match within a few degrees.

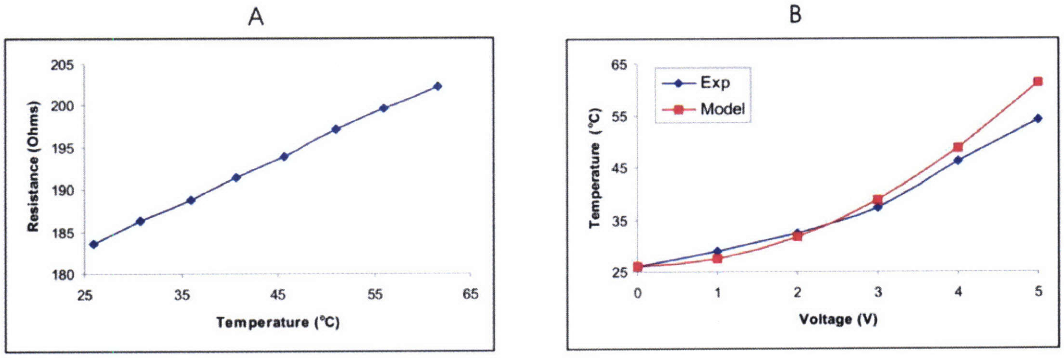

Figure 3-3: ROC experiments. (A) ROC calibration, resistance versus temperature measurements. (B) Media heating experimental measurements and modeling predictions, temperature versus voltage curve.

3.2.2 Cell Health Modeling

While a cell's transmembrane voltage can be measured directly through patch-clamp techniques[100], some groups have measured it indirectly using specialized dyes and sensitive optical techniques[101-104]. However, both of these types of techniques are cumbersome and require single-cell measurements of transmembrane voltage. For our traps, we have relied on a commonly-used model of transmembrane voltage[98], allowing us to predict the induced transmembrane voltages in the DEP Microwells (Figure 3-4A).

In term's of predicting the cell temperature, we could also use specialized dyes to indirectly measure the temperature inside the cell[105], however these methods suffer from the same disadvantages described above. Instead, we chose to indirectly measure the temperature of the cell by measuring the temperature of the media near the cell, bypassing the need to interrogate individual cells. The ROC experiments allowed us to validate our temperature model, which we then used to determine the effects of media heating in the DEP Microwells (Figure 3-4B).

In operating our DEP Microwells, we chose to limit the induced transmembrane voltage to below 70 mV, since previous experimental studies[106,107] indicated that transmembrane voltages under 200 mV did not adversely affect cell physiology, and the cell media temperature to below 38 °C, which is the approximate maximum daily variation in body temperature[108]. According to our modeling predictions, for an applied signal frequency of 10 MHz, we must keep the applied voltage under 1.5 V_p to satisfy both of these requirements. In our case, media heating is the limiting factor that restricts our operating voltage; however this is not always the case in DEP trapping. When using pDEP, requiring the cells to be immersed in a low-conductivity media, media heating is rarely an issue, since the temperature rise is directly proportional to the media conductivity (Eq. 3-1). Also, when using a substrate with a higher thermal conductivity, such as Si, media heating is reduced significantly. In addition, we chose an operating frequency of 10 MHz to minimize the induced transmembrane voltage, while still maximizing trap strength[57].

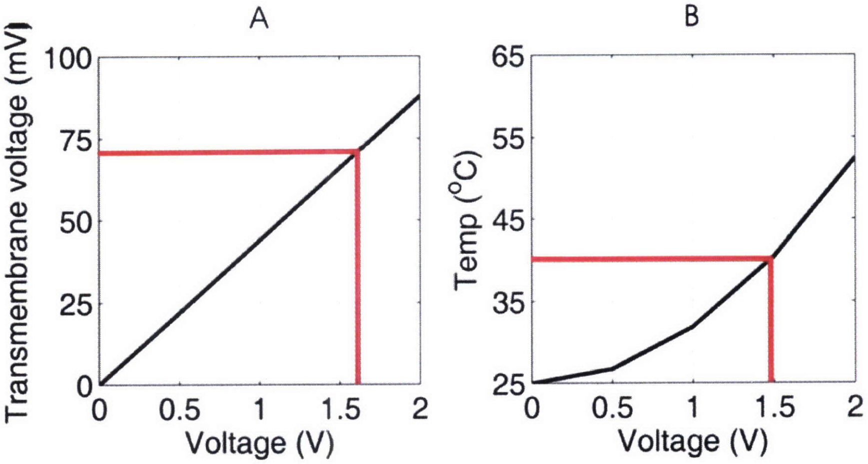

Figure 3-4: Cell health modeling. (A) Induced transmembrane potential and (B) media temperature as a function of the applied signal voltage in the DEP Microwell. The applied signal frequency was f = 10MHz.

3.2.3 Initial Cell Trapping Experiments

Now that we have modeled the effects of DEP trapping on cell health, we can use these restrictions on the signal voltage to safely operate our DEP traps. Keeping the signal voltage below 1.5 V_p, we used our DEP trapping protocol (Figure 2-2) to attempt trapping of 3T3 murine fibroblasts.

While we were able to successfully load single 3T3 fibroblast cells into the nDEP square traps and keep them trapped there against flow, cells were also getting stuck to the bottom substrate in areas outside of the square traps, thus ruining the overall cell pattern (Figure 3-5A). This cell sticking occurred as soon as cells were flowed into the chamber, happening immediately upon making contact with the bottom substrate. These cell-substrate interactions were so large that the cells could not be removed, even with flow rates as high as 100 μL/min. Unfortunately, we were not able to solve this problem by modifying the substrate, making it non-adherent to cells, because we want the cells to eventually attach and proliferate (Figure 1-3).

3.2.4 The DEP Microwell

Since we could not prevent cells from sticking to the bottom substrate using chemical methods, we decided to use a DEP approach. We added interdigitated electrodes (IDEs) between the square traps, creating a *z*-directed DEP force that levitates the cells, thus preventing cells from ever contacting the bottom substrate and sticking (Figure 3-2). Using this design, cells directly over the square traps can still fall down and attach to the bottom substrate (Figure 3-2B). This second generation nDEP square trap prevented almost all the cells from sticking to the substrate (< 5 cells across the entire 10×10 array), allowing us to successfully pattern single mESCs (Figure 3-5B). Using this design, we have also been able to pattern other cell types, such as HeLa cells. Overall, cell patterning efficiencies were consistently between 60-70% across the entire array.

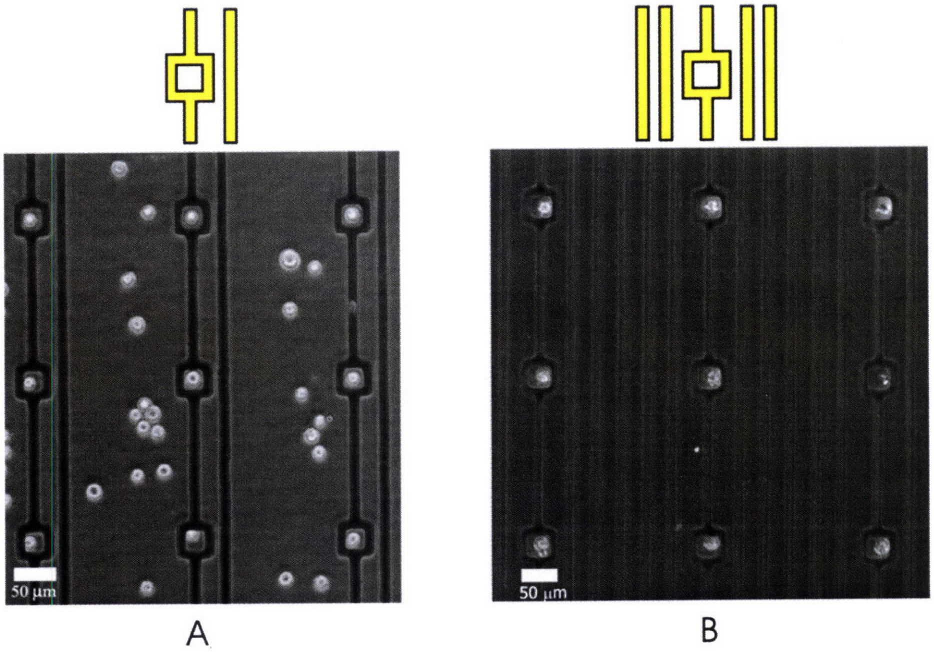

Figure 3-5: Our nDEP square trap. (A) The original design, which allowed cells to stick to the substrate. (B) The improved design with IDEs outside the traps, the DEP Microwell, preventing cells from sticking to the substrate.

3.2.5 Cell Loading Experiments

While we have validated our modeling software many times with beads[45,61,67], we have validated it only once with cells[76]. Since our nDEP square traps operated very differently than the extruded quadrupole posts, we preferred to validate the modeling predictions again using cells in our traps. However, unlike the extruded quadrupole posts that trap cells levitated above the substrate, and beads in our square traps that are immersed in a surfactant to prevent substrate adhesion, cells in our traps do indeed stick to the substrate once trapped (Figure 3-5A). This prevents us from making maximum flow rate measurements of already-trapped cells, since they are stuck to the bottom glass and cannot be removed with practical flow rates. Furthermore, since the magnitude of these cell-substrate adhesion forces is not currently known, we cannot incorporate them into our modeling software. Therefore, in order to still validate our modeling software for cell trapping in the DEP Microwells, we performed cell loading experiments – measuring the flow rate that a cell can flow into a square trap, without being washed away. We defined this maximum loading flow rate, at a given applied voltage, as the flow rate at which nine out of ten cells are able to successfully load into the DEP Microwell.

For mESCs, we measured the maximum loading flow rate at a voltage of 0.25, 0.5, 0.75, 1.0, or 1.25 V_p, allowing us to generate the loading characteristic for the trap (Figure 3-6, top). These voltages are all under the restricted voltage of 1.5 V_p, to ensure safe operation for cell health. First, we see that the modeling predictions and the experimental measurements match well, thus validating our modeling software for use with cells in these traps. Second, we notice that the maximum flow rate increases as a function of voltage, and then decreases, creating a peak loading flow rate. This behavior is completely unexpected, but was elucidated using the modeling software.

Since in our traps, the *z*-directed stability determines the trap strength, we can look at the stability transition line to try and understand the peak behavior (Figure 2-8B). In Figure 2-8B, the stability transition line was plotted for only about half of the inner square trap area. Here, we plotted the stability transition behavior for a much larger area, reaching far outside the DEP Microwell, allowing us to observe the symmetry of the stability transition area on both halves of the square trap (Figure 3-6A-C). In addition, in order to make these stability plots easier to read, we colored in the areas of upwards *z*-directed DEP force in blue and the areas of downwards *z*-directed DEP force in white. The white areas then indicate where it is possible for the cell to fall in and load into the trap.

These stability plots are able to help explain the peak loading behavior. For low voltages, the cells are able to fall into the trap, yet the streamlines show the cell breaking through the trap and flowing away, indicating that *x*-directed DEP forces are too weak to hold the cells in the trap at higher flow rates (Figure 3-6A). For the peak voltage of 0.75 V_p, the cells are still able to fall into the trap, but now the *x*-directed DEP forces are strong enough to hold cells at 4× higher flow rates (Figure 3-6B). At even higher voltages, the region of upwards *z*-directed DEP force is much larger, taking up most of the DEP Microwell (Figure 3-6C). At higher flow rates, the particle streamlines show the cells passing over the trap, not being allowed to fall down into the trap where the *x*-directed DEP forces are strong enough to resist these higher fluid flows.

Without our predictive modeling software, we would not have been able to explain this phenomenon behind the peak loading behavior. However, because we could quantify all the forces in our microsystem and use the streamlines to visualize the cell trajectories, we were able to determine exactly how the cells behave in our DEP Microwells.

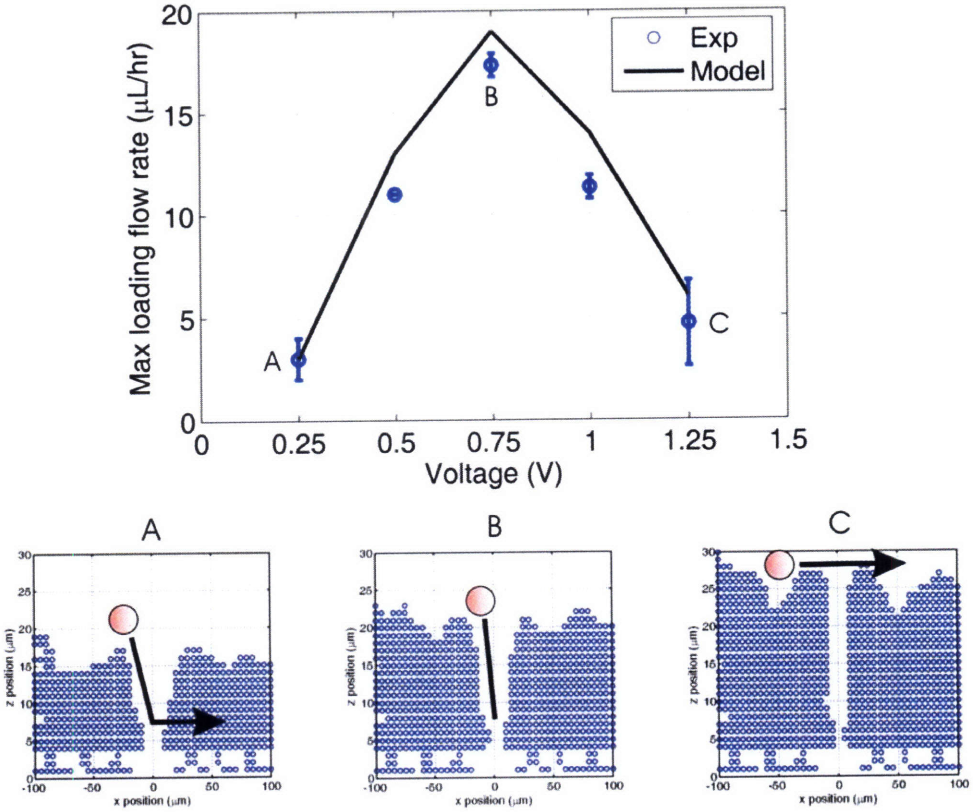

Figure 3-6: Cell loading experiments and modeling – maximum loading flow rate as a function of the applied signal voltage. Bars on experimental data indicate 1 standard deviation from the mean. (A) At low voltage, the cell can fall into the DEP Microwell but the *x*-directed force is too weak to hold the cell against higher flows. (B) At the peak voltage, the cell can fall into the DEP Microwell and the *x*-directed force is strong enough to hold against higher flow. (C) At higher voltages, the cell can not fall into the DEP Microwell and passes over the trap.

3.3 Discussion

3.3.1 Future Improvements for the DEP Microwells

While the IDEs worked well to prevent most cells from sticking to the substrate, there were still a few cells that managed to fall down and stick to the glass slide. These cells were stuck in areas where the IDE spacing was largest, greater than 15 μm, suggesting that there were some vulnerable spots in the levitation field. In order to minimize these cell-substrate interactions, we recommend an IDE spacing of ≤ 10 μm for future generations of the DEP Microwell. In addition, many cells stuck to the substrate in areas outside the IDE array (Figure 3-7). To prevent this in the future, the IDE arrays could be expanded further so that they cover the entire surface inside the flow chamber. However, note that increasing the IDE array size will also increase media heating within the flow chamber. Therefore, in order to safely operate the traps to maintain cell health, the maximum applied voltage will need to be even less.

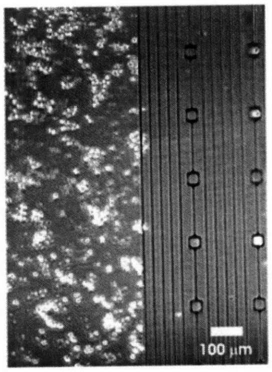

Figure 3-7: Cells sticking to the substrate in the areas outside the IDE arrays. To prevent this, the IDE arrays can be expanded further so that they cover the entire surface inside the flow chamber.

3.3.2 Cell Proliferation and Movement in the DEP Microwells

In order to demonstrate that the operating protocols for the DEP Microwells are indeed safe, we observed the trapped cells over multiple days. I trained Nick Mittal on how to use the DEP Microwells with various cell types. Using my DEP chips, he was then able to trap HeLa cells in the DEP Microwells, successfully enabling proliferation and movement, which he tracked for four days (Figure 3-8A-D). We see that by day 1, the cells are beginning to grow and move, while by day 4, the cells are already partially confluent – suggesting that the DEP trapping is not grossly affecting cell health. Nick Mittal is continuing to use these DEP Microwells to pattern multiple cell types on the same substrate, attempting to reconstruct various stem cell niches.

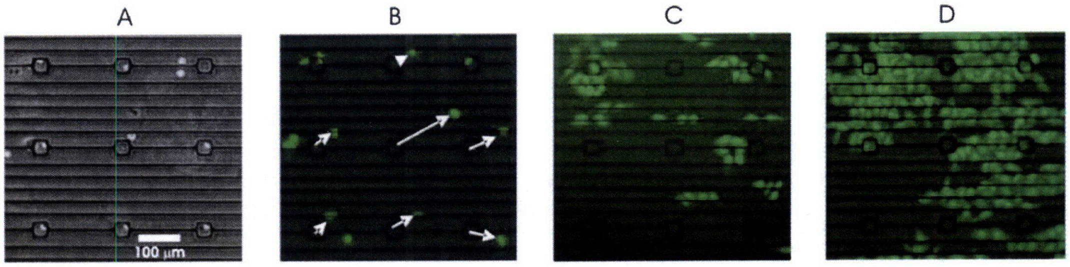

Figure 3-8: Cell proliferation and movement in the DEP Microwells. Trapped HeLa cells on: (A) day 0, (B) day 1, (C) day 2, and (D) day 4.

3.3.3 Challenges Using DEP for Cell Patterning

One of the main challenges we encountered when increasing the size of the DEP trap array was cell-cell interactions – the cells immediately stuck to each other upon contact. This problem was manageable with our smaller 10×10 arrays, but became difficult to solve when we scaled up to larger 10×48 arrays. With all DEP Microwell array sizes, we are able to initially fill ~90% of the traps with single cells. However, pattern efficiency and fidelity significantly decrease when flowing away the high numbers of untrapped cells. The cells start to stick to each other, causing flowing cells to either: stick to cells in the traps and pull them out, stick to cells in the traps and get pulled into the trap so that multiple cells are held in one trap site, or stick to each other outside the traps and cause very large cell clumps that cannot be removed with practical flow rates (Figure 3-9).

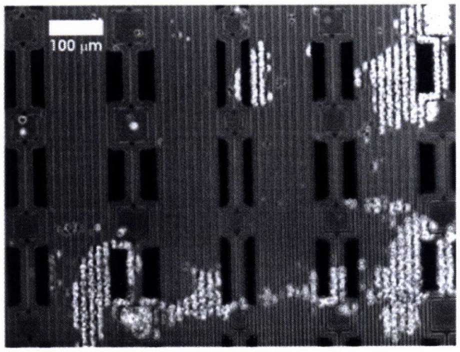

Figure 3-9: For larger trap arrays, cell-cell sticking is a significant issue, causing large cell clumps on the trap array that cannot be removed.

We tried to reduce this cell-cell clumping by immersing the cells in either PBS or cell-dissociation buffer (Invitrogen, 13151-014), in order to reduce cell stickiness, but neither was sufficient enough to improve pattern fidelity. Future generations of the DEP Microwells might be able to minimize this cell clumping by levitating the cells even higher, so that they are not able to interact with the cells that are already held in the traps. Another approach could be to reduce the cell solution density, so that fewer total cells are present across the DEP trap array. However, in order to maintain the high number of cells loaded into the traps, we would need to be able to actively direct these fewer cells into the traps, possibly by using a DEP funnel[93].

Overall, in addition to the problems with scalability, there are still disadvantages of using DEP as a cell patterning technique. The substrate for cell patterning is somewhat restricted because we need to pattern the DEP electrodes on glass or silicon. Since many cells behave differently on various substrates, this could prevent us from using certain cell types with DEP patterning. In addition, there is still the possibility that the electric fields are affecting cell health and/or cell physiology. Even though we used our modeling software to determine safe operating voltages, and demonstrated HeLa proliferation and movement after DEP trapping, the electric fields could still be affecting cellular physiology in other ways. These effects are even more of a concern when using DEP with more sensitive cell types, such as ESCs, since these effects could affect self-renewal and differentiation. Therefore, due to these additional challenges associated with DEP cell patterning, we decided to explore alternative cell patterning techniques that may be more suitable for use with ESCs.

Chapter 4: The Bio Flip Chip

Since cell patterning with our DEP traps had certain limitations, such as difficulty patterning large numbers of cells and possible effects on cell health, we decided to explore other approaches to patterning mESCs. Thus, we created the Bio Flip Chip (BFC). In this chapter, we demonstrate the numerous capabilities of the BFC, such as patterning large numbers of cells, with single-cell resolution, while allowing the cells room to grow and move. The BFC is also the only cell patterning technology that can pattern cells onto any substrate. Finally, the BFC is gentle on the cells, while remaining very simple to use.

4.1 Materials and Methods

4.1.1 Fabrication of the Bio Flip Chip

We made the BFCs by molding polydimethylsiloxane (PDMS) over a 4" Si master wafer. We dehydrated the Si wafers for 30 min at 130 °C. SU8-2050 (Microchem) was poured onto the wafer, ramped at 300 rpm/s to 3000-4000 rpm, and spun for 30 s to yield feature heights of 40-30 μm, respectively. After spinning, we placed the wafer on a 65 °C hotplate, immediately ramped up the temperature to 95 °C for 5-6 min, and then ramped it down to 65 °C. We exposed the wafers to a UV dose of 200 mJ/cm^2 on a contact aligner (Karl Suss, MJB-3 Mask Aligner) using a dark-field mask printed at 20,000 dpi (CAD/Art Services). We placed the wafers on a 65 °C hotplate, immediately ramped up the temperature to 95 °C for 4-5 min, and then ramped it down to 65 °C. Next, we immersed the wafers in PM acetate (Doe and Ingalls) and Isopropanol while we spun them at 500 rpm for 3 min. Actual heights of the SU8 features were measured with a profilometer (Sloan, Dektak II).

We then silanized the wafers for 30 min using hexamethyldisiloxane (Shin-Etsu MicroSi) to prevent PDMS from adhering to the Si master wafer. We mixed PDMS (Dow Corning, Sylgard 184) in a 10:1 ratio, poured it over the master Si wafer (~10 g per wafer), and let it cure overnight at room temperature. The cured PDMS was then slowly peeled off the Si wafer and each chip was cut out using a razor blade and bonded to a 1" × 1" cut microscope slide for easy handling (Figure 4-1B-C).

4.1.2 Bio Flip Chip Operation

We soaked the BFC overnight in PBS in order to prevent absorption of media into the PDMS during the experiment (see Section 4.2.1: Initial Challenges with BFC Patterning). After soaking, we sprayed the chips with ethanol and dried them with a Kimwipe (Kimtech Science). In the tissue-culture hood, we coated the BFC surface with 200 μL of 7.5% Bovine Serum Albumin (BSA) (Invitrogen, 15260-037) and scraped it with a pipette tip to disperse the BSA and remove any bubbles from the wells. The BSA helped to prevent cells from sticking in the microwells after flipping. We left the BSA on the BFC surface for ~1 hr and agitated with a pipette tip every 20 min to prevent crusting.

To fit the BFC inside a 35×10 mm TCPS dish (Falcon, 35-3001), we cut the rims of the TCPS dish half way down so that the ¾" binder clips (Office Depot) would fit over the dish rim to clamp the chip and dish together (Figure 4-1A). We cut the PDMS spacer gasket (frame-shaped with 20×20 mm outer edge, 15×15 mm inner edge, and 250 μm thickness) from a PDMS sheet (Silicone Specialty Products) and then applied it to the dish using tweezers. This spacer gasket was required in order to provide the cells with enough media to prevent nutrient depletion (see Section 4.2.1: Initial Challenges with BFC Patterning). We were able to pattern cells with a range of gasket thicknesses, from 100-600 μm, without any significant differences in cell patterning precision.

We sterilized the dish, gasket, BSA-coated chip, and 2 binder clips under UV light for 1 hr. Afterward, we aspirated the BSA and rinsed the BFC with 200 μL PBS. After aspirating the PBS, we applied 200 μL of cell solution ($\sim 1\times10^6$ cells/mL) to the BFC surface. We let the cells settle for 5-10 min (Figure 4-1D). To clear away the cells outside the microwells, we tilted the BFC to one corner at a 15° angle and slowly pipetted the cell solution off with a 200 μL pipette. Next, we placed the BFC flat and added 100 μL of PBS or blank media to the opposite BFC corner. We observed the BFC under the microscope to make sure cells were still loaded in the wells and rinsed the BFC an additional 2-4 times if necessary (Figure 4-1E). Initially, we tried clearing away the cells outside the microwells using a cell scraper (Falcon, 35-3085), scraping off the cell-solution on the BFC surface, however this method was too aggressive and also ended up removing the cells inside the microwells.

We added 100 μL of media to both the chip surface and the dish inside the PDMS gasket. We spread the media around to wet the entire dish surface in order to prevent bubbles from forming in the chamber after flipping. We then inverted the pre-wetted dish and slowly pushed up the BFC into the dish. We applied a binder clip to each side and removed the metal prongs so that dish remained level when flipped over. Lastly, we quickly flipped over the setup onto the incubator shelf while avoiding any unnecessary movement (Figure 4-1F).

The cells fell out of the wells within minutes and attached to the dish after a few hours (Figure 4-1G), where the cells now have room to grow and move (Figure 4-1H). The BFC can then be removed or left on the substrate. To remove the chip without disturbing the cells, we reinserted the metal prongs into the binder clips and removed them slowly at equal speeds. We then added 0.75 mL media to the dish, around the BFC, and returned the setup to the incubator. This allows the media to slowly release the BFC from the substrate, preventing disruption of the cell pattern (< 5% of the cells are disturbed). After 4 hrs, the BFC can be carefully removed. We aspirated and replaced the old media with 1.0 mL of fresh media. We then maintained the dishes by feeding daily with 1.0 mL media.

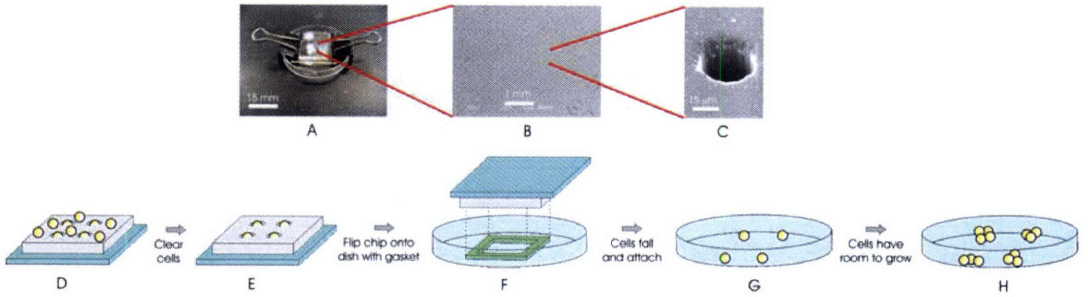

Figure 4-1: BFC device and operation. (A) BFC packaging, consisting of a BFC, spacer gasket, and cell-culture dish, all held together using binder clips. (B) SEM image of the BFC microwells, spaced 200 μm apart. (C) SEM image of a single microwell, with diameter and height of 30 μm. (D) The cells are pipetted onto the surface of the chip, allowing cells to fall into the microwells. (E) The cells are trapped in the microwells and the other cells are rinsed away. (F) The BFC is flipped upside down onto the dish with a spacer gasket. (G) The cells then fall out of the microwells onto the substrate, where they attach after a few hours. (H) The cells now have room to grow and move.

4.1.3 Preparation of the Substrates

To pattern the cells onto the surface with patterned gelatin, the 3-D substrate, and another layer of cells – we used the same protocol described above, with prior modification to the substrate before flipping the BFC. The surface with patterned gelatin was made by placing an elastomeric stencil onto a 60×15 mm TCPS dish (Falcon, 35-3002) and immersing the dish with fluorescent gelatin at 1 μg/mL (Molecular Probes, G13186). We incubated the dish for 15 min at 37 °C and then washed it twice with PBS before removing the stencil. The elastomeric stencils had 100 μm circular holes that formed the pattern (Figure 4-6A). Somponnat Sampattavanich helped with this preparation and provided the patterned gelatin substrates for this experiment.

To create the 3-D substrate, we placed a 100 μm thick layer of PDMS (Silicone Specialty Products) onto half of a 35×10 mm TCPS dish, creating a stepped surface. The cells were then flipped onto the dish, with half of the cells falling directly onto the dish and the other half falling onto the PDMS step (Figure 4-6B).

To create the layer of cells, we seeded murine embryonic fibroblasts (MEFs) at a density of 3×10^6 cells/mL onto a 35×10 mm TCPS dish one day prior to patterning the murine embryonic stem cells. We incubated this dish with MEFs overnight and removed it from the incubator several minutes before flipping. We aspirated the old media from the dish, placed a PDMS gasket on the dish over the MEFs, and added 100 μL of media to the dish inside the gasket. We then inverted the dish with cells and slowly pushed up the BFC into dish, as described above.

4.1.4 Calculating Cell Patterning Efficiency and Precision

To calculate the cell patterning efficiency, a 50×50 grid of cells was patterned onto a 35×10 mm TCPS dish and the entire chip was scanned and imaged at 5× magnification (Zeiss, Axioplan 2 imaging microscope). We then used Matlab-based imaging software to stitch together the individual pictures into one stitched image of the entire chip. From the final stitched image, we calculated the cell patterning efficiency by dividing the number of spots with cells within one well diameter from the well edge, by the total number of available spots ($n = 4$ chips).

To calculate the cell patterning precision, we took pictures of the 50×50 grid of patterned cells across the chip at 10× magnification (Zeiss, Axiovert 200 microscope). From the pictures, we measured the number of pixels between adjacent cells ($n = 211$ measurements over 4 chips). We converted the number of pixels to a distance using a conversion factor, determined using a cell-counting chamber with a known grid spacing (VWR, 15170-208).

4.1.5 Cell Culture

We cultured ABJ1 mESCs with a stably integrated GFP reporter for Oct-4 without feeders in mESC media: DMEM (Invitrogen, 11960-044) supplemented with 15% ES-qualified fetal bovine serum (Invitrogen, 16141-079), 4 mM L-glutamine (Invitrogen, 25030-081), 1 mM non-essential amino acids (Invitrogen, 11140-050), 50 U/mL penicillin, 50 μg/mL streptomycin (Invitrogen, 15140-122), 100 μM β-mercaptoethanol (Sigma-Aldrich, M7522), and 500 pM leukemia inhibitory factor (Chemicon, ESGRO ESG1107). We cultured cells directly on 100×20 mm TCPS dishes (Nunc, 172958) in a 37 °C humidified environment with 7.5% CO_2. For maintenance of mESCs, we fed cells daily and passaged every other day using 0.25% trypsin- EDTA (Invitrogen, 25200-056) at a density of 5×10^5 cells/cm^2. The mESC passage number was always below P30. To demonstrate large-scale cell patterning, we stained the mESCs with a live green-fluorescent stain (Molecular Probes, Calcein AM).

We cultured the murine embryonic fibroblasts (MEFs) in media identical to mESC media, except without the leukemia inhibitory factor and β-mercaptoethanol. The MEFs were thawed, previously being mitotically inactivated with mitomycin C (Sigma-Aldrich, M4287), and seeded at a density of $\sim3\times10^6$ cells/mL. The MEF passage number was P5.

4.2 Results

I trained and supervised two undergraduate students in this BFC research, Alice Macdonald and Steph Flavin. Alice Macdonald was pivotal in demonstrating the BFC proof-of concept, helping to show effective patterning with mESCs. She took several of the pictures in this chapter, such as Figures 4-2, 4-4, 4-5, 4-7, and 4-8. Steph Flavin helped to demonstrate patterning cells onto any substrate and took the pictures in Figure 4-6.

4.2.1 Initial Challenges with BFC Patterning

When we initially came up with the concept of the BFC, we envisioned flipping the BFC directly onto the desired substrate, without a spacer gasket between the two surfaces. Our initial trials showed that, without the gasket, the cells in the BFC microwells (Figure 4-2A) died within a few hours after flipping, rupturing the cell membrane and causing the cells to spill out their inner contents (Figure 4-2B). We hypothesized that the cause of cell death was due to a lack of nutrients, since there was only a small amount of media available to each cell in its corresponding microwell. Since the 30 μm-diameter, 30 μm-height microwell has a volume of 21 pL and a single 20 μm-diameter mESC has a volume of ~4 pL, this leaves only ~17 pL of media in the microwell with the cell.

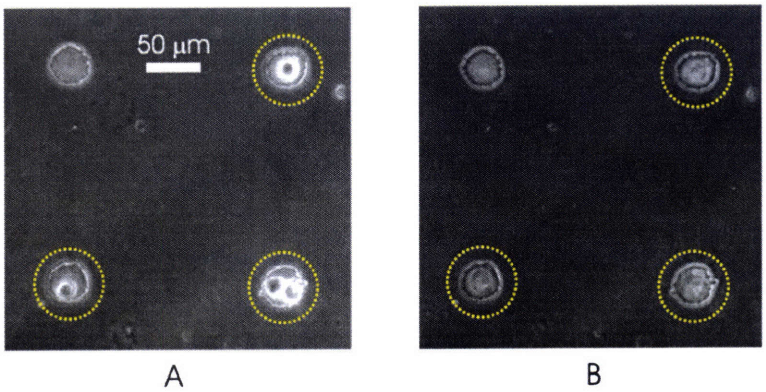

Figure 4-2: Using the BFC without a spacer gasket causes cells to die. (A) Cells in three of the four microwells (shown in yellow circles) immediately after flipping the BFC directly onto the cell-culture dish. (B) The same set of microwells, showing the cells dying after a few hours. Images were taken from the initial and final frames of a video sequence.

By placing a spacer gasket between the BFC and the substrate, we simultaneously exposed all the cells in the microwells to a much larger volume of media, ~22.5 µL. This provided the cells with enough nutrients to thrive for several days. Even keeping the BFC clamped to the substrate for five days, without feeding the cells, they were able to grow into large, spherical colonies, representing normal mESC colony morphology (Figure 4-3).

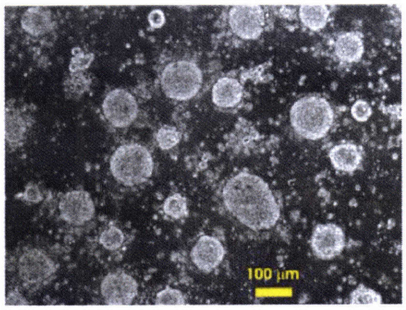

Figure 4-3: Cells proliferating in the BFC environment. mESC colonies after five days in the BFC, without being fed, and still showing a normal morphology.

After solving the nutrient issues, the next challenge we encountered involved preventing the cells from getting stuck in the microwells. After flipping the BFC, only about half of the cells were falling out of the wells onto the substrate, while the rest remained stuck in the microwells (Figure 4-4). Our initial approach to solve this worked well – pre-coating the BFCs with Bovine Serum Albumin (BSA). BSA is a serum albumin protein that is commonly used in cell-culture to prevent cell-substrate adhesion. Coating the BFCs for one hour before depositing the cell solution remarkably helped to reduce the number of cells sticking in the microwells (< 1% remained stuck). We hypothesized that continuous absorption of media into the PDMS microwells also increased the chance of cells sticking in the wells. Therefore, in order to saturate the PDMS chip absorption capability; we soaked the BFCs overnight in PBS, which also helped to decrease sticking. After overcoming the initial challenges with BFC patterning, we were then able to demonstrate effective patterning.

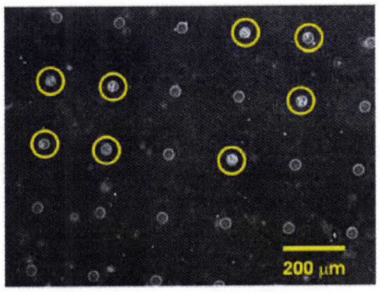

Figure 4-4: Cells sticking in the microwells. After flipping the BFC (without coating the BFC surface with BSA), about half of the cells fell out onto the substrate, while the other remained stuck in the microwells (shown with yellow circles).

4.2.2 Large-Scale and Precise Cell Patterning

Scalability, efficiency, and precision are important capabilities of any new approach to cell patterning. We demonstrated the scalability of BFCs by creating large-scale (50×50) cell patterns of murine embryonic stem cells (mESCs) onto a tissue-culture polystyrene (TCPS) dish (Figure 4-5A). We consistently achieved high cell patterning efficiencies, with an overall efficiency of 75.9% (*n* = 4 chips), calculated by dividing the number of spots with cells within one well diameter from the well edge, by the total number of available spots. In addition, we have achieved stem cell patterning with extremely high precision (Figure 4-5B, inset). Using a microwell-to-microwell spacing of 200 μm, we can pattern the cells onto a TCPS dish with a cell-cell spacing of 195 ± 18 μm (*n* = 211 measurements over 4 chips), thus seeding a cell within one cell diameter away from its target location (Figure 4-5B). We have further demonstrated cell patterning down to single-cell resolution, with 50% of the patterned spots resulting in single cells (*n* = 4 chips).

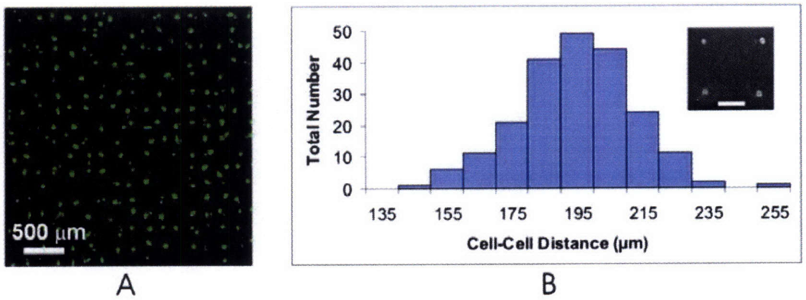

Figure 4-5: Large-scale and precise cell patterning. (A) Patterning of mESCs in a 50×50 grid, stained with a live green-fluorescent stain on day 1 after seeding. (B) Histogram showing the distribution of cell-cell distances, with mean spacing of 195 ± 18 μm. Inset: high precision patterning, seeding cells within 1 cell diameter of their target. Inset scale bar, 100 μm.

4.2.3 Cell Patterning onto Any Substrate

Cell behavior can vary significantly depending on the substrate that the cells are seeded on (e.g., glass vs. TCPS). Since ESCs are very sensitive to cell-substrate interactions[109], we wanted to be able to pattern them onto TCPS, their standard *in vitro* substrate. Most existing cell patterning tools require modification of the substrate – adhesive patterning (e.g., μCP) requires patterning different ECMs[29,41] while techniques that use electromagnetic fields require metal electrodes to be deposited onto glass[57] or silicon[62]. Because the process of patterning with BFCs intrinsically transfers the patterned cells onto another substrate, substrate modification is avoided, allowing patterning of mESCs onto TCPS (Figure 4-5A).

We also patterned cells onto a TCPS dish patterned with gelatin (Figure 4-6A), showing the compatibility of BFCs with cell patterning techniques that do modify the substrate. One can even use BFCs to pattern over 3-D topography, which we demonstrated by patterning mESCs onto a stepped surface (Figure 4-6B). Lastly, because most cell patterning techniques trap and pattern cells with the same substrate, they are incapable of patterning cells on top of an already-existing layer of cells, limiting their utility to one cell layer. However, patterning onto another layer of cells is possible using BFCs, which we demonstrated by patterning mESCs on top of a layer of murine embryonic fibroblasts (Figure 4-6C-D). We can thus use BFCs to pattern onto any substrate – including different materials (e.g., glass, polystyrene), different chemistries (e.g., fibronectin, gelatin, matrigel), different topographies, or different cells.

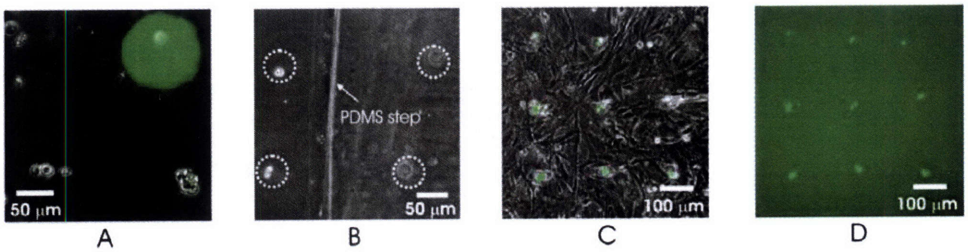

Figure 4-6: Patterning onto any substrate. (A) Cell patterning of mESCs onto a TCPS dish with patterned fluorescent gelatin (top right), showing the compatibility of these two approaches. (B) Cell patterning of half the cells onto a TCPS dish (left, in-focus) and half the cells on a 100 μm step of polydimethylsiloxane (PDMS) (right, out-of-focus). (C) Cell patterning of mESCs onto a layer of murine embryonic fibroblasts. (D) Fluorescent picture of (C), showing only the mESCs.

4.2.4 Multi-Day Cell Tracking: Proliferation and Migration

One of our goals in developing BFCs was to allow patterned cells to proliferate and migrate. mESCs, for instance, divide rapidly (~14 hour doubling time[19]) and the resulting colonies also migrate. In order to study these phenomena, tracking cell growth and movement over multiple days, one needs a technique that patterns cells onto an unconfined area. Currently, there are several existing cell patterning techniques that are suitable for cell tracking over timescales where proliferation or migration is not significant (usually < 24 hours). However, these techniques trap the cells in a confined area, such as an extracellular matrix island[29] or a microwell[37,38]. Using BFCs, however, we can pattern cells onto substrates that are entirely unconfined, enabling both proliferation and migration.

In addition, since each cell has a unique coordinate within the patterned grid, it is possible to track the resulting cells or colonies if desired. In Figure 4-7 we show tracking of one area of patterned mESCs over two days. By day 2, almost all of the initially patterned cells have proliferated into mESC colonies, suggesting that our technique is gentle on the cells and not grossly affecting cell health. The fast doubling time of mESCs causes some deterioration of the pattern by day 2 (Figure 4-7C), which is strong evidence that the cells can indeed migrate freely and is a key feature of our approach. While this precludes the use of BFCs for creating long-term stationary patterns, we emphasize that *stationary* patterns are exactly what we are trying to avoid.

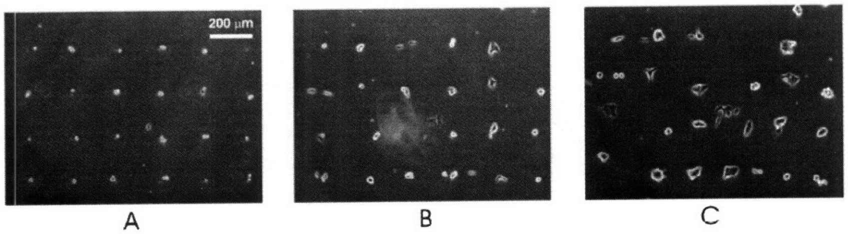

Figure 4-7: Multi-day cell tracking. Proliferation and migration of mESCs on (A) day 0, (B) day 1, and (C) day 2.

4.2.5 Modulating the Cell Seeding Density

Diffusible signaling between cells has been shown to be an important component of the stem cell microenvironment. For instance, stem cell seeding density can affect both differentiation and self-renewal[19,21,22]. However, traditional cell culture techniques control the cell density only at the macroscopic level of the cell-culture dish, creating poor uniformity in cell density and resulting in a cellular microenvironment that varies from cell to cell. However, we can use BFCs to pattern the cells into a grid so that every cell experiences a more uniform microenvironment. Additionally, by varying the spacing of the microwells across the chip (Figure 4-8A), we can pattern cells at multiple seeding densities on the same substrate. We demonstrated this functionality by patterning mESCs on a 60×15 mm TCPS dish at three seeding densities – with a cell-cell spacing of 200, 400, and 800 μm (Figure 4-8B-D).

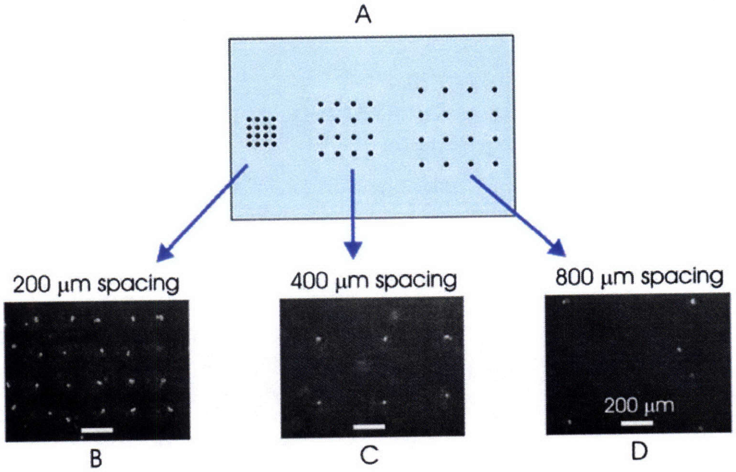

Figure 4-8: Modulating the cell seeding density. (A) By varying the well-well spacing across the chip, we can pattern cells at multiple seeding densities on the same 60×15 mm TCPS dish. Cell patterning with cell-cell spacing of: (B) 200 μm, (C) 400 μm, and (D) 800 μm.

4.3 Discussion

The BFC, in principle, should be able to be used with any cell type. We measured the unattached mESC diameter as 20 ± 3 μm (n = 30) and therefore tried a range of microwell diameters (30, 35, and 40 μm) and heights (30, 40, and 50 μm) to optimize single single-cell trapping. The optimal well diameter and height was 30 μm. To use the BFC to pattern single cells of another cell type, we recommend using a microwell diameter and height equal to 10 μm greater than the unattached cell diameter. In general, a well diameter-to-height ratio of one maximized single-cell patterning efficiency. When the ratio was >1, the wells were too shallow and the cells were washed out of the wells during clearing, reducing overall efficiency. When the ratio was <1, the wells were too deep, and multiple cells were trapped in each well.

Our results demonstrate the key advantages of this new technology and suggest additional applications. First, the ability to pattern single motile cells (Figure 4-7A-C) enables patterned chemotaxis assays. These are currently performed using switchable substrates[110], which trade off substrate chemistry requirements and ease of use for temporal control of motility. Second, BFCs can be used to pattern cells onto other cells (Figure 4-6C). Many cell types or *in vitro* assays require support cells; including maintaining hESCs on feeders[111], differentiating stem cells in the presence of stroma[112], or co-culture of primary cells with non-parenchymal cells[113]. μCP is the predominant approach for patterning such interactions, but is limited to side-by-side patterning where the second cell type fills the interstitial spaces of the first patterned cell type. This is a general feature of cell patterning methods that trap and pattern cells with the same substrate, whereas the BFC technique is completely substrate-independent. This substrate independence is what allows us to pattern one cell type *onto* another cell type.

A key factor for the impact of various patterning technologies is their ease-of-use and transferability. Many existing patterning technologies are either difficult to fabricate or use[40-46], a barrier that prevents their wide adoption. Indeed, the most common cell patterning technique is μCP[29,39], which is simple enough to be used by those with moderate skill in a typical biological laboratory. BFCs are poised to have similar adoptability, since they require no external equipment or chemicals. Using BFCs is complementary and orthogonal to use of μCP (Figure 4-6A); μCP provides higher patterning efficiencies and a greater range of pattern shapes, while the BFCs provide substrate-independence with no restrictions on motility or proliferation.

Lastly, in comparing the BFC to our DEP traps, both have patterned cells with high efficiencies and single-cell resolution. However, the BFC has proven to be a much more effective tool for patterning large numbers of mESCs. The main difference in trapping between these two technologies is that the DEP traps position the cells such that they are still vulnerable to interacting with the cells being washed away, causing cells to clump inside and outside the traps (see Section 3.3.3: Challenges Using DEP for Cell Patterning). The BFCs on the other hand, traps the cells in microwells, protecting them from the cells that are being washed away. In addition, since the BFC uses a physical microwell to hold the cells in place, the traps are incredibly resistant to high-velocity flows. The DEP traps, however, are only as strong as the DEP force which, even in a strong DEP trap, is limited in order to minimize effects on cell health. Furthermore, the BFC technology has the additional advantages of being able to pattern cells onto any substrate, being gentler on the cells, and extremely easy to use.

Chapter 5: Using the BFC to Control mESC Signaling

Now that we have demonstrated the numerous capabilities of the BFC, we will use it to answer the interesting biological question: why do mESCs prefer to be seeded as single cells? In this chapter, we used the BFC to pattern small groups of cells, with and without cell-cell contact, allowing incremental and independent control of contact-mediated signaling. We present quantitative evidence that cell-cell contact plays an important role in depressing mESC colony formation, and show that E-cadherin is involved in this negative regulatory pathway.

5.1 Materials and Methods

5.1.1 Controlling Starting Cell Number

The BFC technology has several parameters that can be modulated – such as microwell diameter and height, microwell-to-microwell spacing, and array size – allowing a wide range of cell patterning configurations. By making the well dimensions large enough to trap multiple cells, we can vary the number of cells patterned at each spot. Using a BFC with 0.75 mm microwell-to-microwell spacing, well diameter of 40 μm, and well height of 50 μm (Figure 5-1A), we patterned small clusters of 1-4 mESCs (Figure 5-1B), allowing them to experience cell-cell contact (Figure 5-1C).

To selectively turn off cell-cell contact, we used small groups of single-cell sized microwells. Using a BFC with 0.75 mm microwell-to-microwell spacing, well diameter of 30 μm, and well height of 30 μm (Figure 5-1D), we patterned small groups of 1-4 single mESCs at each spot (Figure 5-1E), without cell-cell contact (Figure 5-1F). These microwells had an edge-edge distance of ~20 μm ($n = 30$), which generated patterned cells with a membrane-membrane distance of 45 ± 15 μm ($n = 33$).

All of these patterning experiments were performed by leaving the BFC on the cell-culture dish after patterning, forming a closed chamber and therefore minimizing convection of the cell-culture media inside.

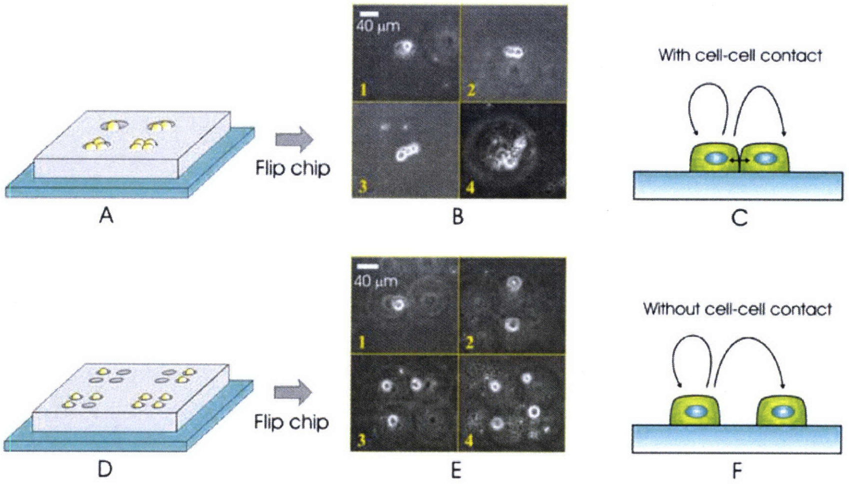

Figure 5-1: Controlling starting cell number. (A) By making the well dimensions large enough to trap multiple cells, we can vary the number of cells patterned at each spot. (B) Using a BFC with 0.75 mm microwell-to-microwell spacing, well diameter of 40 μm, and well height of 50 μm, we patterned clusters of cells with 1-4 cells at each spot. (C) Patterning the cells as clusters allows them to experience cell-cell contact. (D) Using multiple single-cell sized wells, we can pattern small groups of cells without any cell-cell contact. (E) Using a BFC with 0.75 mm microwell-to-microwell spacing, well diameter of 30 μm, and well height of 30 μm, we patterned small groups of 1-4 single mESCs at each spot. (F) Patterning mESCs as small groups of single cells allows us to turn off cell-cell contact.

5.1.2 Cell Culture

We cultured ABJ1, D3, and CCE mESCs without feeders in mESC media, as described in Section 4.1.5: Cell Culture. We cultured cells directly on 100×20 mm TCPS dishes (Nunc, 172958) in a 37 °C humidified environment with 7.5% CO_2. For maintenance of mESCs, we fed cells daily and passaged every other day using 0.25% trypsin- EDTA (Invitrogen, 25200-056) at a density of 5×10^5 cells/cm^2. The mESC passage number was always below P30.

5.1.3 mESC Pluripotency Staining

To observe Oct-4, we used ABJ1 mESCs with a stably integrated GFP reporter for Oct-4. To observe Alkaline Phosphatase, we stained the cells with Vector Red Alkaline Phosphatase Substrate Kit 1 (Vector Laboratories, SK-5100), using two drops of all three reagents in 5 mL of 100 mM Tris-HCl, incubated at room temperature for 20 min. Both of these markers were observed on day 4.

5.1.4 Testing the Effects of Anti-E-Cadherin Antibody

We incubated mESCs with 40 μg/mL anti-E-cadherin antibody (clone DECMA-1, Sigma, U3254) in mESC media for 2 hrs; control experiments were run with cells incubated with mESC media for the same length of time.

5.2 Results

5.2.1 Precise Control of the Stem Cell Microenvironment

We patterned cells into variable-sized clusters for three mESC lines – ABJ1 (Figure 5-2A), D3 (Figure 5-2B), and CCE (Figure 5-2C). We found that the single-cell colony-forming efficiency was ~37.5% (Figure 5-2A-C), which is typical for mESCs[25]. Interestingly, as we increase the number of starting cells per cluster, we do not observe a proportional increase in colony-forming efficiency. Assuming there was no signaling between the cells in a group, the probability that at least one of *n* independent cells in a group would form a colony is 1 - (probability that all the cells in a cluster die). As the number of cells increases, the probability that a colony will form approaches 100%. For $n = 4$ cells, this translates into a $1-(1-0.375)^4 = 85\%$ colony-forming efficiency (Figure 5-2A-C, solid yellow bars), whereas we observe a colony forming efficiency of 48 ± 13% with ABJ1s ($n = 5$ chips, 156 total colonies counted) (Figure 5-2A, solid blue bars). All three mESC lines showed similar results, as did repeating the experiments with the ABJ1 cell line – ruling out time, population, or cell line artifacts.

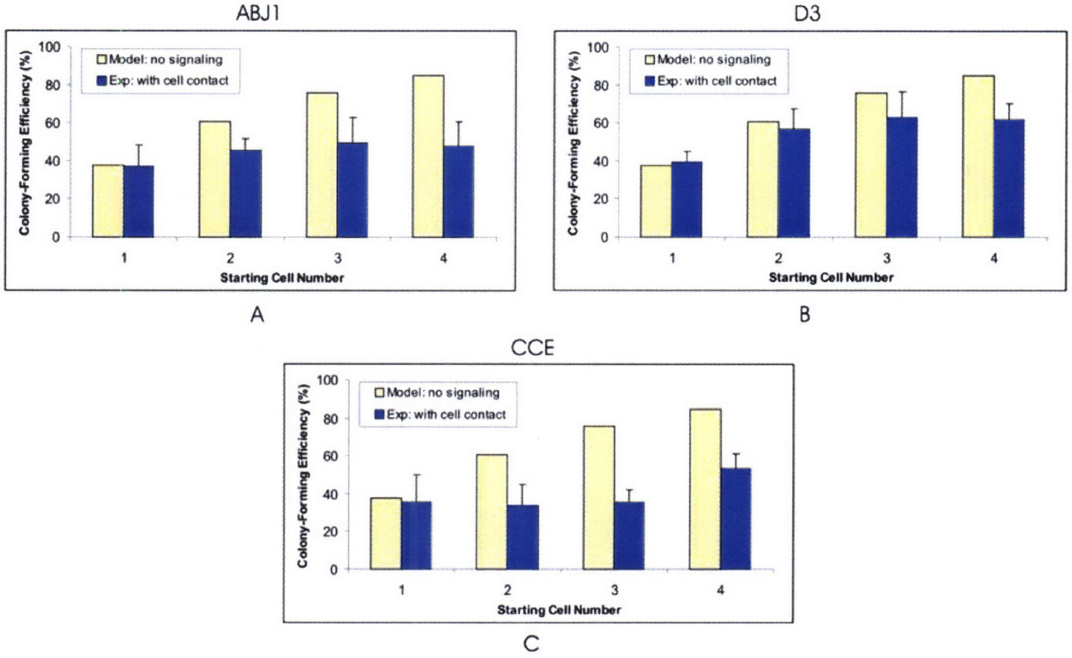

Figure 5-2: Precise control of the mESC microenvironment. Colony-forming efficiency (2 days after cell seeding) as a function of starting cell number for two cases – model of no cell-cell signaling (solid yellow bars) and experiment with cell-cell contact (solid blue bars). Results are for three mESC lines: (A) ABJ1, (B) D3, and (C) CCE. Bars on experimental data indicate 1 standard deviation from the mean.

5.2.2 Removing the Effects of Cell-Cell Contact

In order to investigate the cause of this decreased colony-forming efficiency, we used BFCs with different well configurations to selectively turn off cell-cell contact. We did this for both the ABJ1 mESC line (Figure 5-3A) and the D3 mESC line (Figure 5-3B).

Turning off cell-cell contact, we find that the mESC colony-forming efficiency reverts to that expected for independently acting cells (e.g., no cell-cell signaling) (Figure 5-3A-B, solid red bars), suggesting that cell-cell contact plays a primary role in depressing colony formation.

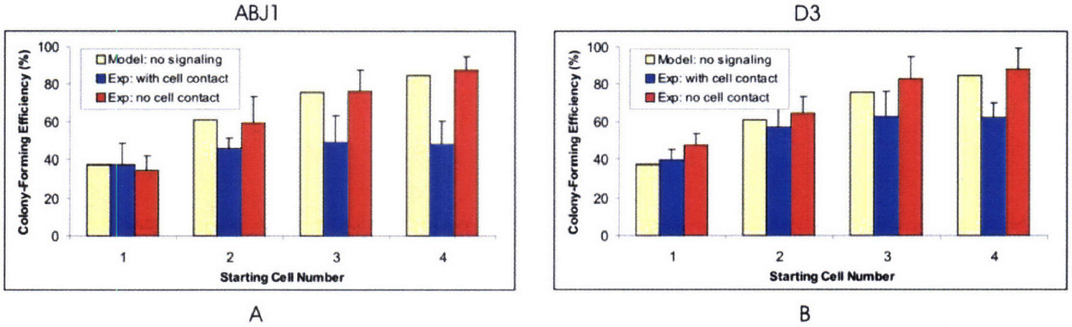

Figure 5-3: Removing the effects of cell-cell contact. Colony-forming efficiency (2 days after cell seeding) as a function of starting cell number for three cases – model of no cell-cell signaling (solid yellow bars), experiment with cell-cell contact (solid blue bars), experiment without cell-cell contact (solid red bars). Results are for two mESC lines: (A) ABJ1 and (B) D3. Bars on experimental data indicate 1 standard deviation from the mean.

5.2.3 Molecular Determinants of Cell Contact-Mediated Depression

To investigate the molecules involved with this cell contact-mediated depression in colony formation, we used a blocking antibody to inhibit E-cadherin signaling. E-cadherin is a transmembrane protein that has been shown to regulate cell-cell adhesion signaling in mESCs[114]. We incubated a single-cell suspension of ABJ1 mESCs in anti-E-cadherin antibody before patterning and repeated the patterning experiments (Figure 5-1A-F). Compared to the depressed colony-forming efficiency that we observed previously for cells in contact (Figure 5-4, solid blue bars), the cells exposed to anti-E-cadherin had colony-forming efficiencies that were similar with and without cell contact (Figure 5-4, striped blue and red bars), suggesting that E-cadherin is involved in this negative regulatory pathway.

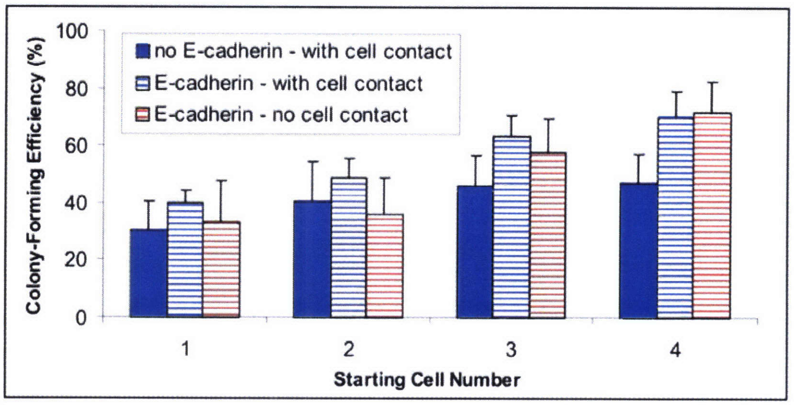

Figure 5-4: Investigating the effects of anti-E-cadherin antibody. Colony-forming efficiency of ABJ1 mESCs as a function of starting cell number for three cases – cells in contact without exposure to anti-E-cadherin (solid blue bars), cells in contact with exposure to anti-E-cadherin (striped blue bars), and cells without contact with exposure to anti-E-cadherin (striped red bars). Bars on experimental data indicate 1 standard deviation from the mean.

5.2.4 mESC Pluripotency in the BFC

To ensure that the BFC microenvironment was not negatively affecting mESC physiology, we patterned mESCs onto a cell-culture dish and, with the BFC clamped to the dish, grew the cells in this enclosed environment for 4 days. We then stained the cells for two markers of pluripotency: Oct-4 and Alkaline Phosphatase. On day 4, the colonies still retained their normal spherical morphology (Figure 5-5A) and exhibited high levels of both Oct-4 (Figure 5-5B) and Alkaline Phosphatase (Figure 5-5C).

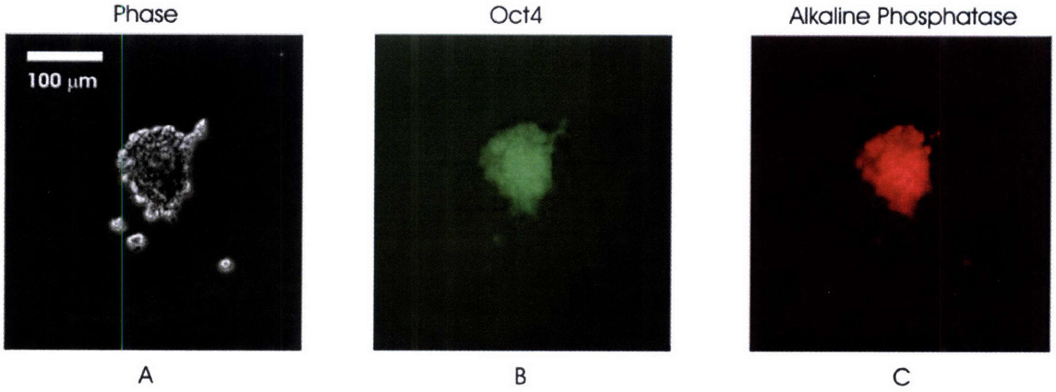

Figure 5-5: mESC pluripotency in the BFC. mESC colony on day 4 in the BFC environment: (A) phase image, (B) staining for Oct-4, and (C) staining for Alkaline Phosphatase.

5.3 Discussion

5.3.1 Diffusible Signaling

Previous experiments have shown that autocrine diffusible factors can be important for maintenance of pluripotency[19], showing that increasing the cell seeding density causes an increase in levels of SSEA-1 expression (Figure 5-6A, rightmost column). We performed similar density experiments, using Oct-4 GFP as a marker for pluripotency, also showing that increasing seeding density increases pluripotency (Figure 5-6B). Looking at proliferation, Zandstra *et al.* reports that the cell number on day 5 increases as the cell seeding density increases (Figure 5-6A, third column from the right), an obvious result. However, if you use their numbers to calculate the actual increase in cell number (total cell number on day 5 divided by input cell number), it increases from 60x, to 63x, to 70x, showing an increased *rate* of proliferation as the cell seeding density increases, indicating that diffusible factors are important in supporting growth. However, for a cell seeding density of 25,000 cells/cm^2, the increase in cell number on day 5 significantly decreases to 18x (Figure 5-6A, second column from right). We hypothesize that, at this high cell seeding density, the single cells are able to start clustering by the first day, allowing cell-cell contact to decrease proliferation. These results would then agree with our results, that increasing cell-cell contact causes a decrease in proliferation (e.g. colony formation).

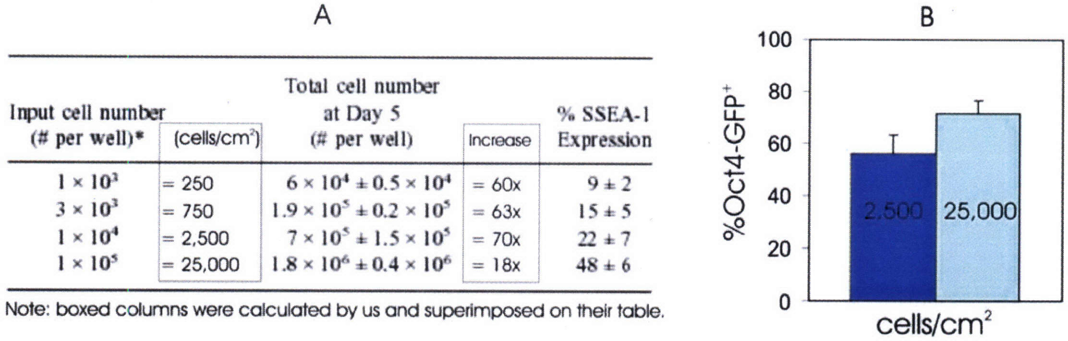

Input cell number (# per well)*	(cells/cm^2)	Total cell number at Day 5 (# per well)	Increase	% SSEA-1 Expression
1×10^3	= 250	$6 \times 10^4 \pm 0.5 \times 10^4$	= 60x	9 ± 2
3×10^3	= 750	$1.9 \times 10^5 \pm 0.2 \times 10^5$	= 63x	15 ± 5
1×10^4	= 2,500	$7 \times 10^5 \pm 1.5 \times 10^5$	= 70x	22 ± 7
1×10^5	= 25,000	$1.8 \times 10^6 \pm 0.4 \times 10^6$	= 18x	48 ± 6

Note: boxed columns were calculated by us and superimposed on their table.

Figure 5-6: Cell seeding density effects on mESC pluripotency. (A) Day 5 cell number and SSEA-1 expression as a function of the cell seeding density[19]. (B) Oct-4 GFP expression as a function of the cell seeding density.

In the two patterning experiments (Figure 5-1B and Figure 5-1E), we are turning cell-cell contact on and off. However, the question arises whether or not we are significantly modulating diffusible signaling between the contact and no contact experiments. To analyze the transport kinetics in our system, Batsilas *et al.* generated a stochastic model for autocrine cell cultures that characterizes the spatial range of secreted products[115]. We used their model to look at the transport of LIF, using published kinetic parameters: the LIF-LIFR association constant is ~10×10^{-8} $M^{-1}min^{-1}$[116], the number of LIF receptors per mESC is ~500[116,117], LIF diffusivity is 2.8×10^{-7} cm^2/s (estimated using the molecular size, since diffusivity scales as the reciprocal of the cube root of its molecular weight), the mESC radius is 10 μm (which we measured), and the BFC chamber height is 250 μm. Using their model, we determined that 99% of the LIF secreted by a cell is not recaptured by that same cell, thereby diffusing to adjacent, neighboring cells. Their model can also be used to determine the diffusion distance of secreted molecules; however this model only works for larger chamber heights, on the millimeter scale. They have published another stochastic model, to be used for smaller chamber heights, that we can use to characterize our experiments[118]. Using this model, we determined that the average trapping distance for a secreted LIF molecule is ~1.35 mm. This is a much larger distance compared to the clustered cells (spaced ~45 μm apart), and is large because the number of LIF receptors per cell is only ~500, so most of the secreted LIF does not become bound and continues to travel to other cells. Since the diffusion distance is so large, it would suggest that transport differences between the contact and no contact cases (~45 μm difference in cell spacing) are negligible. We can look at the differences in diffusion times between these two conditions, $t = L^2/D$, where t is the diffusion time, L is the characteristic diffusion length (the cell-cell membrane spacing), and D is the diffusivity of the secreted molecule. The difference in diffusion times for the cells in contact and without contact is only ~1 min. Therefore, compared to the mESC doubling time of ~14 hours[19], differences in diffusible signaling between the contact and no contract experiments are probably negligible.

However, there are other factors that could affect diffusive transport between cells. Convection in the flow chamber could speed up or slow down transport times, depending on the direction of flow. In these experiments, we tried to minimize any convective effects using a closed volume of media, keeping the BFC clamped to the cell-culture during the entire assay. We also left the BFC in the incubator, untouched, during the entire assay. To determine if these convective flows were significant enough to alter transport times, we could use fluorescent beads[119] to measure the magnitude and direction of flow inside a BFC chamber. If the flows were significant, we could try to isolate the flow source and minimize it (e.g., vibrations inside the incubator, absorption of media into the PDMS, variation in the clamping force of the binder clips). Another possibility is that diffusible factors are getting sequestered in the ECM, since LIF is already known to be trapped in ECM[120]. This could significantly reduce the amount of diffusible factors reaching the cells in the no contact experiment. To investigate this, we could use a LIF antibody to stain for LIF that was captured in the ECM. Furthermore, diffusible factors could also be absorbed by permeation driven-flow in the PDMS[121]. We hypothesized that this mechanism was occurring when loading the BFC microwells with cells, causing the cells to stick in the microwells. To correct this, we soaked the BFCs in PBS overnight, supersaturating the PDMS, thus making it unlikely to affect transport of diffusible factors here.

To further investigate whether diffusible signaling was transport-limited due to any of the reasons mentioned above, we could perform additional no contact experiments for cell spacings less than 45 μm, such as 15 μm or 30 μm, as long this spacing is not too close to enable cell-cell contact before measuring colony formation on day 2. If colony-forming efficiency increases compared to the 45 μm spacing, then that would suggest that the diffusible factors support colony formation, and that in 45 μm case, a significant amount of these factors were indeed transport-limited. There are several candidates for these autocrine diffusible factors, such as LIF[19,23] or BMP[16], which we could test by using antibodies against these diffusible molecules to try and lower colony-forming efficiencies back to the 45 μm spacing levels. This is similar to how we used anti-E-cadherin to restore colony forming efficiency in the contact experiments (Figure 5-4, striped blue bars). If colony-forming efficiency decreases compared to the 45 μm spacing, then that would suggest that diffusible factors inhibit colony formation, also being transport-limited in the 45 μm case. This could be caused by the hypothesized differentiating diffusible factors[19]. If colony-forming efficiency stays the same compared to the 45 μm spacing, then that suggests that the diffusible factors were not transport-limited in the 45 μm spacing case and that differences in diffusible signaling in the contact and no contact experiments were in fact negligible.

If this is true, then because the colony-forming efficiency for the 45 μm case is similar to the no cell signaling case (Figure 5-3A-B, solid red and yellow bars), this suggests that diffusible signaling is not playing a role in any of these patterning experiments. This would most likely be because there are too few cells compared to normal cell-culture conditions (~200 cells/cm^2 in the BFC vs. 5×10^5 cells/cm^2 in a normal cell-culture dish, a difference of 2500×). To estimate the local LIF concentration at a neighboring cell from a single secreting cell, assuming no uptake, we used a continuous point source model in 3-D[86]. For a cell concentration of 2.5×10^5 cells/mL, the LIF secretion was estimated using ELISA to be ~1-2 pM/day (experiment performed by Asiri Ediriwickrema in our lab). Therefore, assuming the secretion rate scales linearly, this yields a LIF secretion of $\sim4\times10^{-6}$ pM/day/cell. For a neighboring cell, located 45 μm away, the LIF concentration after 2 days is calculated to be $\sim6\times10^{-4}$ pM. This concentration is extremely low compared to the media LIF concentration of 500 pM, and therefore autocrine effects of LIF are probably negligible in our experiments. To further investigate the autocrine effects of LIF, we could repeat these experiments in no-LIF media. If the colony-forming efficiencies change, this indicates that LIF diffusible signaling can affect colony-formation, even for this low number of cells secreting such low concentrations of LIF. If the colony-forming efficiencies remain the same, it suggests that either the concentrations of LIF are still too low to affect colony formation, or that LIF may not directly affect colony formation at all.

Another potential issue to address is whether or not there are significant amounts of diffusible signaling *between* colonies. When fabricating the BFCs, we made the spacing between colonies 0.75 mm (Figure 5-1A and Figure 5-1D) to minimize any intercolony signaling. In terms of the diffusion distances, we used the above stochastic model[118] to determine that over 60% of secreted LIF can travel to distances larger than 0.75 mm. However, there are several reasons to believe that this intercolony signaling is negligible. First, we did not observe any spatial patterns in colony-forming efficiency, meaning that colony formation was independent of the presence of nearby colonies. Second, colony-forming efficiencies in the no contact experiments were similar to the efficiencies in the no cell signaling case (Figure 5-3A-B, solid red and yellow bars), indicating that even at this 45 μm spacing, diffusible factors are not important. Therefore, for the intercolony distances of 0.75 mm, almost 20× larger, diffusible signaling should also be negligible. To further investigate the effects of diffusible signaling at these larger distances, we could increase the cell-cell spacing within a group of cells above 45 μm, to 100-200 μm spacing, expecting that these colony-forming efficiencies would be similar to the 45 μm spacing and no signaling efficiencies.

Lastly, while we could turn on and off cell-cell contact, diffusible signaling was always present in our patterning experiments. It would then be interesting to try and remove diffusible signaling while maintaining cell-cell contact, which we might be able to accomplish using continuous flow. We have previously demonstrated that the BFC could successfully be interfaced to a flow chamber and used to pattern cells inside the chamber. Using continuous flow (operating at Peclet numbers $\gg 1$) to wash away the diffusible factors, we could then measure the colony-forming efficiencies from contact alone. We would make sure to keep the shear stress below ~6-10 dyn/cm^2, levels which Fok *et al.* showed did not affect mESC proliferation or differentiation[122]. It is important to note, however, that continuous flow cannot be started until after the patterned cells have attached to the substrate (usually after a few hours). Therefore, if diffusible signaling during these first few hours is significant enough to affect colony-forming efficiency, this experiment would not yield different results from our previous contact experiments. Yet, if colony-forming efficiencies did turn out to be greater in the contact experiments with diffusible signaling present, it would suggest the diffusible factors promote colony formation. If these efficiencies were less, it would suggest the diffusible factors inhibit colony formation. If colony-forming efficiencies remained the same, regardless of whether diffusible factors were present or not, it would suggest that either the flow was not fast enough to effectively sweep away the diffusible factors, that diffusible signaling was significant during the first few hours of cell attachment (when there was no flow), or that these diffusible factors are not actually playing a significant role in colony formation.

5.3.2 Contact-Mediated Signaling

Assuming that we have ruled out effects from diffusible signaling, the question is whether factors other than cell-cell contact could be causing this depression in colony formation. One possibility is that in our closed chamber experiments, with minimal convection, larger cell clusters are being locally depleted of nutrients. To test this, we would repeat our BFC experiments, removing the BFC after patterning, so the cells are in an open cell-culture dish. This will allow media convection to take place and possibly restore any local depletion of nutrients around the cells. Note that adding this convection will also affect the transport of diffusible factors. In addition, in these open chamber experiments, we could try replacing the media every 12 hours, to determine if this helps to restore colony-forming efficiency. Overall, it is unlikely that nutrient depletion is responsible. First, based on the arguments above for diffusible signaling, it is unlikely that there were significant differences in nutrient transport between the contact and no contact cases. And since the no contact experiments did not show a depression of colony-forming efficiency in larger cell clusters, this was probably not occurring for the cells in contact. Second, in the closed chamber experiments, without feeding the cells after five days, we were still able to grow up mESCs into colonies (Figure 4-3), making nutrient depletion unlikely over the course of our two-day assays.

We will now consider the possibility that the depression in colony-forming efficiency is indeed a cell contact-mediated effect. We saw that, for cells in contact, colony-forming efficiency flattens out as a function of starting cell number, therefore a cluster of four cells behave with a similar colony-forming efficiency as a single cell (Figure 5-2A, solid blue bars). This flattening out of colony-forming efficiency is most likely caused by two competing effects – the increasing number of starting cells increases the chance that any one of those cells in a cluster will proliferate (as we saw in the no cell signaling case), while the contact-mediated signaling decreases colony-forming efficiency, overall resulting in a curve that flattens out. To determine the effects from contact alone, we need to look at the *difference* in efficiencies between the contact and no signaling cases, which does *increase* with starting cell number, suggesting that contact-mediated signaling is playing an increasing role in this negative regulatory pathway.

Another way to do these experiments that would allow us to observe the isolated effects of contact-mediated signaling would be to measure the colony-forming efficiencies at the single-cell level. For example, for each cell in a four-cell cluster, determine whether *each* of those four cells formed into a colony or not, rather than if *any* of them did. We could compare each of these efficiencies, for each starting cell number, to the expected single-cell colony-forming efficiencies, which was determined by us, and other groups[25], to be ~37.5%. Note that this type of single-cell analysis could be done fairly easily for the no contact case, since cells in a group have discrete borders and even with colony-formation, separate colonies are formed. However, in the contact case, it would be more difficult to determine cell fate for each of the cells in a cluster, and might require imaging of the cells every few hours, to make individual cell tracking easier. Additionally, one could use live microscopy to video the cells over the entire two-day assay. Note, however, that both of these additional manipulations could affect the cell signaling environment due to induced convection from handling the chip. Additionally, if the cells are going to be imaged for long periods of time, we would recommend using an incubated microscopy stage, to ensure maintenance of temperature and CO_2 levels.

Furthermore, it would also be interesting to investigate colony-forming efficiency as a function of the geometry of cell-cell contact. In mouse development, the geometry of cell-cell contact has shown to be important in determining cell fate[123] – the development and orientation of cell polarity in early embryonic blastomeres is initiated more effectively in the presence of cell-cell contact[124,125]. In our BFC experiments, we could measure the colony-forming efficiency as a function of the level of cell-cell contact. For example, the cells in a four-cell cluster could be patterned in a tight cluster (Figure 5-1B), as a line of four cells, or any configuration in between. These different patterns will generate differences in the level of cell-cell contact, which in turn, may affect colony formation. In our experiments, we observed the majority of clusters being patterned as tight clusters, although this might not have always been the case. To effectively modulate the degree of cell-cell contact, for a constant number of starting cells, we could fabricate a BFC that used different-shaped microwells, from a circular well to generate tight cell clusters to a high-aspect ratio oval well to generate lines of cells. We could then image the cells in a cluster and use image processing software (e.g., MATLAB) to quantify the level of cell-cell contact (e.g., the percentage of cell membrane perimeter that is overlapping with other cells). After patterning, we would observe colony-forming efficiency for *each* cell in the cluster, as described above. These results would also be an excellent way to validate that the depression in colony-forming efficiency was indeed caused by cell-cell contact, and not diffusible signaling. Since we are keeping the number of cells in a cluster constant, diffusible signaling between a tight cell cluster and a line of cells should be similar. Therefore, any differences in colony-forming efficiency should be due to cell-cell contact alone. As our lab continues to increase its automated microscopy capabilities, imaging large arrays of patterned cells, and develop efficient post-processing algorithms, this type of quantitative analysis becomes feasible.

To further investigate the mechanism behind the contact-mediated depression in colony formation, we should look at the timing of the observed events. We first determine the starting cell number a few hours after patterning, once the cells are attached to the substrate. Then, at day 2, we determine whether or not any of the cells in a cluster have formed a colony. If there is not a colony there, as is the case for many of the larger cell clusters with contact, then that means that *all* of the cells in that cluster died. So after patterning, the contact-mediated signaling triggers downstream signaling pathways that most likely led to apoptosis for all those cells. Now, it is possible that it is a *non-contact* apoptotic event. With a single-cell colony-forming efficiency of ~40%, that means that 60% of cells are most likely undergoing apoptosis on their own anyway. Therefore, it is possible that if one cell in a cluster dies, it could then signal the other cells in a cluster to die, either through the release of pro-apoptotic diffusible factors or toxic metabolites[126]. However, this is less likely because of the higher colony-forming efficiencies in the no contact case. As described above, we could repeat the no contact experiments with cell spacings less than 45 μm in order to rule this out. Overall, it seems that apoptosis may be responsible when a colony has not formed from a cluster of cells and it would be worthwhile to test for this.

Apoptosis is characterized by specific cellular changes. In the early stages of apoptosis, caspases are activated and the mitochondrial transmembrane potential dissipates. Then, phosphatidylserine, normally located on the cytoplasmic surface of the cell membrane, becomes exposed to the extracellular environment. Plasma membrane integrity is also lost and nuclear chromatin becomes condensed. Many of these cellular changes can be assayed to test whether or not a cell is undergoing apoptosis. However, since we wish to investigate apoptosis of the patterned cells, retaining the spatial information of the starting cell number, we are limited to *in-situ* assays. There are several apoptosis kits that we can utilize for these *in-situ* assays – including Annexin-V staining of phosphatidylserine (Invitrogen, V13241), stains to test membrane integrity or condensed chromatin (Invitrogen, V23201), and staining for intracellular caspase activation (Invitrogen, V35118).

To best understand the mechanism and timing of the contact-mediated signaling leading to apoptosis, it would be beneficial to perform these apoptosis assays at multiple time points between cell attachment and when we assay for colony formation on day 2. Since the highest degree of contact-mediated apoptosis is for the four-cell clusters, we only need to observe apoptosis for this starting cell number. We could start by flipping four BFCs, each BFC to be used to assay a different time point ($t = 4, 12, 20, 28$ hrs after flipping). Then, after the cells have attached ($t > 2$ hrs after flipping), we would determine the locations of all the four-cell clusters in all four BFCs. Afterward, using one of the above apoptotic kits, we would stain the cells in a BFC at its appropriate time point and image all the four-cell clusters Using these images we could determine how many of the four starting cells were undergoing apoptosis, at each time point. This might allow us to characterize the dynamics of apoptosis. For example, if a majority of the four-cell clusters had one cell undergoing apoptosis at $t = 4$ hrs, two cells at $t = 12$ hrs, three cells at $t = 20$ hrs, it might suggest that the apoptosis was occurring in one cell and then signaling other cells in a cluster to undergo apoptosis. It would be worthwhile to repeat these experiments for the no contact case to determine if this was a pro-apoptotic diffusible factor. However, if a majority of the four-cell clusters had zero cells undergoing apoptosis at t = 4 hrs, t = 12 hrs, and t = 20 hrs, and then had three cells undergoing apoptosis at t = 28 hrs, it would suggest that while the contact-mediated signaling begins early on in all of the cells, it takes some time to eventually trigger apoptosis.

Assuming that the depression in colony formation was caused by a contact-mediated signaling leading to apoptosis, the next obvious question is why doesn't this signaling occur when cells are proliferating *within* a colony? If increasing levels of cell-cell contact lead to apoptosis, it would suggest that colonies would not be able to grow at all, because as they got larger, the level of cell-cell contact would increase and inhibit their growth. One possibility is that the cells respond differently to the cells patterned next to them versus the cells proliferating from them. However, our cells are clonal and were in colonies just hours before they were patterned. Though, this does raise the interesting question of how breaking up colonies into single cells changes their behavior. In our experiments, we trypsinized and then triturated the cell solution to ensure that they were first broken up into single cells before they were reformed into clusters inside the BFC microwells. It could be that enzymatic digestion and triturating removes membrane-bound factors, initially making the cells more sensitive to the contact-mediated signaling, and by the time they start proliferating in colonies these membrane-bound factors are restored. We could test this is multiple ways. First, we could measure colony-forming efficiency for intact clusters (e.g., cells that were broken up from colonies into 2-4 cells, but not into single cells and then reformed) to determine if there is a difference in behavior between intact and reformed cell clusters. If there was no longer a contact-mediated depression in colony-forming efficiency, it might suggest that enzymatic digestion was actually removing important membrane-bound factors. We could then repeat the patterning experiments, using *non-enzymatic* digestion to separate the colonies into single cells, to see if this recreates the depression in colony formation.

Another possibility is that in colonies, there are so many cells that the increased number of cells wins out over the negative effects of the contact-mediated signaling. To test this out, we could repeat our contact experiments for larger numbers of starting cells. Previously, we patterned clusters of 1-4 cells, however, by using larger-sized microwells we could easily increase the starting cell number up to 10-20 cells. Looking at colony formation as a function of these increased number of starting cells, we would determine if the colony-forming efficiency starts to eventually increase for > 4 cells or if continues to flatten out. If it does start to increase, approaching 100%, it might indicate that the contact-mediated signaling eventually saturates. After all, the level of cell-cell contact can only go so high. This relates to the "kissing number problem" in mathematics, which states that in 2-D (since the cells are patterned on a bottom substrate), that a maximum of six spheres can surround an inner sphere. Therefore, it is possible that in a colony, the contact-mediated signaling saturates with this maximum level of cell-cell contact, and as the number of cells increase beyond this, it starts to increase the colony-forming efficiency.

5.3.3 Signaling Pathways

Overall, it seems likely that contact-mediated signaling is playing a role in the depression in colony formation. The next important question is – what signaling pathways come between the initial cell-cell contact and apoptosis? Our E-cadherin experiments suggest that E-cadherin is involved in this negative regulatory pathway. Previous studies have shown that cell agglomeration of mESCs in embryoid bodies negatively affects cell proliferation[127] and that E-cadherin mediates this process[128], possibly occurring in a similar fashion to what we observed here.

To further investigate whether E-cadherin signaling was indeed responsible for the depression in colony formation, we could pattern the cells in contact with E-cadherin-coated beads[129,130]. Since the concentration of E-cadherin on the bead can be varied, we could modulate E-cadherin signaling independently of the level of contact. For example, by patterning a single mESC next to a single E-cadherin-coated bead, we could then measure colony-forming efficiency as a function of E-cadherin concentration on the bead. Since these experiments would only require a single mESC, the efficiencies would not include the effects from having multiple cells in a cluster, which increases the chance that a colony will form. Instead, the efficiencies would only include the effects from E-cadherin signaling. We could then compare the colony-forming efficiencies of this single mESC-bead pair to the single mESC colony-forming efficiency of ~37.5%. As the bead E-cadherin concentration increases, we would expect this colony-forming efficiency to decrease.

In contrast to modulating the amount of E-cadherin signaling, using the E-cadherin-coated beads, we can also control the removal of E-cadherin signaling by varying the concentration of anti-E-cadherin antibody in the media. We used a concentration of 40 μg/mL, since that was what Dang *et al.* used to prevent contact-mediated agglomeration of embryoid bodies[128]. However, it would be interesting to repeat these experiments for lower concentrations of antibody, seeing if we could phase out the restoring effects of the antibody, returning the colony-forming efficiencies back to the depressed levels as in the contact experiments. We could also use an anti-E-cadherin antibody concentration greater than 40 μg/mL, however we would expect that the colony-forming efficiencies would not get any higher, since they are already at the no contact levels.

It would also be useful to rule out non-specific effects of the anti-E-cadherin antibody by doing an isotype control experiment. While the anti-E-cadherin antibody did actually help to restore colony formation in our experiments, suggesting that the antibody was binding to its specific target, it is also possible that the antibody had non-specific effects that were the cause of this restoration in efficiency. Since our anti-E-cadherin antibody isotype is rat IGgl (clone DECMA-1, Sigma, U3254), we should repeat our contact and no contact experiments using a rat IgG1 isotype control (Ebioscience, 16-4301), immersing the cells in the same antibody concentration of 40 μg/mL for 2 hrs. It is unlikely that the colony-forming efficiencies are greater in the isotype control experiment, since the anti-E-cadherin efficiencies were already at the no contact levels. However, if the colony-forming efficiencies are the same, that would suggest that there are non-specific effects from this antibody isotype and that E-cadherin signaling was not directly responsible for the restoration in efficiencies. If the colony-forming efficiencies are less in the isotype control experiments, at the contact experiment levels, this would suggest that the anti-E-cadherin antibody was binding to its specific target, causing the observed restoration in colony formation.

Furthermore, we could also modulate E-cadherin signaling in other ways, such as using siRNA to repress expression of the E-cadherin gene at the transcriptional level[112].

Or, we could target the downstream products of E-cadherin, such as β-catenin. We could use a glycogen synthase kinase-3 (GSK-3) inhibitor, such as 6-bromoindirubin-3'-oxime (BIO), to increase Wnt signaling[17]. This would lead to an increase in the levels of β-catenin, since Wnt signaling has been shown to increase cytoplasmic levels of β-catenin[131]. In the contact experiments, we could determine if adding BIO to the media depresses colony-forming efficiency even further. More interestingly, in the no contact experiments, we could determine if adding BIO would depresses colony-forming efficiency at all, thus simulating the downstream effects of E-cadherin signaling without actually requiring cell-cell contact.

It is also important to look at the downstream signaling pathways of E-cadherin, and other mESC cell-cell adhesion molecules, to see if we can determine how contact leads to a depression in colony formation. Nagano *et al.* characterized a large subset of all the proteins expressed in mESCs and found that there were several proteins that were important in cell-cell adhesion signaling[114]. In addition to E-cadherin, three other proteins were expressed – including radixin, tight junction protein, and integrin binding protein. Radixin helps regulate the cytoskeleton, and while little is known about its downstream signaling pathways, radixin is suspected to be essential for cellular proliferation[132]. Tight junction protein 1, or zonula occludens 1 (ZO-1) protein, has been shown to be important in numerous cell processes, including proliferation. In endothelial cells, ZO-1 overexpression leads to a reduction in ZO-1 nucleic acid binding protein (ZONAB), followed by a decrease in nuclear cell division kinase CDK4, stopping cell proliferation[133,134]. Therefore, ZO-1 could also be involved in our contact-mediated depression in colony formation. Integrins are involved mostly in cell-ECM adhesions and many of their signals converge on cell cycle regulation, directing cells to proliferate or die[135]. In mESCs, integrin signaling leads to an increase in cytoplasmic levels of β-catenin[136,137]. It would be useful to repeat our patterning experiments using antibodies to knock out signaling from radixin, tight junction protein, and integrin to determine the effects on colony formation.

Looking at E-cadherin signaling, E-cadherin is known to increase levels of β-catenin in the cytoplasm and nucleus. β-catenin forms a complex with T cell factor and lymphoid enhancer family transcription factors, to stimulate STAT3 transcription, followed by STAT3 protein accumulation in the cytoplasm, leading to an increase in pluripotency[131]. Therefore, it seems unlikely that E-cadherin signaling would cause a depression in colony-forming efficiency. One possibility is that colony formation and pluripotency are not necessarily connected. Zandstra *et al.* demonstrated that increasing amounts of LIF in the media led to increases in mESC pluripotency (as demonstrated with SSEA-1 staining), but did not change overall proliferation[19]. He later showed that increasing LIF increased the levels of Oct4-GFP, and that growth rates either slightly increased or stayed the same, depending if the cells were differentiated or undifferentiated[15]. Overall, Zandstra's results demonstrate that pluripotency and proliferation are not always coupled, and therefore our E-cadherin mediated depression in colony formation might be consistent with the pro-pluripotency effects of E-cadherin signaling.

Another interesting possibility is that the depression in colony-formation is not directly caused by E-cadherin signaling, but instead, caused by a lack of integrin signaling. It has been shown that higher levels of cell-cell contact cause decreased levels of cell-ECM interactions[138]. Therefore, for our larger cell clusters with contact, it is possible that cells are adhering more to each other than the bottom substrate, decreasing cell-ECM interactions and integrin signaling. Depending on the influence of both signaling pathways, it is possible that the lack of integrin signaling and decreased levels of β-catenin wins out over the E-cadherin-mediated increase in β-catenin, overall resulting in decreased pluripotency. If pluripotency and colony formation are coupled, this could cause our observed contact-mediated depression in colony-forming efficiency. This mechanism would still be consistent with our anti-E-cadherin antibody experiments, since the antibody reduced cell-cell interactions, possibly allowing increased cell-ECM interactions that led to the restoration in colony-forming efficiency. We could investigate this potential mechanism in two ways. First, we could try and increase the level of cell-ECM interactions for the cells in contact. Our BFC experiments were performed on a bare TCPS dish. By patterning the cells onto more adhesive ECMs, like gelatin, this could increase the level of cell-ECM interactions and integrin signaling, possibly restoring colony-forming efficiency for the cells in contact. Second, we could try and decrease the level of cell-ECM interactions for the cells not in contact. By using an anti-integrin antibody on patterned cells not in contact, this may reduce integrin signaling, leading to a depression in colony formation without even requiring any cell contact.

Chapter 6: Conclusions

In this chapter, we conclude with the major contributions of the thesis. We then discuss several ongoing collaborations using the BFCs, demonstrating the ease-of-use and transferability of this technology. Lastly, we describe several potential applications of the BFC.

6.1 Thesis Contributions

The contribution in this thesis consists of several technical achievements, the development of our two cell patterning technologies, and a biological achievement, determining the effects of cell-cell contact on mESC colony formation.

With the creation of our DEP square trap, we demonstrated the strongest, planar, single-cell, nDEP trap realized to-date. We were also able to further validate our modeling software, matching experimental results to modeling predictions for both beads and cells. We showed that we could use this software to evaluate the performance of new trap designs, optimizing their geometries even before the traps are fabricated. Furthermore, we made the software freely available to the scientific community. We also further improved the nDEP square trap to include interdigitated electrodes, allowing almost complete prevention of cells sticking to the substrate, yielding a high-efficiency cell patterning tool that worked with multiple cell types.

With the creation of our BFCs, we demonstrated a novel cell patterning technology that enables us to pattern cells with single-cell resolution anywhere on a substrate and onto any substrate. We demonstrated large-scale patterning of mESCs, with patterning efficiencies > 75%, onto a variety of substrates – a cell-culture dish patterned with gelatin, a 3-D substrate, and even another layer of cells. In addition, the ease-of-use of this technique has allowed this technology to be transferred to several engineering and biology labs, as discussed in Section 6.2: Ongoing Collaborations with the BFC.

Lastly, we used the BFCs to answer an interesting biological question – how do the seeding conditions of mouse embryonic stem cells affect their proliferation? We used the BFC to pattern small groups of cells, with and without cell-cell contact, allowing incremental and independent control of contact-mediated signaling. We present quantitative evidence that cell-cell contact plays an important role in depressing mESC colony formation, and show that E-cadherin is involved in this negative regulatory pathway. We thus provide an enabling technology that can be used to manipulate and monitor cells in unique ways.

6.2 Ongoing Collaborations with the BFC

Due to the numerous capabilities of the BFC, including its ease-of-use, we have begun several collaborations with other labs. The Kristen Van Vliet lab, in the Department of Materials Science and Engineering at MIT, has started using BFCs to pattern mesenchymal stem cells. The Van Vliet lab creates their own substrates using polyelectrolyte multilayers (PEMs), allowing tunable substrate mechanical compliance[139]. They have been investigating cell-substrate interactions, particularly the effects of substrate compliance on stem cell fate. They would like to use the BFC to pattern mesenchymal stem cells in a grid, enabling cell tracking of visual markers and cellular physical properties (using atomic force microscopy (AFM)).

We have also been collaborating with the George Daley Lab, at the Children's Hospital in Boston, working with Frank Yates and Elayne Chan. In this collaboration, we are interested in using BFCs to pattern human embryonic stem cells (hESCs) for cell tracking and control of cell-cell signaling. We have already demonstrated BFC patterning of H9 hESCs (a tryspin-adapted cell line), patterning single hESCs on top of a layer of matrigel or a layer of murine embryonic fibroblasts (MEFs). The single hESCs on top of matrigel did not proliferate in these experiments, but the single hESCs on top of a layer of MEFs did form hESC colonies (Figure 6-1).

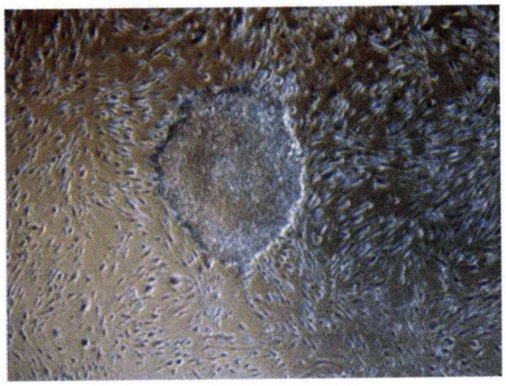

Figure 6-1: hESC colony formation after BFC patterning of single, trypsin-adapted H9 hESC on top of a layer of MEFs.

Another collaboration of ours is with Sridhar Ramaswamy's lab at the Massachusetts General Hospital's Cancer Center, working with Andrew Yee. In this project, we are interested in exploring the existence of cancer stem cells, possibly enabling targeted cancer therapies. In this collaboration, we wish to use the BFCs to pattern cancer cells in a grid (A375-melanoma and H1975-lung), allowing easy long-term cell tracking of cell proliferation. By staining the cells before seeding, the intensity of the stain can be monitored as the cell proliferates and the dye is partitioned. This could provide insight into the proliferation rates of the cancer cells, and whether there is any asymmetric cell division, possibly validating the existence of any cancer stem cells. So far, we have demonstrated patterning of H1975 cancer cells and tracked proliferation over three days (Figure 6-2A-C) and are just beginning to stain the cells and demonstrate automated large-scale cell tracking.

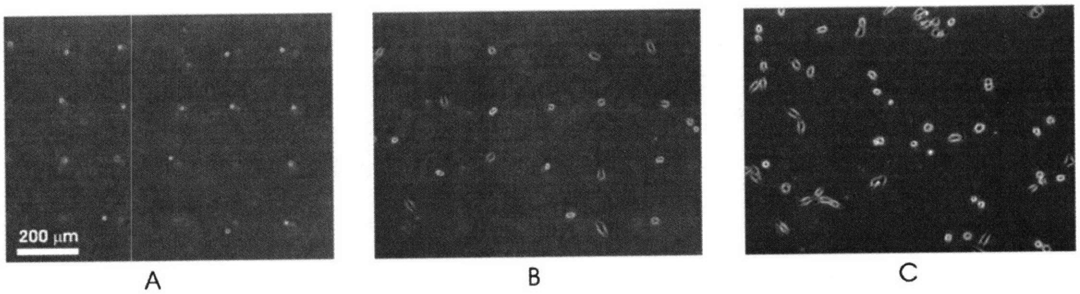

Figure 6-2: BFC patterning of lung cancer cells (H1975) on (A) day 0, (B) day 1, and (C) day 2.

We recently began additional collaborations using the BFC. Peter Sorger, in the Department of Systems Biology at Harvard Medical School, would like to use BFCs to pattern single cells to monitor heterogeneous behavior of apoptosis induced by various drugs. And lastly, Bevin Engelward, in the Biological Engineering department at MIT, would like to use the BFCs for two different projects. The first is a similar application to one of the aims in this thesis, using the BFC to control cell-cell signaling in embryonic stem cells. The second application is to use BFCs for long-term cell tracking of immunofluorescence.

6.3 Future Applications of the BFC

In addition to the collaborations mentioned above, there are numerous other potential applications that can be explored with the BFC technology. In general, since the BFC is compatible with any cell type, it can be used for long-term tracking or controlling cell-cell signaling in other cell types of interest.

More specifically, we could also look into the effects of starting cell number on maintenance of mESC pluripotency. By extending our cell patterning assays to the fourth day in culture, we could observe various pluripotency markers in the colonies that formed – such as Oct-4, Nanog, or Alkaline Phosphatase – to determine if starting cell number affects pluripotency as it did proliferation. While pluripotency levels were maintained when seeding clusters of 1-4 mESCs (Figure 5-5B-C), others have shown that seeding clusters of thousands of mESCs can cause differentiation[27]. It would therefore be interesting to use the BFC to seed larger clusters of cells – from tens, to hundreds, to thousands – to determine a quantitative relationship between cluster size and pluripotency levels, and if the relationship is linear or binary (e.g., at around five hundred cells pluripotency is suddenly lost) .

We could also explore the effects of starting cell number on hESC colony formation. Typically, hESCs are seeded as clusters of hundreds of cells[140], however it would be interesting to use the BFCs to precisely control starting cell number to optimize hESC colony-forming efficiency. The BFC can be engineered to seed different sized clusters of hESCs on the same substrate, from 25-800 cells, using a BFC with a constant microwell depth, but a varying the microwell diameter (Figure 6-3A). This will produce clusters of varying diameters, but all having the same height. Alternatively, the height of the hESC cluster could also be modulated, using a constant cluster diameter (Figure 6-3B). Modulating colony shape could enable us to investigate whether colony morphology actively regulates self-renewal, or whether it is merely the byproduct of undifferentiated cells clustering together.

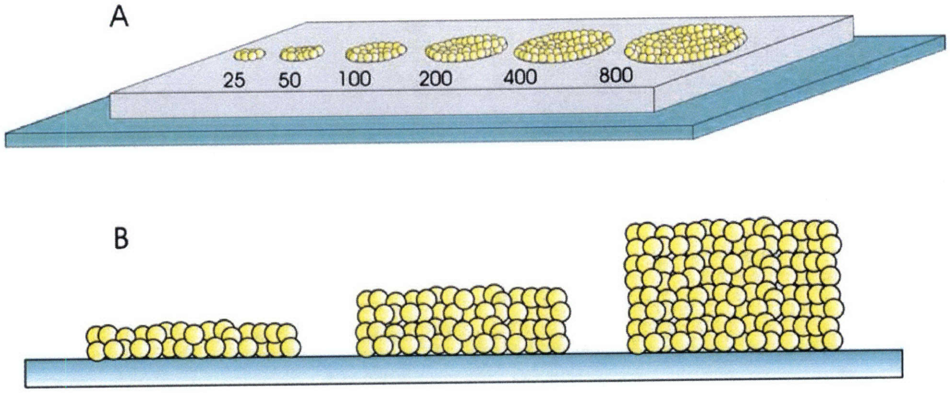

Figure 6-3: BFC patterning of hESCs to control colony formation. (A) Patterning a range of cell cluster sizes, from 25-800 cells, varying cluster diameter but keeping cluster height constant. (B) Patterning clusters with the same diameter but with a range of heights.

In addition to self-renewal, stem cell differentiation could also be explored using BFCs. These experiments would be very similar to the patterning experiments in Chapter 5, except using a mixed population of differentiated and undifferentiated cells (Figure 6-4A). The cells would randomly be trapped in different ratios in the microwells, allowing incremental control of differentiating factors. If differentiation does indeed increase with the number of differentiated cells, cell-cell contact could again be turned on (Figure 6-4B) and off to determine if these differentiating factors are diffusible or contact-mediated.

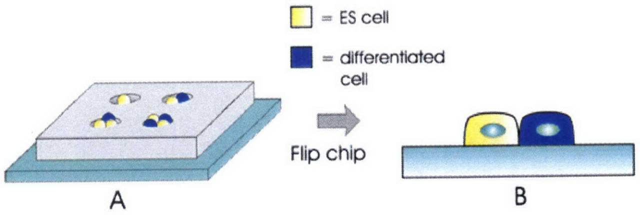

Figure 6-4: BFC patterning for studying differentiation. (A) Repeating the patterning experiments in Chapter 5, except with a mixed population of ESCs and differentiated cells. These mixed populations can be patterned without or (B) with cell-cell contact.

Another potential application for the BFC is patterned chemotaxis assays. These are currently performed using switchable substrates[110], which trade off substrate chemistry requirements and ease of use for temporal control of motility. The BFC can be used to pattern cells on a substrate with another cell type. Cells could then be monitored to determine the influence of chemotactic factors on cell migration (Figure 6-5A). Additionally, BFCs could be used to investigate cell migration, particularly over various kinds of topography. Since the BFCs can pattern onto any substrate, cells can be monitored as they travel over 3-D obstacles (Figure 6-5B).

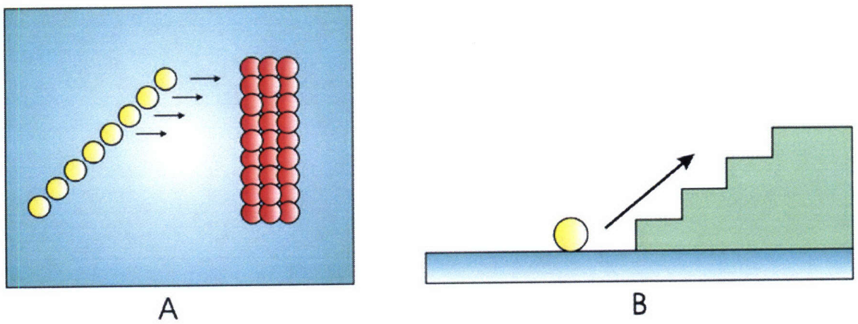

Figure 6-5: BFC patterning for (A) chemotaxis assays or (B) cell migration studies over obstacles.

In collaboration with the George Daley lab, we are also looking into using the BFC as a novel cloning tool. Currently, most researchers use an automated FACS machine in order to place single cells in different wells of a 384-well plate. This is not only expensive ($60/hr), but the technique also has a substantial error, sometimes placing zero or multiple cells in a well instead of a single cell. By making a BFC with single-cell sized microwells, with the same spacing as the wells on a 384-well plate, the BFC could trap single cells and then flip each cell into a separate well of a 384-well plate (Figure 6-6). We have already begun to demonstrate this on a smaller scale using a 5×5 BFC array that flips single 3T3 murine fibroblasts into 25 wells of the 384-well plate. We are continuing to improve the technique and will eventually expand it for use with hESCs adapted for single-cell cloning.

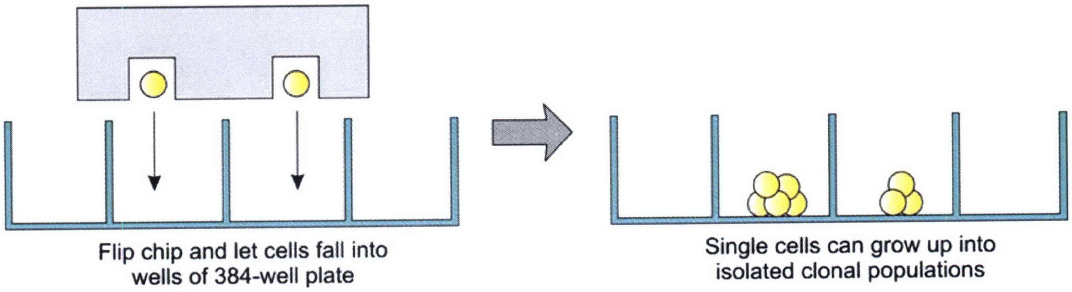

Figure 6-6: BFC to be used for a novel cloning technology. By flipping single cells into the wells of a 384-well plate, clonal populations can grow up in isolation.

Lastly, in additional to the numerous applications mentioned above, there can also be improvements to the chip-making process. Currently, we photopattern SU8 posts on Si master wafer, pour the PDMS over the wafers, cure it, and then manually peel off the BFC microwells. While it is fairly reliable, the SU8 posts sometimes do rip off the Si master wafer, decreasing the overall microwell pattern fidelity, which translates to decreased cell patterning efficiencies. Only a small fraction of the chips on a given wafer become like this, so we usually just throw out those corrupted chips, given that they only cost fifteen cents per chip. However, making this fabrication process more robust, so the SU8 posts do not rip off, would increase throughput when making up new BFCs.

Furthermore, none of our collaborators currently have the capabilities to fabricate their own BFCs. Therefore, not only are we doing the initial fabrication of the Si master wafer, but we are also making up new BFCs for them every time they need more. While we could give them the Si master wafers, allowing them to pour the PDMS themselves, the frailty of the SU8 posts make this option undesirable. Therefore, Salil Desai in our lab recently came up with a new process that uses a plastic mold (Smooth-On, Smooth-Cast 310) as a replacement for the Si master wafers (Figure 6-7A-D). By molding plastic into an already-made BFC, an inverse mold with posts is formed, identical to the Si master wafer. The PDMS can then be poured onto these plastic posts, instead of the SU8 posts, allowing repeated manufacturing without damaging the post structures. While Salil already has created these molds at the single chip level, he is now working on making them at the whole-wafer level.

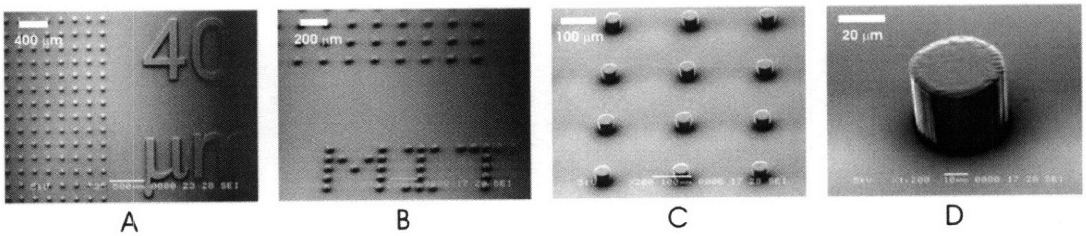

Figure 6-7: SEM images of the plastic posts: (A) array with text, (B) array with MIT posts, (C) closer view of the array, and (D) a single post.

Appendix A: Modeling Software Functionality

In this appendix, we demonstrate the functionality of the modeling software by using it to investigate the trapping behavior for three different trap geometries – our planar nDEP square trap[45], the 3-D nDEP octopole[68], and a 3-D pDEP points-and-lid-geometry[57]. The model revealed interesting trapping behavior – such as multipolar DEP force effects, trap size-selectivity, and effects from varying the flow chamber height – and enabled quantitative explanations of these behaviors.

Modeling Parameters

We compare the trapping behavior of three trap geometries found in the literature: our planar, nDEP square trap[45], the 3-D nDEP octopole[68], and a 3-D pDEP points-and-lid-geometry[57] (Figure A-0-1).

For these results, the applied signal was always a 5 V_p sine wave at 5 MHz. The media density was 1000 kg/m^3 with a relative permittivity of 80. The solution conductivity was 1.5 S/m for the nDEP square and octopole traps, which is the typical conductivity of cell-culture media, and 0.01 S/m for the pDEP trap, which approximates the conductivity for previous pDEP cell trapping experiments[52,57].

We modeled all particles as cells with a density of 1071 kg/m^3, a cell cytoplasmic relative permittivity of 75, and a cytoplasmic conductivity of 0.75 S/m. The cell membrane had a conductance of 22 mS/cm^2, a capacitance of 1.6 µF/cm^2, and a thickness of 1 nm. These values were taken from Gascoyne[99]. The cell diameter was 14 µm, except when varying cell diameter, in which case it ranged from 2-24 µm in 2-µm increments.

For all cases, the chamber width was 4 mm. The chamber height was 40 µm, except when varying chamber height when it ranged from 40-200 µm in 40-µm increments. The simulations used a flow rate resolution of 10 µL/hr for the nDEP square trap, 1 µL/hr for the nDEP octopole, and 10 µL/min for the pDEP trap. The starting position of the cell was in the center of the square electrode and on the bottom substrate for the nDEP square trap, the center of the point electrode and on the bottom substrate for the pDEP trap, and in the center of the quadrupole and in the center of the flow chamber for the nDEP octopole trap. These positions were chosen based on the trapped particle locations in each of these traps[45,57,68], although the software allows the user to specify the particle starting position anywhere within the simulated space.

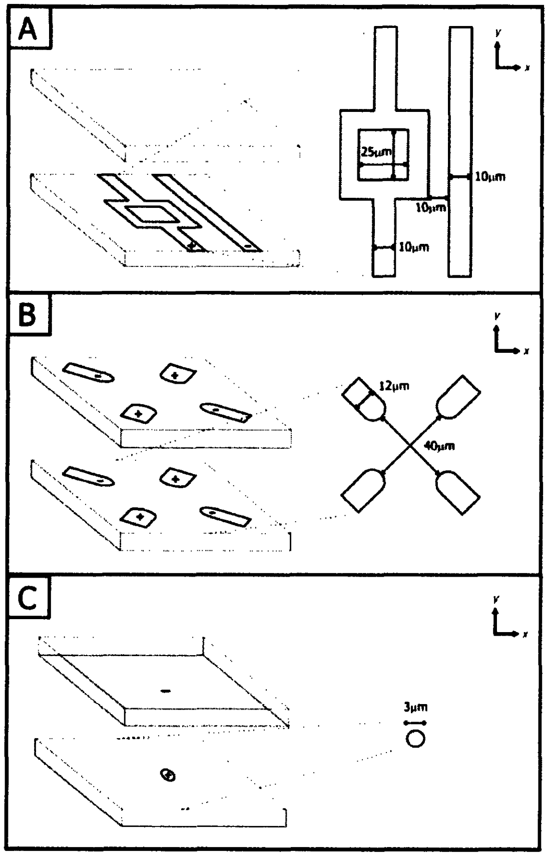

Figure A-0-1: The three simulated trap geometries. (*A*) The planar nDEP square trap, consisting of one square electrode with inner square side length of 25 μm and another line electrode spaced 10 μm away. All electrode widths are 10 μm. (*B*) The 3-D nDEP octopole with no phase shifts between the quadrupoles on the top and bottom surface. The electrode width is 12 μm and the tip-to-tip electrode spacing is 40 μm. (*C*) The 3-D pDEP points-and-lid geometry, consisting of a 3-μm point electrode on the bottom surface and a planar electrode on the top surface.

Multipolar DEP Force Effects

For all three trap geometries, we simulated the maximum flow rate versus cell diameter for multipole contributions ranging from n=1 to n=7 (where n=1 corresponds to the dipole contribution, n=2 corresponds to the dipole plus quadrupole contribution, etc). n=7 was the highest multipole contribution we could simulate at our 1-μm grid resolution before running out of memory (Intel Pentium 4, 2.26 GHz processor, 1 GB RAM). We defined the "number of multipoles needed" as the number of multipoles required to best approximate the true maximum flow rate. We set this value as the number of multipoles that bring the maximum flow rate within 15% of the maximum flow rate when n=7.

The nDEP square trap is only symmetric in the y-direction (Figure A-0-1A), making its electric fields more complex than the other two traps, which are symmetric in both the x and y-directions. We see that as the cell size increases, the number of multipoles needed also slowly increases (Figure A-0-2A). The trap size is of the same order as the cell size, so higher-order poles are expected to be induced[80].

The nDEP octopole was simulated with no phase shifts between the upper and lower plane (Figure A-0-2B). Therefore, every positive electrode on the top of the flow chamber has a positive electrode positioned directly below it on the bottom of the chamber. The same is true for the negative electrodes. This type of configuration creates the strongest trapping against the direction of fluid motion[68]. We see that the maximum number of multipoles needed for this geometry is $n=1$ – the dipole contribution alone is enough to approximate the maximum flow rate (Figure A-0-2B). Although inclusion of the quadrupole force ($n=2$) was necessary to levitate the cells in the center of the trap, also shown previously[68], this levitation effect did not significantly change the maximum flow rate. Therefore, $n=1$ was still sufficient to solve for the maximum flow rate in this trap.

The pDEP trap consists of a 3-µm point electrode on the bottom surface with a lid electrode on the top surface (Figure A-0-1C). We see that the number of multipoles needed increases with cell diameter, at an even faster rate than the square nDEP trap (Figure A-0-2C). This effect occurs because the point electrode is much smaller than the size of the cell. As the size of the cell gets larger compared to the size of the electrode, the electrode starts to look like a point source, requiring the contribution of all the multipolar moments for proper modeling[84].

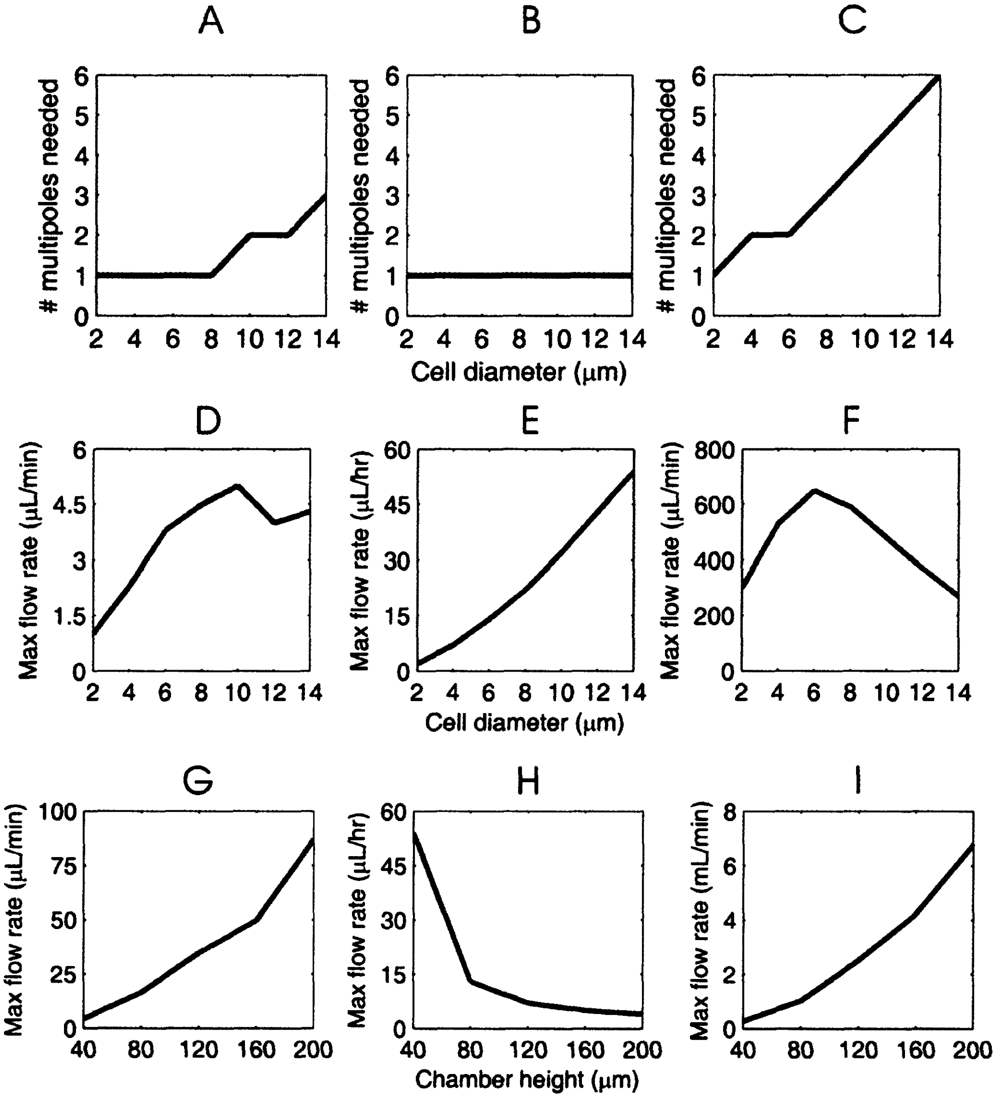

Figure A-0-2: Trapping behavior for the three DEP traps. (*A-C*) DEP multipolar force effects. The number of multipoles needed to bring the maximum flow rate to within 15% of the maximum flow rate when $n=7$, as a function of cell diameter, for the: (*A*) nDEP square trap, (*B*) nDEP octopole, and (*C*) pDEP trap. Note that although we show these plots as continuous functions, only integer numbers of multipoles are possible. (*D-F*) Size-selectivity behavior. The maximum flow rate versus cell diameter, for the: (*D*) nDEP square trap in μL/min, (*E*) nDEP octopole in μL/hr, and (*F*) pDEP trap in μL/min. (*G-I*) Flow chamber height effects. The maximum flow rate versus chamber height, for the: (*G*) nDEP square trap in μL/min, (*H*) nDEP octopole in μL/hr, and (*I*) pDEP trap in mL/min.

Trap Size-Selectivity

To determine how the three traps' operating characteristics changed with cell size, we simulated the maximum flow rate as a function of cell diameter with all other parameters held constant (e.g., voltage, frequency, etc.). For the nDEP square trap, we see that there is size-selectivity such that the maximum flow rate initially increases with cell diameter, approaching a peak maximum flow rate, and then starts to decrease with cell diameter (Figure A-0-2D). Since the dipole contribution of the DEP force increases as R^3, we would expect the maximum flow rate to keep increasing with cell size for a given DEP trap. We already elucidated the reasons for the size-selectivity in Section 2.3.2: Size-Selectivity Behavior. Briefly, this effect results from the complex geometry of the force fields in the *z*-direction. There exists a stability transition line below which the cell experiences a downward force, pushing it into the trap and keeping it stably held. Above the stability transition line, the cell experiences an upward force, pushing it out of the trap. The smaller and larger particles cross this stability transition line into the region of upward force at lower flow rates than the medium-sized particles, producing size-selectivity behavior.

The nDEP octopole trap displays the expected behavior for a DEP trap – the maximum flow rate, and therefore the DEP force, increases with cell size (Figure A-0-2E). The increase scales approximately as R^2. This result is best explained with a scaling analysis, similar to that used by Jones[141]. At the stable point where the cell is trapped, the DEP force and HD drag force from Poiseuille flow must balance, so $F_{drag} = F_{DEP}$. Looking at the relevant components of these forces (Eq. 1-1 and 1-7), we can set up a proportionality for the maximum flow rate, $QR \propto R^3 \nabla E^2$, where Q is the flow rate and ∇E^2 is the gradient of the electric field squared. If we cancel the R term from both sides, we see that $Q \propto R^2 \nabla E^2$. Since ∇E^2 at the cell center does not significantly change with cell size, the maximum flow rate will scale approximately as R^2.

The pDEP trap shows size-selectivity similar to the nDEP square trap (Figure A-0-2F). In this case, the force fields in the *z*-direction do not affect the size-selectivity, since the trap pulls cells to the point electrode with incredibly strong forces (on the order of nanoNewtons). A similar scaling analysis as above helps to explain this size-selectivity. Once again, at equilibrium the DEP force and HD drag force from the shear flow are equal in magnitude. Looking at the relevant components (Eq. 1-1 and 1-6), we set up a proportionality for the maximum flow rate, $QRz \propto R^3 \nabla E^2$, where z is the distance from the particle center to the bottom surface. Since the cell is trapped on the bottom surface at the point electrode, $z = R$, and $QR^2 \propto R^3 \nabla E^2$. If we cancel the R^2 term from both sides, we see that $Q \propto R \nabla E^2$. If we look at the individual contributions from each of these terms as a function of the cell diameter, we see the trivial relation that R increases with cell diameter (Figure A-0-3A). However, ∇E^2 decreases significantly with cell diameter (Figure A-0-3B). This effect occurs because the electric fields decrease quickly as one moves further and further away from the point electrode. Since the larger cells occupy more volume further away from the point electrode, the field gradients at the particle center will be smaller. By multiplying these two contributions together, we are able to reproduce the same size-selectivity shape as seen in Figure A-0-2F (Figure A-0-3C). Thus, the size-selectivity is due to a combination of factors, including the increased DEP force due to the cell size, the decreased DEP force due to the electric field geometry, and the increased drag force due to the cell size (which was hidden in the scaling analysis by the cancellation of the R^2 term).

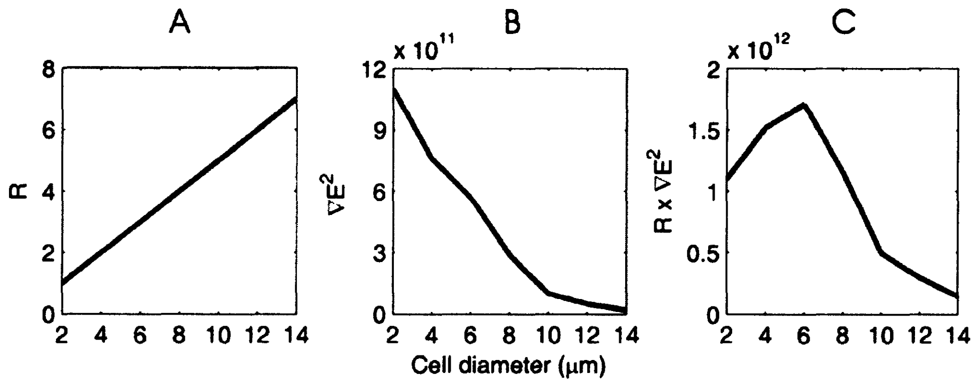

Figure A-0-3: pDEP size-selectivity scaling analysis. (*A*) The cell radius versus cell diameter. (*B*) ∇E^2 at the cell center versus the cell diameter. (*C*) $R \times \nabla E^2$ at the cell center, which is proportional to the flow rate, versus the cell diameter.

Chamber Height Effects

We have seen previously that some traps highly benefit from an increase in flow chamber height, since it allows for an increase in the trap's maximum flow rate[45]. For the three electrode geometries, we simulated the maximum flow rate as a function of the flow chamber height for a 14 μm-diameter cell. For the nDEP square trap, we see that the maximum flow rate increases with chamber height (Figure A-0-2G). This behavior occurs because for any trapped cell, the DEP force and drag force must be equal in magnitude. Since the HD drag force from the shear flow is proportional to Q/h^2 (Eq. 1-6), where h is the flow chamber height, and the DEP force is independent of Q and h, increasing the chamber height will allow an increase in the maximum flow rate. For this trap, the DEP force is independent of h because both electrodes are on the bottom surface, so changing the chamber height does not change the electrode spacing.

For the nDEP octopole trap, we see that the maximum flow rate quickly decreases as the chamber height increases (Figure A-0-2H). This effect occurs because the DEP force is now dependent on h, since the electrodes are on both the top and bottom surfaces. By doubling the chamber height, from 40 to 80 μm, we can see the disappearance of the octopole cage – the stable octopole geometry essentially turns into two separate quadrupole geometries (Figure A-0-4). Quadrupole traps are much weaker due to their lack of stability in the *z*-direction – they levitate the cells away from the traps into higher shear flows and the cell is pushed out of the trap[67]. Above a chamber height of 80 μm, further increases in chamber height do not decrease the maximum flow rate as significantly.

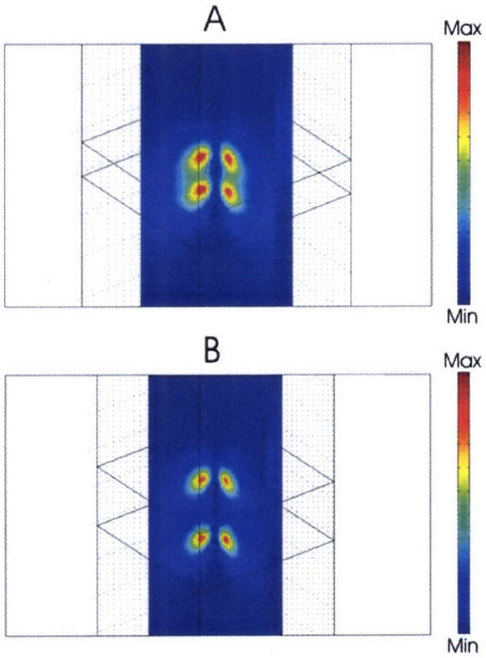

Figure A-0-4: nDEP octopole electric fields. FEMLAB 3-D plot of the electric fields for the (*A*) a 40-μm chamber height and (*B*) an 80-μm chamber height.

For the pDEP trap, we see the maximum flow rate increases with chamber height (Figure A-0-2I). This behavior is unexpected since increasing the chamber height increases the distance between the two electrodes. We would assume that this should decrease the electric field and therefore the DEP force and maximum flow rate as well. To investigate this effect, we solved for the *z*-directed electric field as a function of chamber height, since this quantity should be the most sensitive to chamber height. We found that there is only a slight decrease (~6%) in electric field magnitude over this range of chamber heights. For further validation, we also examined the analytical solution to the cone-plate electrode geometry[142], which is very similar to this points-and-lid geometry. Using the analytical solution to the *z*-directed electric fields, for an electrode separation of 40-200 μm, we also found that the electric field magnitude only decreases slightly (2%) over this range of chamber heights. Therefore, for the pDEP trap, these chamber heights are far enough away that the 3 μm-diameter point electrode operates like a point source. We saw this behavior earlier for the same trap when examining the DEP multipolar force effects. Furthermore, we looked at the *x*-directed DEP force to determine if it was also as insensitive to variations in chamber height. We found that the DEP force only varies by about 5% over this range of chamber heights and therefore is not significantly dependent on h, so an increase in chamber height allows an increase in the maximum flow rate for the same reasons as the nDEP square trap above.

Comparing Various DEP Trap Geometries

In addition to quantitative analyses on a given DEP trap geometry, the modeling software permits comparisons of trapping behavior across multiple trap geometries rather easily. The three traps simulated here are very different in nature: nDEP vs. pDEP, symmetric vs. asymmetric traps, planar vs. 3-D, and small vs. large trap sizes when compared to the size of the cell.

From the three plots in Figure A-0-2D-F, we are able to compare the trap strength of these traps under the same set of experimental conditions. For a 14 μm-diameter cell, the nDEP octopole traps withstand flows of 0.6 μL/min, the nDEP square trap holds against 4.3 μL/min, and the pDEP trap operates up to 270 μL/min. However, this may be an unfair comparison since the nDEP octopole traps cells towards the center of the chamber, where the velocity, and thus the HD drag force is greatest. The difference in maximum linear flow velocities between the nDEP traps is somewhat less, 0.2 mm/s for the nDEP octopole and 0.8 mm/s for the nDEP square trap, while the pDEP trap is still much stronger with a linear velocity of 50.2 mm/s. The high strength of the pDEP trap is due to several factors. First, pDEP traps usually have a greater CM factor, which has a maximum of +1.0, while nDEP traps can only have a maximum magnitude of |-0.5|. If the nDEP traps are in cell-culture media, which is one of the advantages of using nDEP for cell trapping, then the CM factor is only ~-0.2. This gives the pDEP traps a 2-5× stronger advantage, depending on the media conductivity. In addition, pDEP trap geometries generally produce higher electric field gradients in close proximity to the trapped particles. nDEP traps usually position the cell far away from the electrodes at the electric-field minima, where the DEP force is smallest, whereas the pDEP traps hold the cell at the electric-field maxima, where the DEP force is highest. Our nDEP square trap capitalizes on this fact by placing the cell in the electric field minima, yet very close to the electric field maxima, thus creating the first planar nDEP trap that can resist significantly high flow rates.

Furthermore, we can compare the trapping behavior as a function of cell size. If trying to trap a mixed-size population of cells, all three of these examined trap geometries will discriminate in their trapping behavior. The nDEP octopole selects for larger cells, since the maximum flow rate increases with cell diameter. The nDEP square trap and pDEP trap are both size-selective, being optimized to trap cells with certain diameters. However, because the nDEP square trap is much weaker than the pDEP trap, it is only selective over a range of a few μL/min, whereas the pDEP trap is selective over hundreds of μL/min. This size-selectivity behavior, easily tuned by changing the trap dimensions[45], could serve as an advantage if trying to sort cells based on size.

Aside from their trapping behavior, these traps demonstrate other inherent differences, most of which were already described in the Introduction (Section 1.4.1: DEP Trap Requirements). The pDEP trap and the nDEP octopole trap are both 3-D geometries, implemented using electrodes on both the top and bottom surfaces of the flow chamber. Since the pDEP top electrode is a plane, alignment with the bottom point electrode is unnecessary. However, the nDEP octopole requires proper alignment between the top and bottom quadrupoles for effective operation. The pDEP trap also requires the cells to be immersed in an artificially low-conductivity media, which can affect cell physiology, whereas the nDEP traps can be used with normal cell-culture media. Lastly, the nDEP square trap and pDEP trap hold cells near the bottom-surface electrodes, while the nDEP octopole traps cells near the center of the flow chamber. Therefore, the nDEP octopole is advantageous if trying to prevent cells from inadvertently sticking to the bottom substrate, while the nDEP square trap and pDEP trap are more appropriate for cell patterning. However, the nDEP octopole could also potentially trap cells near the bottom substrate by varying the applied voltages.

References

1. Boheler, K. R. et al. Differentiation of pluripotent embryonic stem cells into cardiomyocytes. *Circulation Research* **91**, 189-201 (2002).
2. Nishikawa, S., Hirashima, M., Matsuyoshi, N. & Kodama, H. Progressive lineage analysis by cell sorting and culture identifies FLK1(+)VE-cadherin(+) cells at a diverging point of endothelial and hemopoietic lineages. *Development* **125**, 1747-1757 (1998).
3. Hamazaki, T. et al. Hepatic maturation in differentiating embryonic stem cells in vitro. *Febs Letters* **497**, 15-19 (2001).
4. Lumelsky, N. et al. Differentiation of embryonic stem cells to insulin-secreting structures similar to pancreatic islets. *Science* **292**, 1389-1394 (2001).
5. Fraichard, A. et al. In-Vitro Differentiation of Embryonic Stem-Cells into Glial-Cells and Functional-Neurons. *Journal of Cell Science* **108**, 3181-3188 (1995).
6. Bain, G., Kitchens, D., Yao, M., Huettner, J. E. & Gottlieb, D. I. Embryonic Stem-Cells Express Neuronal Properties in-Vitro. *Developmental Biology* **168**, 342-357 (1995).
7. Thomson, J. A. et al. Embryonic stem cell lines derived from human blastocysts. *Science* **282**, 1145-1147 (1998).
8. Niwa, H., Miyazaki, J. & Smith, A. G. Quantitative expression of Oct-3/4 defines differentiation, dedifferentiation or self-renewal of ES cells. *Nature Genetics* **24**, 372-376 (2000).
9. Chambers, I. et al. Functional expression cloning of Nanog, a pluripotency sustaining factor in embryonic stem cells. *Cell* **113**, 643-655 (2003).
10. Chambers, I. & Smith, A. Self-renewal of teratocarcinoma and embryonic stem cells. *Oncogene* **23**, 7150-7160 (2004).
11. Williams, R. L. et al. Myeloid-Leukemia Inhibitory Factor Maintains the Developmental Potential of Embryonic Stem-Cells. *Nature* **336**, 684-687 (1988).
12. Taga, T. & Kishimoto, T. gp130 and the interleukin-6 family of cytokines. *Annual Review of Immunology* **15**, 797-819 (1997).
13. Matsuda, T. et al. STAT3 activation is sufficient to maintain an undifferentiated state of mouse embryonic stem cells. *Embo Journal* **18**, 4261-4269 (1999).
14. Raz, R., Lee, C. K., Cannizzaro, L. A., D'Eustachio, P. & Levy, D. E. Essential role of STAT3 for embryonic stem cell pluripotency. *Proceedings of the National Academy of Sciences of the United States of America* **96**, 2846-2851 (1999).
15. Viswanathan, S. et al. Supplementation-dependent differences in the rates of embryonic stem cell self-renewal, differentiation, and apoptosis. *Biotechnology and Bioengineering* **84**, 505-517 (2003).
16. Ying, Q. L., Nichols, J., Chambers, I. & Smith, A. BMP induction of Id proteins suppresses differentiation and sustains embryonic stem cell self-renewal in collaboration with STAT3. *Cell* **115**, 281-292 (2003).
17. Sato, N., Meijer, L., Skaltsounis, L., Greengard, P. & Brivanlou, A. H. Maintenance of pluripotency in human and mouse embryonic stem cells through activation of Wnt signaling by a pharmacological GSK-3-specific inhibitor. *Nature Medicine* **10**, 55-63 (2004).

18. Gratsch, T. E. & O'Shea, K. S. Noggin and chordin have distinct activities in promoting lineage commitment of mouse embryonic stem (ES) cells. *Developmental Biology* **245**, 83-94 (2002).
19. Zandstra, P. W., Le, H. V., Daley, G. Q., Griffith, L. G. & Lauffenburger, D. A. Leukemia inhibitory factor (LIF) concentration modulates embryonic stem cell self-renewal and differentiation independently of proliferation. *Biotechnology and Bioengineering* **69**, 607-617 (2000).
20. Tsai, R. Y. L. & McKay, R. D. G. Cell contact regulates fate choice by cortical stem cells. *Journal of Neuroscience* **20**, 3725-3735 (2000).
21. Javazon, E. H., Colter, D. C., Schwarz, E. J. & Prockop, D. J. Rat marrow stromal cells are more sensitive to plating density and expand more rapidly from single-cell-derived colonies than human marrow stromal cells. *Stem Cells* **19**, 219-225 (2001).
22. Purpura, K. A., Aubin, J. E. & Zandstra, P. W. Sustained in vitro expansion of bone progenitors is cell density dependent. *Stem Cells* **22**, 39-50 (2003).
23. Dani, C. et al. Paracrine induction of stem cell renewal by LIF-deficient cells: A new ES cell regulatory pathway. *Developmental Biology* **203**, 149-162 (1998).
24. Rathjen, P. D. et al. Developmentally Programmed Induction of Differentiation Inhibiting Activity and the Control of Stem-Cell Populations. *Genes & Development* **4**, 2308-2318 (1990).
25. Schratt, G. et al. Serum response factor is required for immediate-early gene activation yet is dispensable for proliferation of embryonic stem cells. *Molecular and Cellular Biology* **21**, 2933-2943 (2001).
26. Berrill, A. et al. Assessment of stem cell markers during long-term culture of mouse embryonic stem cells. *Cytotechnology* **44**, 77-91 (2004).
27. Hamazaki, T., Oka, M., Yamanaka, S. & Terada, N. Aggregation of embryonic stem cells induces Nanog repression and primitive endoderm differentiation. *Journal of Cell Science* **117**, 5681-5686 (2004).
28. Bhatia, S. N., Balis, U. J., Yarmush, M. L. & Toner, M. Microfabrication of hepatocyte/fibroblast co-cultures: Role of homotypic cell interactions. *Biotechnology Progress* **14**, 378-387 (1998).
29. Chen, C. S., Mrksich, M., Huang, S., Whitesides, G. M. & Ingber, D. E. Geometric control of cell life and death. *Science* **276**, 1425-1428 (1997).
30. Folch, A. & Toner, M. Cellular micropatterns on biocompatible materials. *Biotechnology Progress* **14**, 388-392 (1998).
31. Tan, W. & Desai, T. A. Microfluidic patterning of cells in extracellular matrix biopolymers: Effects of channel size, cell type, and matrix composition on pattern integrity. *Tissue Engineering* **9**, 255-267 (2003).
32. Tempelman, L. A., King, K. D., Anderson, G. P. & Ligler, F. S. Quantitating staphylococcal enterotoxin B in diverse media using a portable fiber-optic biosensor. *Analytical Biochemistry* **233**, 50-57 (1996).
33. Paddle, B. M. Biosensors for chemical and biological agents of defence interest. *Biosensors & Bioelectronics* **11**, 1079-1113 (1996).
34. Pancrazio, J. J., Whelan, J. P., Borkholder, D. A., Ma, W. & Stenger, D. A. Development and application of cell-based biosensors. *Annals of Biomedical Engineering* **27**, 697-711 (1999).

35. Ostuni, E., Kane, R., Chen, C. S., Ingber, D. E. & Whitesides, G. M. Patterning mammalian cells using elastomeric membranes. *Langmuir* **16**, 7811-7819 (2000).
36. Folch, A., Jo, B.-H., Hurtado, O., Beebe, D. J. & Tonor, M. Microfabricated elastomeric stencils for micropatterning cell cultures. *J Biomed Mater Res* **52**, 346-353 (2000).
37. Revzin, A., Tompkins, R. G. & Toner, M. Surface engineering with poly(ethylene glycol) photolithography to create high-density cell arrays on glass. *Langmuir* **19**, 9855-9862 (2003).
38. Rettig, J. R. & Folch, A. Large-scale single-cell trapping and imaging using microwell arrays. *Analytical Chemistry* **77**, 5628-5634 (2005).
39. Singhvi, R. et al. Engineering Cell-Shape and Function. *Science* **264**, 696-698 (1994).
40. Jiang, X. Y., Ferrigno, R., Mrksich, M. & Whitesides, G. M. Electrochemical desorption of self-assembled monolayers noninvasively releases patterned cells from geometrical confinements. *Journal of the American Chemical Society* **125**, 2366-2367 (2003).
41. Lahann, J. et al. A reversibly switching surface. *Science* **299**, 371-374 (2003).
42. Ozkan, M. et al. Electro-optical platform for the manipulation of live cells. *Langmuir* **19**, 1532-1538 (2003).
43. Birkbeck, A. L. et al. VCSEL Arrays as micromanipulators in chip-based biosystems. *Biomedical Microdevices* **5**, 47-54 (2003).
44. Dufresne, E. R. & Grier, D. G. Optical tweezer arrays and optical substrates created with diffractive optics. *Review of Scientific Instruments* **69**, 1974-1977 (1998).
45. Rosenthal, A. & Voldman, J. Dielectrophoretic traps for single-particle patterning. *Biophysical Journal* **88**, 2193-2205 (2005).
46. Albrecht, D. R., Underhill, G. H., Wassermann, T. B., Sah, R. L. & Bhatia, S. N. Probing the role of multicellular organization in three-dimensional microenvironments. *Nature Methods* **3**, 369-375 (2006).
47. Pohl, H. A. *Dielectrophoresis* (Cambridge University Press, 1978).
48. Li, H. B., Zheng, Y. N., Akin, D. & Bashir, R. Characterization and modeling of a microfluidic dielectrophoresis filter for biological species. *Journal of Microelectromechanical Systems* **14**, 103-112 (2005).
49. Green, N. G. & Morgan, H. Dielectrophoretic separation of nano-particles. *Journal of Physics D-Applied Physics* **30**, L41-L44 (1997).
50. Fuhr, G., Glasser, H., Muller, T. & Schnelle, T. Cell Manipulation and Cultivation under Ac Electric-Field Influence in Highly Conductive Culture Media. *Biochimica Et Biophysica Acta-General Subjects* **1201**, 353-360 (1994).
51. Wang, X. B., Huang, Y., Burt, J. P. H., Markx, G. H. & Pethig, R. Selective Dielectrophoretic Confinement of Bioparticles in Potential-Energy Wells. *Journal of Physics D-Applied Physics* **26**, 1278-1285 (1993).
52. Albrecht, D. R., Tsang, V. L., Sah, R. L. & Bhatia, S. N. Photo- and electropatterning of hydrogel-encapsulated living cell arrays. *Lab on a Chip* **5**, 111-118 (2005).
53. Morgan, H., Hughes, M. P. & Green, N. G. Separation of submicron bioparticles by dielectrophoresis. *Biophysical Journal* **77**, 516-525 (1999).

54. Green, N. G., Morgan, H. & Milner, J. J. Manipulation and trapping of sub-micron bioparticles using dielectrophoresis. *Journal of Biochemical and Biophysical Methods* **35**, 89-102 (1997).
55. Lapizco-Encinas, B. H., Simmons, B. A., Cummings, E. B. & Fintschenko, Y. Insulator-based dielectrophoresis for the selective concentration and separation of live bacteria in water. *Electrophoresis* **25**, 1695-1704 (2004).
56. Suehiro, J., Hamada, R., Noutomi, D., Shutou, M. & Hara, M. Selective detection of viable bacteria using dielectrophoretic impedance measurement method. *Journal of Electrostatics* **57**, 157-168 (2003).
57. Gray, D. S., Tan, J. L., Voldman, J. & Chen, C. S. Dielectrophoretic registration of living cells to a microelectrode array. *Biosensors & Bioelectronics* **19**, 771-780 (2004).
58. Prasad, S. et al. Separation of individual neurons using dielectrophoretic alternative current fields. *Journal of Neuroscience Methods* **135**, 79-88 (2004).
59. Schnelle, T., Hagedorn, R., Fuhr, G., Fiedler, S. & Muller, T. 3-Dimensional Electric-Field Traps for Manipulation of Cells - Calculation and Experimental-Verification. *Biochimica Et Biophysica Acta* **1157**, 127-140 (1993).
60. Manaresi, N. et al. A CMOS chip for individual cell manipulation and detection. *Ieee Journal of Solid-State Circuits* **38**, 2297-2305 (2003).
61. Voldman, J., Toner, M., Gray, M. L. & Schmidt, M. A. Design and analysis of extruded quadrupolar dielectrophoretic traps. *Journal of Electrostatics* **57**, 69-90 (2003).
62. Frenea, M., Faure, S. P., Le Pioufle, B., Coquet, P. & Fujita, H. Positioning living cells on a high-density electrode array by negative dielectrophoresis. *Materials Science & Engineering C-Biomimetic and Supramolecular Systems* **23**, 597-603 (2003).
63. Heida, T., Rutten, W. L. C. & Marani, E. Dielectrophoretic trapping of dissociated fetal cortical rat neurons. *Ieee Transactions on Biomedical Engineering* **48**, 921-930 (2001).
64. Matsue, T., Matsumoto, N. & Uchida, I. Rapid micropatterning of living cells by repulsive dielectrophoretic force. *Electrochimica Acta* **42**, 3251-3256 (1997).
65. Wang, X. B., Huang, Y., Gascoyne, P. R. C. & Becker, F. F. Dielectrophoretic manipulation of particles. *Ieee Transactions on Industry Applications* **33**, 660-669 (1997).
66. Fuhr, G. et al. Levitation, Holding, and Rotation of Cells within Traps Made by High-Frequency Fields. *Biochimica Et Biophysica Acta* **1108**, 215-223 (1992).
67. Voldman, J., Braff, R. A., Toner, M., Gray, M. L. & Schmidt, M. A. Holding forces of single-particle dielectrophoretic traps. *Biophysical Journal* **80**, 531-541 (2001).
68. Schnelle, T., Muller, T. & Fuhr, G. Trapping in AC octode field cages. *Journal of Electrostatics* **50**, 17-29 (2000).
69. Hartley, L. F., Kaler, K. & Paul, R. Quadrupole levitation of microscopic dielectric particles. *Journal of Electrostatics* **46**, 233-246 (1999).
70. Markx, G. H., Pethig, R. & Rousselet, J. The dielectrophoretic levitation of latex beads, with reference to field-flow fractionation. *Journal of Physics D-Applied Physics* **30**, 2470-2477 (1997).

71. Watarai, H., Sakamoto, T. & Tsukahara, S. In situ measurement of dielectrophoretic mobility of single polystyrene microparticles. *Langmuir* **13**, 2417-2420 (1997).
72. Muller, T. et al. A 3-D microelectrode system for handling and caging single cells and particles. *Biosensors & Bioelectronics* **14**, 247-256 (1999).
73. Schnelle, T., Muller, T., Gradl, G., Shirley, S. G. & Fuhr, G. Paired microelectrode system: dielectrophoretic particle sorting and force calibration. *Journal of Electrostatics* **47**, 121-132 (1999).
74. Hughes, M. P. & Morgan, H. Measurement of bacterial flagellar thrust by negative dielectrophoresis. *Biotechnology Progress* **15**, 245-249 (1999).
75. Voldman, J. in *Electrical Engineering and Computer Science* 152 (Massachusetts Institute of Technology, Cambridge, 2001).
76. Voldman, J., Gray, M. L., Toner, M. & Schmidt, M. A. A microfabrication-based dynamic array cytometer. *Analytical Chemistry* **74**, 3984-3990 (2002).
77. Leighton, D. & Acrivos, A. The lift on a small sphere touching a plane in the presence of a simple shear flow. *Journal of Applied Mathematics and Physics* **36**, 174-178 (1985).
78. Cherukat, P. & McLaughlin, J. B. The Inertial Lift on a Rigid Sphere in a Linear Shear-Flow Field near a Flat Wall. *Journal of Fluid Mechanics* **263**, 1-18 (1994).
79. Rosenthal, A., Taff, B. M. & Voldman, J. Quantitative modeling of dielectrophoretic traps. *Lab on a Chip* **6**, 508-515 (2006).
80. Washizu, M., Jones, T. B. & Kaler, K. Higher-Order Dielectrophoretic Effects - Levitation at a Field Null. *Biochimica Et Biophysica Acta* **1158**, 40-46 (1993).
81. Jones, T. B. & Washizu, M. Multipolar dielectrophoretic and electrorotation theory. *Journal of Electrostatics* **37**, 121-134 (1996).
82. Washizu, M. & Jones, T. B. Multipolar Dielectrophoretic Force Calculation. *Journal of Electrostatics* **33**, 187-198 (1994).
83. Washizu, M. & Jones, T. B. Generalized multipolar dielectrophoretic force and electrorotational torque calculation. *Journal of Electrostatics* **38**, 199-211 (1996).
84. Jones, T. B. *Electromechanics of Particles* (Cambridge University Press, 1995).
85. Goldman, A., Cox, R. & Brenner, H. Slow viscous motion of a sphere parallel to a plane wall - II Couette flow. *Chemical Engineering Science* **22**, 653-660 (1967).
86. Deen, W. M. *Analysis of Transport Phenomena* (Oxford University Press, New York, 1998).
87. Ganatos, P., Pfeffer, R. & Weinbaum, S. A Strong Interaction Theory for the Creeping Motion of a Sphere between Plane Parallel Boundaries .2. Parallel Motion. *Journal of Fluid Mechanics* **99**, 755-783 (1980).
88. Yamamura, S. et al. Single-cell microarray for analyzing cellular response. *Analytical Chemistry* **77**, 8050-8056 (2005).
89. Khademhosseini, A. et al. Molded polyethylene glycol microstructures for capturing cells within microfluidic channels. *Lab on a Chip* **4**, 425-430 (2004).
90. Ostuni, E., Chen, C. S., Ingber, D. E. & Whitesides, G. M. Selective deposition of proteins and cells in arrays of microwells. *Langmuir* **17**, 2828-2834 (2001).
91. Love, J. C., Ronan, J. L., Grotenbreg, G. M., van der Veen, A. G. & Ploegh, H. L. A microengraving method for rapid selection of single cells producing antigen-specific antibodies. *Nature Biotechnology* **24**, 703-707 (2006).

92. Jo, B. H., Van Lerberghe, L. M., Motsegood, K. M. & Beebe, D. J. Three-dimensional micro-channel fabrication in polydimethylsiloxane (PDMS) elastomer. *Journal of Microelectromechanical Systems* **9**, 76-81 (2000).
93. Fiedler, S., Shirley, S. G., Schnelle, T. & Fuhr, G. Dielectrophoretic sorting of particles and cells in a microsystem. *Analytical Chemistry* **70**, 1909-1915 (1998).
94. Medoro, G. et al. A lab-on-a-chip for cell detection and manipulation. *Ieee Sensors Journal* **3**, 317-325 (2003).
95. Ramos, A., Morgan, H., Green, N. G. & Castellanos, A. Ac electrokinetics: a review of forces in microelectrode structures. *Journal of Physics D-Applied Physics* **31**, 2338-2353 (1998).
96. Archer, S., Li, T. T., Evans, A. T., Britland, S. T. & Morgan, H. Cell reactions to dielectrophoretic manipulation. *Biochemical and Biophysical Research Communications* **257**, 687-698 (1999).
97. Glasser, H. & Fuhr, G. Cultivation of cells under strong ac-electric field - differentiation between heating and trans-membrane potential effects. *Bioelectrochemistry and Bioenergetics* **47**, 301-310 (1998).
98. Foster, K. R. & Schwan, H. P. Dielectric-Properties of Tissues and Biological-Materials - a Critical-Review. *Critical Reviews in Biomedical Engineering* **17**, 25-104 (1989).
99. Huang, Y., Wang, X. B., Becker, F. F. & Gascoyne, P. R. C. Introducing dielectrophoresis as a new force field for field-flow fractionation. *Biophysical Journal* **73**, 1118-1129 (1997).
100. Zhang, J., Davidson, R. M., Wei, M. D. & Loew, L. M. Membrane electric properties by combined patch clamp and fluorescence ratio imaging in single neurons. *Biophysical Journal* **74**, 48-53 (1998).
101. Antic, S. & Zecevic, D. Optical Signals from Neurons with Internally Applied Voltage-Sensitive Dyes. *Journal of Neuroscience* **15**, 1392-1405 (1995).
102. Frey, W. et al. Plasma membrane voltage changes during nanosecond pulsed electric field exposure. *Biophysical Journal* **90**, 3608-3615 (2006).
103. Wu, J. Y. et al. Voltage-sensitive dyes for monitoring multineuronal activity in the intact central nervous system. *Histochemical Journal* **30**, 169-187 (1998).
104. Xu, C. & Loew, L. M. The effect of asymmetric surface potentials on the intramembrane electric field measured with voltage-sensitive dyes. *Biophysical Journal* **84**, 2768-2780 (2003).
105. Zohar, O. et al. Thermal imaging of receptor-activated heat production in single cells. *Biophysical Journal* **74**, 82-89 (1998).
106. Heida, T., Wagenaar, J. B. M., Rutten, W. L. C. & Marani, E. Investigating membrane breakdown of neuronal cells exposed to nonuniform electric fields by finite-element modeling and experiments. *Ieee Transactions on Biomedical Engineering* **49**, 1195-1203 (2002).
107. Muller, T. et al. The potential of dielectrophoresis for single-cell experiments. *Ieee Engineering in Medicine and Biology Magazine* **22**, 51-61 (2003).
108. Weaver, J. C., Vaughan, T. E. & Martin, G. T. Biological effects due to weak electric and magnetic fields: The temperature variation threshold. *Biophysical Journal* **76**, 3026-3030 (1999).

109. Anderson, D. G., Levenberg, S. & Langer, R. Nanoliter-scale synthesis of arrayed biomaterials and application to human embryonic stem cells. *Nature Biotechnology* **22**, 863-866 (2004).
110. Jiang, X., Bruzewicz, D. A., Wong, A. P., Piel, M. & Whitesides, G. M. Directing cell migration with asymmetric micropatterns. *PNAS* **102**, 975-978 (2005).
111. Richards, M., Fong, C. Y., Chan, W. K., Wong, P. C. & Bongso, A. Human feeders support prolonged undifferentiated growth of human inner cell masses and embryonic stem cells. *Nature Biotechnology* **20**, 933-936 (2002).
112. Kawasaki, H. et al. Induction of midbrain dopaminergic neurons from ES cells by stromal cell-derived inducing activity. *Neuron* **28**, 31-40 (2000).
113. Bhatia, S. N., Yarmush, M. L. & Toner, M. Controlling cell interactions by micropatterning in co-cultures: Hepatocytes and 3T3 fibroblasts. *Journal of Biomedical Materials Research* **34**, 189-199 (1997).
114. Nagano, K. et al. Large-scale identification of proteins expressed in mouse embryonic stem cells. *Proteomics* **5**, 1346-1361 (2005).
115. Batsilas, L., Berezhkovskii, A. M. & Shvartsman, S. Y. Stochastic model of autocrine and paracrine signals in cell culture assays. *Biophysical Journal* **85**, 3659-3665 (2003).
116. Hilton, D. J. & Nicola, N. A. Kinetic Analyses of the Binding of Leukemia Inhibitory Factor to Receptors on Cells and Membranes and in Detergent Solution. *Journal of Biological Chemistry* **267**, 10238-10247 (1992).
117. Viswanathan, S., Benatar, T., Rose-John, S., Lauffenburger, D. A. & Zandstra, P. W. Ligand/receptor signaling threshold (LIST) model accounts for gp130-mediated embryonic stem cell self-renewal responses to LIF and HIL-6. *Stem Cells* **20**, 119-138 (2002).
118. Berezhkovskii, A. M., Batsilas, L. & Slvartsman, S. Y. Ligand trapping in epithelial layers and cell cultures. *Biophysical Chemistry* **107**, 221-227 (2004).
119. Levitan, I., Helmke, B. P. & Davies, P. F. A chamber to permit invasive manipulation of adherent cells in laminar flow with minimal disturbance of the flow field. *Annals of Biomedical Engineering* **28**, 1184-1193 (2000).
120. Rathjen, P. D., Toth, S., Willis, A., Heath, J. K. & Smith, A. G. Differentiation Inhibiting Activity Is Produced in Matrix-Associated and Diffusible Forms That Are Generated by Alternate Promoter Usage. *Cell* **62**, 1105-1114 (1990).
121. Randall, G. C. & Doyle, P. S. Permeation-driven flow in poly(dimethylsiloxane) microfluidic devices. *Proceedings of the National Academy of Sciences of the United States of America* **102**, 10813-10818 (2005).
122. Fok, E. Y. L. & Zandstra, P. W. Shear-controlled single-step mouse embryonic stem cell expansion and embryoid body-based differentiation. *Stem Cells* **23**, 1333-1342 (2005).
123. Yamanaka, Y., Ralston, A., Stephenson, R. O. & Rossant, J. Cell and molecular regulation of the mouse blastocyst. *Developmental Dynamics* **235**, 2301-2314 (2006).
124. Johnson, M. H. & Ziomek, C. A. Induction of Polarity in Mouse 8-Cell Blastomeres - Specificity, Geometry, and Stability. *Journal of Cell Biology* **91**, 303-308 (1981).

125. Ziomek, C. A. & Johnson, M. H. Cell-Surface Interaction Induces Polarization of Mouse 8-Cell Blastomeres at Compaction. *Cell* **21**, 935-942 (1980).
126. Friedlander, R. M. Mechanisms of disease: Apoptosis and caspases in neurodegenerative diseases. *New England Journal of Medicine* **348**, 1365-1375 (2003).
127. Dang, S. M., Kyba, M., Perlingeiro, R., Daley, G. Q. & Zandstra, P. W. Efficiency of embryoid body formation and hematopoietic development from embryonic stem cells in different culture systems. *Biotechnology and Bioengineering* **78**, 442-453 (2002).
128. Dang, S. M., Gerecht-Nir, S., Chen, J., Itskovitz-Eldor, J. & Zandstra, P. W. Controlled, scalable embryonic stem cell differentiation culture. *Stem Cells* **22**, 275-282 (2004).
129. Chappuis-Flament, S., Wong, E., Hicks, L. D., Kay, C. M. & Gumbiner, B. M. Multiple cadherin extracellular repeats mediate homophilic binding and adhesion. *Journal of Cell Biology* **154**, 231-243 (2001).
130. Hogan, C. et al. Rap1 regulates the formation of E-cadherin-based cell-cell contacts. *Molecular and Cellular Biology* **24**, 6690-6700 (2004).
131. Hao, J., Li, T. G., Qi, X. X., Zhao, D. F. & Zhao, G. Q. WNT/beta-catenin pathway up-regulates Stat3 and converges on LIF to prevent differentiation of mouse embryonic stem cells. *Developmental Biology* **290**, 81-91 (2006).
132. Hoeflich, K. P. & Ikura, M. Radixin: cytoskeletal adopter and signaling protein. *International Journal of Biochemistry & Cell Biology* **36**, 2131-2136 (2004).
133. Balda, M. S., Garrett, M. D. & Matter, K. The ZO-1-associated Y-box factor ZONAB regulates epithelial cell proliferation and cell density. *Journal of Cell Biology* **160**, 423-432 (2003).
134. Schneeberger, E. E. & Lynch, R. D. The tight junction: a multifunctional complex. *American Journal of Physiology-Cell Physiology* **286**, C1213-C1228 (2004).
135. Giancotti, F. G. & Ruoslahti, E. Transduction - Integrin signaling. *Science* **285**, 1028-1032 (1999).
136. Czyz, J. & Wobus, A. M. Embryonic stem cell differentiation: The role of extracellular factors. *Differentiation* **68**, 167-174 (2001).
137. Boiani, M. & Scholer, H. R. Regulatory networks in embryo-derived pluripotent stem cells. *Nature Reviews Molecular Cell Biology* **6**, 872-884 (2005).
138. Nelson, C. M. & Chen, C. S. Cell-cell signaling by direct contact increases cell proliferation via a PI3K-dependent signal. *Febs Letters* **514**, 238-242 (2002).
139. Thompson, M. T., Berg, M. C., Tobias, I. S., Rubner, M. F. & Van Vliet, K. J. Tuning compliance of nanoscale polyelectrolyte multilayers to modulate cell adhesion. *Biomaterials* **26**, 6836-6845 (2005).
140. Suemori, H. et al. Efficient establishment of human embryonic stem cell lines and long-term maintenance with stable karyotype by enzymatic bulk passage. *Biochemical and Biophysical Research Communications* **345**, 926-932 (2006).
141. Jones, T. B. Influence of scale on electrostatic forces and torques in AC particulate electrokinetics. *IEE Proceedings Nanobiotechnology* **150**, 39-46 (2003).

142. Jones, T. B. & Kraybill, J. P. Active Feedback-Controlled Dielectrophoretic Levitation. *Journal of Applied Physics* **60**, 1247-1252 (1986).